Doctoral thesis

Search for scalar top-quark pair-production of compressed SUSY scenarios in the final state involving one lepton, jets, and missing transverse energy in pp collisions at $\sqrt{s} = 13$ TeV with the ATLAS detector

ATLAS 検出器を用いた重心系エネルギー 13 TeV の陽子陽子衝突における 1 レプトン、複数ジェット、及び消失横エネルギーを終状態に持つ縮退した超対称性シナリオのスカラートップクォーク対生成の探索

KOUTA ONOGI

High Energy Physics Laboratory
Department of Physics, Nagoya University

February 2018

Abstract

In 2012, the Higgs boson was discovered by the Large Hadron Collider (LHC) experiment at CERN. However, to derive the observed Higgs mass (125 GeV) in the Standard Model (SM), fine tuning between the bare Higgs mass and the radiative correction required. The SM has another problem, which is the absence of the particles constituting the dark matter (DM) indicated by the cosmological observation. One of the candidates of the theory which can solve these problems is the Supersymmetry (SUSY). If the scalar top quark (stop, $\tilde{t}$), which is the superpartner of the SM top quark, exists and has the mass below 1 TeV, the level of fine tuning can be significantly reduced because the radiative correction of the top quark loop can be canceled by the radiative correction of the stop loop. In addition, the neutralino ($\tilde{\chi}_1^0$), which is the neutral lightest supersymmetric particle (LSP) can become a candidate of the DM.

The LHC experiment searched for the stop pair production in a $pp \to \tilde{t}_1\tilde{t}_1 \to t\tilde{\chi}_1^0 t\tilde{\chi}_1^0$ process and set a 1 TeV mass limit by exploiting the highest center-of-mass energy of the pp collisions. Unfortunately, the evidence of the stop pair production was not obtained. The direct searches for the stop pair production in the phase space challenging for the experiments is of interest. An example is the phase space, where two or three of stop, chargino, and neutralino have similar masses.

Here a search is presented for the stop pair production in a $pp \to \tilde{t}_1\tilde{t}_1 \to b\tilde{\chi}_1^\pm b\tilde{\chi}_1^\pm \to bW^\pm\tilde{\chi}_1^0 bW^\pm\tilde{\chi}_1^0$ process with the 36.1 fb^{-1} data of $\sqrt{s} = 13$ TeV pp collisions obtained by the LHC-ATLAS experiment from 2015 to the end of 2016. The search focuses on two theoretical scenarios, which have the compressed mass spectrum between the SUSY particles (sparticles) and can be searched by the final state involving one lepton, jets, and missing transverse energy ($E_{\mathrm{T}}^{\mathrm{miss}}$): I. the higgsino LSP scenario with small mass difference between the chargino ($\tilde{\chi}_1^\pm$) and the neutralino and II. the bino LSP scenario with small mass difference between the stop and the chargino. In case of the higgsino LSP scenario, the signal region (SR), which has a high $E_{\mathrm{T}}^{\mathrm{miss}}$ and an initial state radiation with a high momentum, was set and optimized. The dominant backgrounds ($t\bar{t}$ and W + jets) remaining after the signal event selection were estimated by using a semi-data driven method called the control region (CR) techniques to reduce the systematic uncertainties. The QCD/multi-jets background including a fake leptons was estimated to be negligible. No significant excess above SM expectation was observed in the SR. This result was reinterpreted to determinate the exclusion limit. The higgsino LSP scenario was excluded the stop mass up to 415 GeV. In case of the bino LSP scenario, the SR is introduced with rejecting jets tagged as originating from bottom quarks. The dominant background (W + jets) was estimated by using the CR techniques. No significant excess above the SM expectation was observed in the SR. The bino LSP scenario was excluded in a part of the phase space with the stop mass up to 850 GeV.

The coverage in the phase space has been significantly extended by setting and optimizing the individual SRs dedicated for the two scenarios and by precisely estimating the background. I contributed to the strongly constrain for SUSY, in particular the stop pair production, by searching these scenario having the compressed mass difference between sparticles.

Contents

Chapter 1

Introduction

The ultimate goal of the particle physics is the fundamental understanding of the particles and the interaction. The theory of the particles and the interactions evolved with the validation by the experiment. In 2012, the Higgs boson, which is an essential particle of Standard Model (SM), was discovered by the A Toroidal LHC ApparatuS (ATLAS) and Compact Muon Solenoid (CMS) experiments at the Large Hadron Collider (LHC). The Higgs boson plays an impotant role in the understanding of the "*origin of mass*" of the particles. On the other hand, there are problems which can not be explained by the SM:

- In the SM, fine tuning is required between the bare Higgs boson mass and the radiative correction arising from the one-loop contribution of the top quark,
- Existence of dark matter (DM) is indicated by the cosmological observations, but there are no particle candidates in the SM.

These problems require the extensions of the SM. One of the candidates of extended models which can solve these problems is the model with Supersymmetry (SUSY). SUSY is containing the symmetry between the boson and the fermion. The Minimal Supersymmetric SM (MSSM) is a minimal extension of the SM. MSSM includes a partner (superpartner) for each SM particle. The scalar top quark (stop) $\tilde{t}_1$, which is the superpartner of the SM top quark, contributes to the cancellation of the radiative correction of the Higgs boson mass, and the level of fine tuning can be significantly reduced. In addition, the neutralino $\tilde{\chi}_1^0$, which is the Lightest Supersymmetric Particle (LSP) and is stable under the R-parity conservation, possibly constitutes the DM.

Physicists have been searching for signs of SUSY with several experiments. In the searches for stop-pair production with the decay channel $\tilde{t}_1\tilde{t}_1 \to t\tilde{\chi}_1^0 t\tilde{\chi}_1^0$ at the ATLAS and CMS experiments, no evidence of excess over the SM was found. A mass region of the stop up to 1 TeV was excluded.

This thesis presents the search for the stop-pair production with the decay chain $\tilde{t}_1 \to b\tilde{\chi}_1^\pm \to bW\tilde{\chi}_1^0$, where $\tilde{\chi}_1^\pm$ indicates a chargino, based on 36.1 fb^{-1} data of $\sqrt{s} = 13$ TeV proton-proton (pp) collisions taken by the ATLAS detector. This decay chain makes it possible to search for signs of SUSY in an experimentally challenging phase space, where two or three of $\tilde{t}_1$, $\tilde{\chi}_1^\pm$, and $\tilde{\chi}_1^0$ have similar masses. The analysis focuses on the following two scenarios, which can be probed by the final states containing one lepton, jets and large missing transverse energy ($E_{\mathrm{T}}^{\mathrm{miss}}$):

- a higgsino LSP scenario, which reduces the level of fine tuning of the Higgs boson mass,
- a bino LSP scenario, where the bino is a candidate of the DM.

To search for the stop in these scenarios with maximum possible sensitivity, an analysis method dedicated for each scenario has been developed. In addition, backgrounds are precisely estimated by the Monte Carlo (MC) simulations and semi-data driven method for the reduction of systematic uncertainty.

The structure of the thesis is as follows. In Chapter 2, problems of the SM and theoretical motivation of SUSY are reviewed, and target scenarios of this analysis are described. In Chapter 3, an overview of LHC and the ATLAS detector is shown. In Chapter 4, the phenomenology of the pp collisions and the MC simulations are introduced. In Chapter 5, the object reconstructions and definitions are provided. In Chapter 6 and 7, the analysis method and the result of the search for the higgsino LSP scenario and the bino LSP scenario, respectively, are given. In Chapter 8, the constraints on SUSY parameters are compared with other analyses. In Chapter 9, a conclusion of this thesis is described.

Chapter 2

Theoretical Motivations and SUSY Target Scenarios

2.1 Standard Model of Particle Physics

The SM (Figure 2.1) [1] proposed in the 1970s described phenomena of fundamental particles and their interactions. The most important principles in the SM are symmetries and the Spontaneous Symmetry Breaking (SSB). The six quarks and six leptons, which compose matters, are characterized by the chiral symmetry, and its symmetry breaking. The four gauge bosons (gluon, photon, W boson, Z boson), which intermediate the forces (strong, weak, electromagnetic), are characterized by the gauge symmetry. The scalar Higgs boson, which give a mass to the particle, is introduced by the SSB in the Higgs mechanism. Their existence have been confirmed by a variety of experiments.

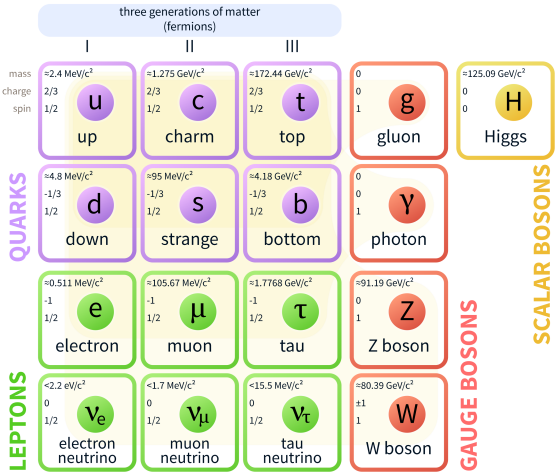

Figure 2.1: The illustration of the Standard Model particles [2]. There are three generation of matter particles, four gauge bosons of force-carrier particles, and the scalar Higgs boson that generate the elementary-particle masses.

2.1.1 Problems of the SM

The SM explains various experimental results. However, there are problems which can not be explained by the SM. Two main problems are discussed in this section.

Fine Tuning Problem

Observable physical quantities, e.g, mass ($m_{\text{obs.}}$), are finite quantities defined by the renormalization for the perturbative expansion. The observed mass is defined as

$$m^2_{\text{obs.}} = m^2_{\text{bare}} + \Delta m^2, \tag{2.1}$$

where m_{bare} is the bare mass and Δm is the radiative correction. Since the bare masses of fermions and gauge bosons are assumed to be zero for the high energy scale, even if a cut-off parameter (Λ_{UV}) is to be the Plank scale ($M_{\text{P}} \equiv \sqrt{\hbar c/G} \sim 10^{19}$ GeV)[1], the radiative corrections to the masses of fermions and the gauge bosons are suppressed until around order of $\log(\Lambda_{\text{UV}})$. In case of a scalar particle, the mass term is accepted by a symmetry. The radiative correction of the Higgs boson mass is affected by the Λ_{UV} times a coupling constant (λ_t) corresponding to a mass of fermions or gauge bosons. The dominant contribution to the radiative correction of the Higgs boson mass is the top quark which is the heaviest particle of the SM, and is written as

$$\Delta m^2_{\text{h}} = -|\lambda_t|^2 \Lambda^2_{\text{UV}} + O(\log(\Lambda_{\text{UV}})). \tag{2.2}$$

Here, λ_t is the coupling constant corresponding to the top quark. Figure 2.2 shows the Feynman diagram for one-loop contribution of the top quark to the Higgs boson mass. To generate the observed Higgs boson mass

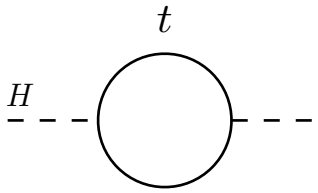

Figure 2.2: Feynman diagram of one-loop contribution to the Higgs boson mass squared m_h^2 from the top quark.

of 125 GeV, the bare mass squared of the Higgs boson should be order of 10^{38} and the fine tuning between the bare mass and the radiative correction is need at a level of $O(10^{-34})$ [3–7].

Absence of the Particles Constituting the Dark Matter

The existence of DM is indicated by various astronomical and cosmological measurements. The DM is predicted to be stable, natural, and colorless. This particle of the SM can not constitute the DM. Therefore, existence of the new physics beyond the SM is expected [8, 9].

Cosmic microwave background (CMB) [9] is radiation coming from the early universe. As the universe expands, the primordial plasma, which is composed of hydrogen and helium, cooled and converted into gas. CMB were radiated from this primordial plasma and have travelled through the universe. Since the CMB

[1] M_{P} indicates the energy scale of the theory including the gravity. Here, G is the gravitational constant.

spectrum depends on the amount of matters and energy, the relic density[2] of the baryonic matter[3] and the DM can be calculated. From the measurements of CMB by WMAP [10] and Planck [11], the relic density of baryonic matter ($\Omega_{\rm b}h^2$) and dark matter ($\Omega_{\rm DM}h^2$) was obtained to be

$$\Omega_{\rm b}h^2 = \begin{cases} 0.02264 \pm 0.00050 & \text{WMAP} \\ 0.02226 \pm 0.00023 & \text{Planck} \end{cases}, \quad \Omega_{\rm DM}h^2 = \begin{cases} 0.1138 \pm 0.0045 & \text{WMAP} \\ 0.1186 \pm 0.0020 & \text{Planck.} \end{cases} \tag{2.3}$$

These results indicate that the amount of DM is estimated to be about 80% of the total gravitationally attractive component in our universe. The estimated amount of the ordinary SM matter is only about 20%.

Weakly-Interacting Massive Particles (WIMPs) are ones of most favored candidates of the DM. They are electrically neutral and has weak-scale mass. If the WIMPs are generated with other particles together in the early universe, the WIMP number density matches the number density inferred from the cosmological observations. If the universe is dense and hot, the WIMPs are annihilated into lighter particles and vice-versa. Figure 2.3 shows the WIMP equilibrium density as a function of temperature. The $< \sigma v >$ is the thermal average of the annihilation cross section times relative velocity of two annihilating particles. As the universe cools down, WIMPs continue to annihilate until all WIMPs annihilate. The WIMPs drop out of the thermal equilibrium, which is called the freeze-out. After freeze-out, WIMP abundance remains constant. A particle with a weak interaction cross-section (red lines in Figure 2.3) would freeze-out to reproduce the observed relic density. A particle with electromagnetic or strong interaction cross-sections would produce smaller relic abundance due to the high annihilation efficiency. Therefore, the WIMPs are favored candidates of the DM.

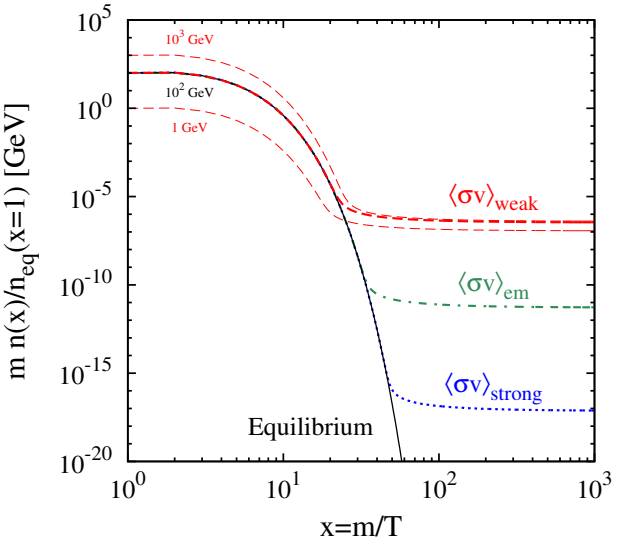

Figure 2.3: Evolusion of WIMP abundance as a function of the temperature (time). The solid line indicates the equilibrium density. The dashed lines indicate the relic densities for different annihilation cross-section and mass [8].

[2]Relic density or abundance is that the density of a matter remained in the universe.
[3]Baryonic matter refers to ordinary matter made out of nucleons and electrons.

2.2 Supersymmetry

SUSY [12–20] is the expansion theory of SM to introduce the symmetry between fermion and boson. An operator (Q) is introduced that it transforms a bosonic state into a fermionic state and vice-versa as

$$Q\,|\text{Boson}\rangle = |\text{Fermion}\rangle\,, \quad Q\,|\text{Fermion}\rangle = |\text{Boson}\rangle\,. \tag{2.4}$$

Q and $Q^\dagger$ (the hermitian conjugate of Q) is the anticommuting spinors and a conserved quantity that is not to change a mass of particles. SUSY is formed with the representation of the SUSY algebra called supermultiplet. The SUSY particles (sparticles) or the superpartners is the partners of the SM particles.

The MSSM [21] is one of the simplest models of SUSY to satisfy the requirements of SM. The points of MSSM are following items:

- the boson and the fermion represent the different quantum states of one particle;
- sparticles counterpart of each SM particle exists;
- the sparticles of the SM fermions have bosonic states with spin 0;
- the sparticles of the SM bosons have fermionic states with spin 1/2;
- when the SUSY is not broken, the mass of a particle and its sparticle is same;
- the Higgs bosons are originating from two complex SU(2) doublets.
- the R-parity ($R = (-1)^{2s+3(\text{B-L})}$, where s is the spin, and B, L are the numbers of the quarks and the leptons.) conservation law exists.

There are two vacuum expectation values (VEVs), v_u, v_d, corresponding to each of the two complex Higgs doublets. The ratio of VEVs [21] is parametrized by the mixing angle β and the vacuum expectation value in the SM (v_{SM}) is defined as

$$v_u^2 + v_d^2 = v_{\text{SM}}^2 = \frac{2m_Z^2}{g + g'},\ \frac{v_u}{v_d} = \tan\beta \tag{2.5}$$

where g and g' are the gauge coupling constants. The R-parity conservation law means that the decayed particles from a sparticle must contain a sparticle. Thus, the LSP, which is a electrically neutral particle with a lightest mass and stable, must be appeared under the R-parity conservation law. All of the supermultiplets are shown in Table 2.1. There are sparticles called gauginos corresponding to the gauge bosons of the SM. Two independent scalar boson sparticle ($\tilde{q}_{\text{L}}, \tilde{q}_{\text{R}}, \tilde{\ell}_{\text{R}}, \tilde{\ell}_{\text{L}}$) correspond to two types of the states of the fermions. The masses of bosons and fermions are different after the SUSY breaking. There are eight independent Higgs components generated from the SU(2) Higgs doublets. Since the three components are absorbed to give the masses for $W^\pm, Z$, the five Higgs bosons and the five higgsino are appeared. The quantum numbers of SU(3)_{C}, SU(2)_{L}, U(1)_{Y} for the particles and its sparticles are same.

If the SUSY is unbroken under the symmetry, the masses of sparticles are the same as the masses of SM particles, e.g. the masses of selectrons $\tilde{e}_{\text{L}}$ and $\tilde{e}_{\text{R}}$ are exactly equal to $m_e = 0.511$ MeV, and sparticles are easy to be discovered at previous experiments. However, the sparticles have not been discovered yet. This result indicates that SUSY is broken in vacuum states chosen in by the nature[4]. The effective MSSM Lagrangian including the SUSY breaking based on the SSB [21] can be defined as

$$\mathcal{L}_{\text{eff}}^{\text{MSSM}} = \mathcal{L}_{\text{inv.}}^{\text{MSSM}} + \mathcal{L}_{\text{soft}}^{\text{MSSM}}. \tag{2.6}$$

[4]This mean is that SUSY breaking is based on the SSB.

Table 2.1: Supermultiplets in the MSSM [21]. The upper part shows the gauge supermultiplets. The bottom part shows the chiral supermultiplets including the complex scalers with spin-0, the left-handed two-component Weyl fermions with spin-1/2, the right-handed singlelet Weyl fermion, and the Higgs doublets.

Names		spin-1	spin-1/2	$\mathrm{n(SU(3)_C), n(SU(2)_L), n(U(1)_Y)}$
gluino, gluon		g	$\tilde{g}$	$(8,1,0)$
winos, W boson		$W^{\pm}$, W^0	$\tilde{W}^{\pm}$, $\tilde{W}^0$	$(1,3,0)$
binos, B boson		B^0	$\tilde{B}^0$	$(1,1,0)$
Names		spin-0	spin-1/2	$\mathrm{n(SU(3)_C), n(SU(2)_L), n(U(1)_Y)}$
squarks, quarks	Q	$(\tilde{u}_\mathrm{L}, \tilde{d}_\mathrm{L})$	$(u_\mathrm{L}, d_\mathrm{L})$	$(3,2,\frac{1}{6})$
($\times$ 3 families)	$\bar{u}$	$\tilde{u}^*_R$	$u^\dagger_R$	$(3,1,-\frac{2}{3})$
	$\bar{d}$	$\tilde{d}^*_R$	$d^\dagger_R$	$(3,1,\frac{1}{3})$
sleptons, leptons	L	$(\tilde{\nu}_\mathrm{L}, \tilde{e}_\mathrm{L})$	$(\nu_\mathrm{L}, e_\mathrm{L})$	$(1,2,-\frac{1}{2})$
($\times$ 3 families)	$\bar{e}$	$\tilde{e}^*_R$	$e^\dagger_R$	$(1,1,1)$
Higgs, Higgsino	H_u	(H^+_u, H^0_u)	$(\tilde{H}^+_u, \tilde{H}^0_u)$	$(1,2,\frac{1}{2})$
	H_d	(H^0_d, H^-_d)	$(\tilde{H}^0_d, \tilde{H}^-_d)$	$(1,2,-\frac{1}{2})$

The first term ($\mathcal{L}^{\mathrm{MSSM}}_{\mathrm{inv.}}$) contains the invariant part of the MSSM and the second term ($\mathcal{L}^{\mathrm{MSSM}}_{\mathrm{soft}}$) consists of sparticle mass terms including the Higgs potential. The effect of SSB appears in the second term and this SUSY breaking is called soft SUSY breaking.

To introduce SUSY as extension of the SM, the stop ($\tilde{t}$) appears as the superpartner of the SM. Stop couples to the Higgs boson with the coupling constant $\lambda_{\tilde{t}}$, and the new Lagrangian term $\mathcal{L}_{\tilde{t}} \sim \lambda_{\tilde{t}}|H|^2|\tilde{t}|^2$. As a result, the one-loop radiative correction to the Higgs mass squared has additional contribution described in Figure 2.4.

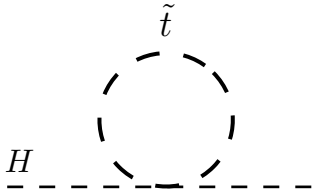

Figure 2.4: The illustration of Feynman diagrams for one-loop contribution of to the Higgs boson mass squared m^2_h, due to a scaler top quark.

The correction for stop [21] is written as

$$\Delta m^2_{h_{\tilde{t}}} = \lambda_{\tilde{t}}[\Lambda^2_{\mathrm{UV}} - m^2_{\tilde{t}} \ln \frac{\Lambda_{\mathrm{UV}}}{m_{\tilde{t}}} + \cdots], \tag{2.7}$$

where $m_{\tilde{t}}$ is the stop mass. The radiative correction [21] is the sum of the radiative corrections for the top quark (fermion) and the stop (boson) $\Delta m^2_{\mathrm{h}} \sim \Delta m^2_{\mathrm{h}_t} + \Delta m^2_{\mathrm{h}_{\tilde{t}}}$ and is written as

$$\Delta m^2_h \sim C \ln \frac{\Lambda_{\mathrm{UV}}}{m_{\tilde{t}}} + \cdots, \tag{2.8}$$

where C is the constant value corresponding to the masses of the top quark and stop. The first term of equation

(2.2) is canceled by $\Delta m_{\mathrm{h}_{\tilde{t}}}$. The remaining term is the log term of the ratio of $\Lambda_{\mathrm{UV}}/m_{\tilde{t}}$ and the level of fine-tuning is scaled down to the log scale. There is another benefit to introduce the SUSY. The LSP can be the DM candidate.

2.2.1 The Mass Spectrum of the MSSM

Neutralino and Chargino

The higgsinos and the electroweak gauginos mix with each other due to the Electro-Weak-Symmetry-Breaking. The neutralino is the four mass eigenstates formed by mixing the neutral higgsinos and the neutral gaugino ($\tilde{N}_i, i = 1, 2, 3, 4$). The chargino is the two mass eigenstates formed by mixing the charged higgsinos and the charged gaugino ($\tilde{C}_i, i = 1, 2$). In the gauge eigenstate for neutralino and chargino [21]: $\psi^0 = (\tilde{B}, \tilde{W}^0, \tilde{H}_d^0, \tilde{H}_u^0)$, $\psi^{\pm} = (\tilde{W}^+, \tilde{H}_u^+, \tilde{W}^-, \tilde{H}_d^-)$, these mass terms are sourced by MSSM Lagrangian and they can be written as

$$\mathcal{L}_{\tilde{N}\ \mathrm{mass}} = -\frac{1}{2}(\psi^0)^T \boldsymbol{M}_{\tilde{N}} \psi^0 + c.c., \tag{2.9}$$

$$\mathcal{L}_{\tilde{C}\ \mathrm{mass}} = -\frac{1}{2}(\psi^{\pm})^T \boldsymbol{M}_{\tilde{C}} \psi^{\pm} + c.c. \tag{2.10}$$

$$\tag{2.11}$$

where the $\boldsymbol{M}_{\tilde{N},\tilde{C}}$ is the mass matrices. The mass matrix for neutralinos is given as

$$\begin{pmatrix} M_1 & 0 & -\cos\beta\sin\theta_W m_Z & \sin\beta\sin\theta_W m_Z \\ 0 & M_2 & \cos\beta\cos\theta_W m_Z & -\sin\beta\cos\theta_W m_Z \\ -\cos\beta\sin\theta_W m_Z & \cos\beta\cos\theta_W m_Z & 0 & -\mu \\ \sin\beta\sin\theta_W m_Z & -\sin\beta\sin\theta_W m_Z & -\mu & 0 \end{pmatrix} \tag{2.12}$$

where M_1, M_2, and μ are the masses of the bino, wino and higgsino and θ_W is the mixing angle generated from the weak neutral current interaction of the SM ($e = g\sin\theta_W = g'\cos\theta_W$). The neutralino mass eigenvalues given by the mass matrix [21] can be written as

$$m_{\tilde{N}_1} = M_1 - \frac{m_Z^2 \sin^2\theta_W}{\mu^2 - M_1^2}(M_1 + \mu\sin 2\beta) \tag{2.13}$$

$$m_{\tilde{N}_2} = M_2 - \frac{m_W^2}{\mu^2 - M_1^2}(M_2 + \mu\sin 2\beta) \tag{2.14}$$

$$m_{\tilde{N}_3} = |\mu| + \frac{m_Z^2}{2(\mu + M_1)(\mu + M_2)}(I - \sin 2\beta)(\mu + M_1\cos^2\theta_W + M_2\sin^2\theta_W) \tag{2.15}$$

$$m_{\tilde{N}_4} = |\mu| + \frac{m_Z^2}{2(\mu - M_1)(\mu - M_2)}(I + \sin 2\beta)(\mu - M_1\cos^2\theta_W - M_2\sin^2\theta_W) \tag{2.16}$$

where M_1 and M_2 are real and positive, and the μ is real with sign $I = \pm 1$. Each neutralino has different mixing between the electroweak gauginos and higgino: $\tilde{N}_1$ is a "bino-like"; $\tilde{N}_2$ is a "wino-like"; $\tilde{N}_{3,4}$ is a "higgsino-like". The mass matrix ($M_{\tilde{C}}$) for chargino [21] is given as

$$\boldsymbol{M}_{\tilde{C}} = \begin{pmatrix} \boldsymbol{0} & \boldsymbol{X}^T \\ \boldsymbol{X} & \boldsymbol{0} \end{pmatrix},\ \boldsymbol{X}_= \begin{pmatrix} M_2 & \sqrt{2}\sin\beta m_W \\ \sqrt{2}\cos\beta m_W & \mu \end{pmatrix}. \tag{2.17}$$

The chargino mass eigenstates [21] can be written as

$$m_{\tilde{C}_1} = M_2 - \frac{m_W^2}{\mu^2 - M_2^2}(M_2 + \mu\sin 2\beta) \tag{2.18}$$

$$m_{\tilde{C}_2} = |\mu| + \frac{m_W^2 I}{\mu^2 - M_2^2}(\mu + M_2\sin 2\beta). \tag{2.19}$$

Each chargino has different mixing between the wino and higgino: $\tilde{C}_1$ is a "wino-like", $\tilde{C}_2$ is a "higgsino-like".

In this thesis, the neutralinos and charginos are denoted as $\tilde{\chi}_i^0$, $(i = 1, 2, 3, 4)$ and $\tilde{\chi}_j^{\pm}$, $(j = 1, 2)$, where i and j are given in order of their mass (e.g. $m_{\tilde{\chi}_1^0} < m_{\tilde{\chi}_2^0} < m_{\tilde{\chi}_3^0} < m_{\tilde{\chi}_4^0}$).

Scalar Top Quarks

In the MSSM, any scalar particles with the electric charge, the R-parity and the color can mix with each other because the soft terms of MSSM Lagrangian is completely arbitrary. The mass eigenstates of the squarks and sleptons are obtained by the squared-mass matrices and the Yukawa coupling matrices which have the copuling parameters ($\boldsymbol{y} = (y_t, y_b, y_\tau)$ and A_t is the third component of the scalar coupling parameter $\boldsymbol{a_u}$). The off-diagonal components of the mass matrices or Yukawa coupling matrices of the first- and second-generations for the squarks and sleptons are negligibly small. On the other hand, the third generation sparticles, stops, sbottoms, and the staus, are strongly affected from the off-diagonal components. Thus, the mass eigenstates of the third generation sparticles are obtained by L-R mixing. To focus on the stops, the mass eigenstates $(\tilde{t}_1, \tilde{t}_2)$ are given by diagonalizing 2×2 mass matrix:

$$\begin{pmatrix} m^2_{\tilde{t}_{\mathrm{L}}} & y_t v \sin\beta(A_t - \mu \cot\beta) \\ y_t v \sin\beta(A_t - \mu * \cot\beta) & m^2_{\tilde{t}_{\mathrm{R}}} \end{pmatrix}. \tag{2.20}$$

2.2.2 Naturalness for 125 GeV Higgs

After the cancellation of the quadratic term in the radiative correction of the Higgs boson mass, the following two point should be discussed. The first point is that the fine tuning should be as small as possible in for the naturalness. The second point is that the observed Higgs mass is near 125 GeV [22, 23]. The observed Higgs mass squared [22] is defined as

$$m_h^2 = M_Z^2 \cos^2 2\beta + \delta_t^2 \tag{2.21}$$

where $M_Z^2 \cos^2 2\beta$ is the bare Higgs mass and δ_t^2 is the loop contribution of the top and stop after the renormalization. Assuming $\cos^2 2\beta \sim 1$, the δ_t is required to be ~ 85 GeV by the limit from masses of observed Higgs and Z boson at the tree-level. Considering the one-loop level correction of stop, δ_t [22] can be written as

$$\delta_t^2 \sim \frac{3}{(8\pi)^2}\frac{m_t^2}{v^2}[\ln\frac{m_{\tilde{t}}}{m_t^2} + \frac{X_t^2}{m_{\tilde{t}^2}}(1 - \frac{X_t^2}{12m_{\tilde{t}}^2})] \tag{2.22}$$

where m_t is the top quark mass, $m_{\tilde{t}}$ is the stop mass which is not same as the mass eigenstate of stop. Since the dominantly one-loop contribution depends on the geometric mean of stop masses $m_{\tilde{t}}^2 = m_{Q_3} m_{u_3}$ where m_{Q_3} and m_{u_3} are the left and right-handed top squark mass parameters, this correction also largely depends on the light stop mass ($m_{\tilde{t}_1}$) and its mixing parameter $X_t = A_t - \mu \cot\beta$. When the mixing parameter is required to be maximum, $X_t^{\max} = \sqrt{6} m_{\tilde{t}}$. Figure 2.5 shows the Higgs mass calculated at the two loop in the MSSM as a function of the light stop mass for two values of the top squarks mixing parameter. In this calculation, large $\tan\beta$ is assumed ($\tan\beta = 20$). The red/blue bands are computed by using different calculators: Suspect, FeynHiggs. In the case of no mixing ($X_t = 0$), the Higgs mass is not allowed at 125 GeV. On the other hand, in the case of maximal mixing, the mixed stop mass ($m_{\tilde{t}_1}$) is not required to be heavy for 125 GeV Higgs.

The Higgs potential at the tree-level [22] is defined as:

$$V = m_H^2 |h|^2 + \frac{\lambda_h}{4}|h|^4. \tag{2.23}$$

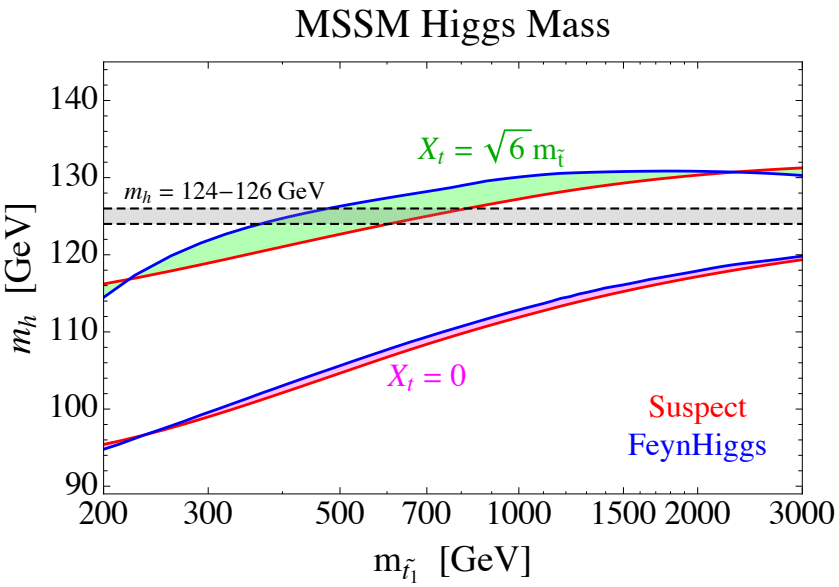

Figure 2.5: The relation between the lightest stop mass and the Higgs mass [22].

The mass of tree-level Higgs (m_h) is related with the quadric term of the potential, $m_h^2 = 2\lambda_h v^2 = -4m_H^2$. The amount of the fine tuning [22] is determined by the Higgs mass at the tree-level and the amount of the correction in this quadric potential, $\delta m_{H_u}^2$,

$$\delta m_{H_u}^2 = -\frac{3y_t^2}{8\pi^2}(m_{Q_3}^2 + m_{u_3}^2 + |A_t|^2)\ln(\frac{\Lambda}{m_{\tilde{t}}}), \tag{2.24}$$

where Λ is the scale of SUSY breaking. The parameter for the fine tuning (Δ_{m_h}) [22] can be written as the m_h^2 and the fundamental parameters (p_i) defined by Λ: μ, $B\mu$, $m_{Q_3}^2$, $m_{u_3}^2$, $m_{H_u}^2$, and $m_{H_d}^2$, and then it becomes:

$$\Delta_{m_h} = \max|\frac{\partial \ln m_h^2}{\partial \ln p_i}|. \tag{2.25}$$

The inverse of Δ_{m_h} indicates the accuracy (%) of the fine tuning, and for example, if the Δ_{m_h} is large, it indicates that precise fine tuning is required. Figures 2.6 show the contours of m_h in the MSSM as a function of a common stop mass $m_{Q_3} = m_{u_3} = m_{\tilde{t}}$ and the mixing parameter X_t, for $\tan\beta = 20$. The red/blue bands show the allowed region with 124-126 GeV Higgs. The left plot shows the relation between the ratio ($X_t/m_{\tilde{t}}$) and stop mass ($m_{\tilde{t}}$), and the dash purple lines show the amount of the fine tuning. The right plot also shows the relation between the ratio and the stop mass, and the dash green lines show the mixed stop mass ($m_{\tilde{t}_1}$). These plots indicate that even for the 125 GeV Higgs boson mass, it is possible to reduce the amount of the fine tuning to a few %. The stop mass and the Higgs mass are controlled by the μ parameter. Therefore, the higgsino should be small and be favored as LSP due to the requirement of light stop mass.

To be more natural (very small fine tuning), there is the Next-to-Minimum Supersymmetric Standard Model (NMSSM). NMSSM introduces the new singlet superfield that couples to the Higgs in the superpotential, $\lambda S H_u H_d$. The SM higgs mass of the lightest CP-even scaler at the tree-level [22] can be redefined by the λ term corresponding to the new singlet (S) and it is written as:

$$|m_h|^2_{\text{tree}} \leq m_Z^2 \cos^2 2\beta + \lambda\nu^2 \sin^2 2\beta + \delta_t^2, \tag{2.26}$$

where δ_t is included the loop corrections. The first term is the upper bound of MSSM and the second term is the contribution of the new singlet. The bound is saturated when the singlet is integrated out with a large

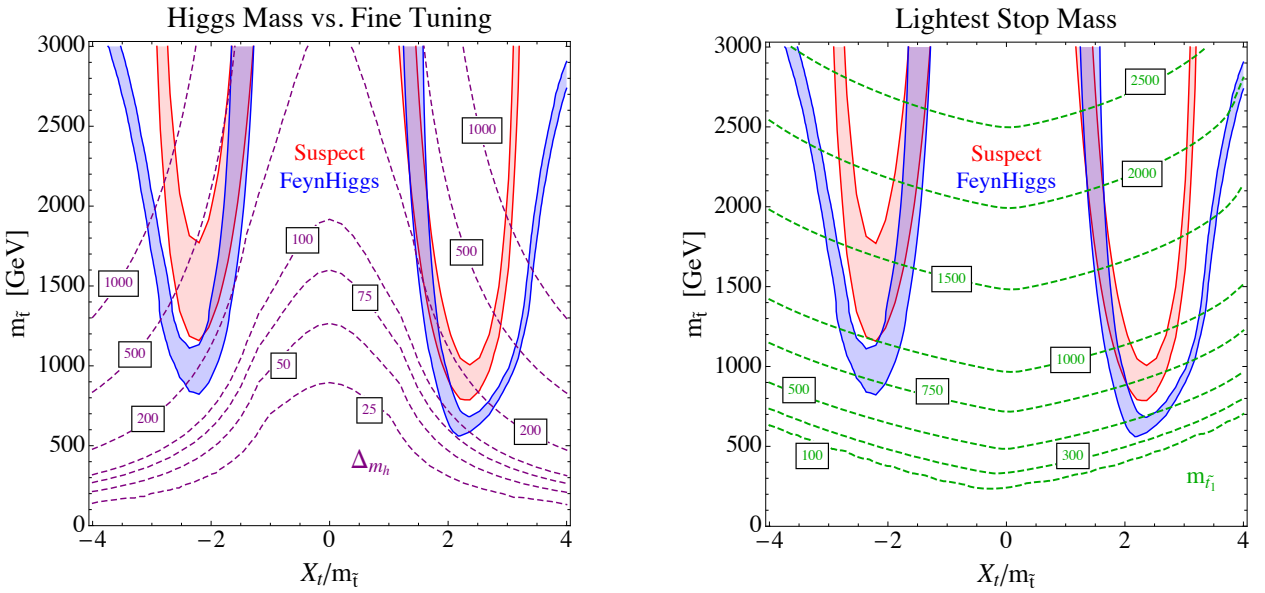

(a) (b)

Figure 2.6: The relation between mixing parameter (X_t), stop mass ($m_{\tilde{t}}$), the amount of the fine tuning (Δ_{m_h}), and the mixed stop mass ($m_{\tilde{t}_1}$) assuming MSSM, $m_{Q_3} = m_{u_3} = m_{\tilde{t}}$ and $\tan\beta = 20$ GeV [22].

SUSY breaking mass, $m_S^2 > M_S^2$, which, in practice, can be realized with m_S several hundreds of GeV. The λ is constrained up to 0.7 for the perturbation to the unified scale, and the term including λ grows at the small $\tan\beta$. This means that the largest Higgs mass is achieved with low $\tan\beta$ and λ as large as possible (~ 0.7). The loop contribution is important and it should be needed because the $(m_h)^2_{\text{tree}}$ without this correction is always smaller than 122 GeV. Figure 2.7 shows the relation between the ratio ($X_t/m_{\tilde{t}}$) and the stop mass and the dash purple lines show the amount of the fine tuning. To compare between Figure 2.6(left) and this plot, the accuracy of fine tuning in the NMSSM can be smaller than MSSM.

2.2.3 DM Candidates with the Well-Tempered Neutralino

There are three candidates of the LSP/DM in SUSY [24]; pure bino ($\tilde{B}$), pure higgsino ($\tilde{H}$), and pure wino ($\tilde{W}$). First, to consider the pure bino LSP, the bino annihilation occurs in the early universe through the squarks and sleptons exchange. The contribution of the bino annihilation for Ω_{DM} [24] can be approximated as:

$$\Omega_{\tilde{B}}h^2 = 1.3\times10^{-2}\left(\frac{m_{\tilde{e}_R}}{100\text{GeV}}\right)^2 \times \frac{(1+r)^4}{r(1+r^2)}\left(1+0.07\log\frac{\sqrt{r}100\text{GeV}}{m_{\tilde{e}_R}}\right), \tag{2.27}$$

where r is the squared ratio of the bino mass and three degenerated right-handed slepton mass ($m_{\tilde{e}_R}$). Pure bino LSP scenario assuming $r \leq 0.9$, which does not degenerate the bino and slepton, gives the relic density too high.

Second, to consider the pure Higgsino LSP, it is promising candidate traditionally because the annihilation cross-section is more effective. The annihilation channel into the gauge boson, and in addition, the co-annihilation should be important because the chargino and neutralino should be degenerated for the higgsino LSP. A large higgisno mass is need to cancel the positive contribution to M_Z^2. The relic density for the

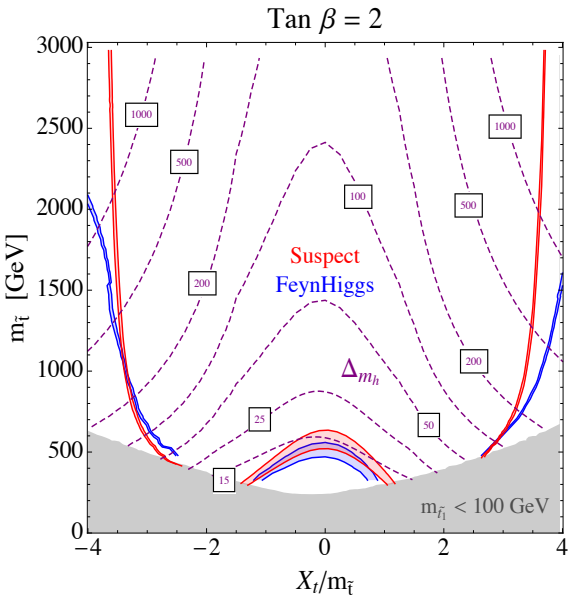

Figure 2.7: The relation between mixing parameter (X_t), stop mass ($m_{\tilde{t}}$), the amount of the fine tuning (Δ_{m_h}), and the mixed stop mass ($m_{\tilde{t}_1}$) assuming NMSSM, $m_{Q_3} = m_{u_3} = m_{\tilde{t}}$ and $\tan\beta = 2$ GeV [22].

pure higgsino LSP [24] can be approximated as:

$$\Omega_{\tilde{H}} h^2 = 0.11(\frac{\mu}{1\text{TeV}})^2. \tag{2.28}$$

Thus, the relic density is too low, and to fix this, the Higgsino must have a large mass with TeV-scale.

Third, the pure wino LSP can be considered, and the dominant annihilation is into the gauge boson same as the pure higgsino LSP. The approximation of relic density of the pure wino [24] is:

$$\Omega_{\tilde{W}} h^2 = 0.13(\frac{M_2}{2.5\text{TeV}})^2. \tag{2.29}$$

Likewise the higgsino LSP case, wino mass larger than 2.5 TeV is need. The models of pure higgsino and wino LSP requiring the large mass over the TeV scale have other problem such as the natural SUSY described in Section 2.2.2.

The component of neutralino may not be the pure bino, higgsino, wino, and more likely a mixture of them in the nature, if anything, there is some possibility of favoring to be mixed neutralino in the nature [24,25]. The annihilation channels increase more and the Ω_{DM} can be reproduced by mixing components. However, when the mixed neutralino is considered, the m_Z values included in the soft term of SUSY is also need to be taken care for the natural SUSY. One of the simple mixing neutralino is built by the bino LSP and wino Next-to-Lightest Supersymmetric Particle (NLSP). This model reduces the relic density of dark matter by using the small fine tuning for these mass parameters. The effective mass matrix for bino/wino mixing [24] is defined as:

$$M = \begin{pmatrix} M_1 & 0 \\ 0 & M_2 \end{pmatrix} - \sin 2\beta \frac{M_Z^2}{\mu} \begin{pmatrix} \sin^2\theta_W & -\sin\theta_W\cos\theta \\ -\sin\theta_W\cos\theta & \cos^2\theta_W \end{pmatrix} + O(\frac{1}{\mu^2}) \tag{2.30}$$

where θ_W is the mixing angle of SM and this equation is assumed $M_1 \sim M_2$. The bino/wino mixing angle θ, $1/\mu^2$ term and the ratio of bino/wino masses [24] are also defined as:

$$\theta \equiv \frac{\sin 2\theta_W \sin 2\beta M_Z^2}{2\mu\Delta M_1},\ \delta \equiv \frac{\sin 2\theta_W M_Z^2}{2\mu^2\Delta},\ \Delta \equiv \frac{M_2 - M_1}{M_1}. \tag{2.31}$$

In the case of $M_1 \sim M_2$ such as $M_1 - M_2 \sim 0$, θ and δ becomes larger than unity, and θ can be θ_W. The masses of the lightest and 2nd lightest neutralinos and the lightest chargino [24] can be approximated as:

$$m_{\tilde{\chi}_1^0} = M_1, \tag{2.32}$$

$$m_{\tilde{\chi}_2^0} = M_1(1 - \frac{\sin^2 2\beta M_Z^2}{\mu M_1} - \frac{M_Z^2}{\mu^2}), \tag{2.33}$$

$$m_{\tilde{\chi}_1^\pm} = M_1(1 - \frac{\sin^2 2\beta M_W^2}{\mu M_1} - \frac{M_W^2}{\mu^2}). \tag{2.34}$$

Therefore, if the degeneration between M_1 and M_2 is assumed around 10%, The neutralino that is the candidate of dark matter can have the mass around few hundreds GeV.

2.2.4 Current Exclusion Limit of Direct Stop Pair Production

The stop pair productions with the *pp* collisions are continuously and widely searched by the ATLAS and CMS experiments. Unfortunately, there are no evidences of that, and it is interpreted into constrains on the models. In this section, some direct stop pair production searches at the ATLAS and CMS are reviewed.

$\tilde{t}_1 \to b\tilde{\chi}_1^\pm$ decay channel is motivated by the higgsino LSP scenario for the naturalness and the bino LSP and the wino NLSP scenario for the DM. Figure 2.8 show the exclusion limit of $\tilde{t}_1 \to b\tilde{\chi}_1^\pm$ process for the higgsino LSP scenario. Since the stop modeled by higgsino LSP scenario can decay either into $t\tilde{\chi}_1^0$, $b\tilde{\chi}_1^\pm$, and $t\tilde{\chi}_2^0$, the CMS experiment assumes the mixing of decay channels with the half of branching ratio (BR). The ATLAS experiment also assumes the mixing described in Figure 2.9 at the Run-2 [26]. These processes are excluded up to about 1000 GeV of stop mass, however the boundary region nearby $m_{\tilde{t}_1} < m_b + m_{\tilde{t}_1^\pm}$ have not been searched yet.

Figure 2.10 show the exclusion limit of $\tilde{t}_1(\tilde{b}_1) \to b\tilde{\chi}_1^\pm$ process for the bino LSP and wino NLSP scenario. These processes are excluded up to about 900 GeV of stop (sbottom) mass for the scenario with $m_{\tilde{\chi}_1^\pm} = 2m_{\tilde{\chi}_1^0}$ condition, however the scenario with $\Delta m(\tilde{t}_1, \tilde{\chi}_1^\pm) = 10$ GeV excluded only about 450 GeV.

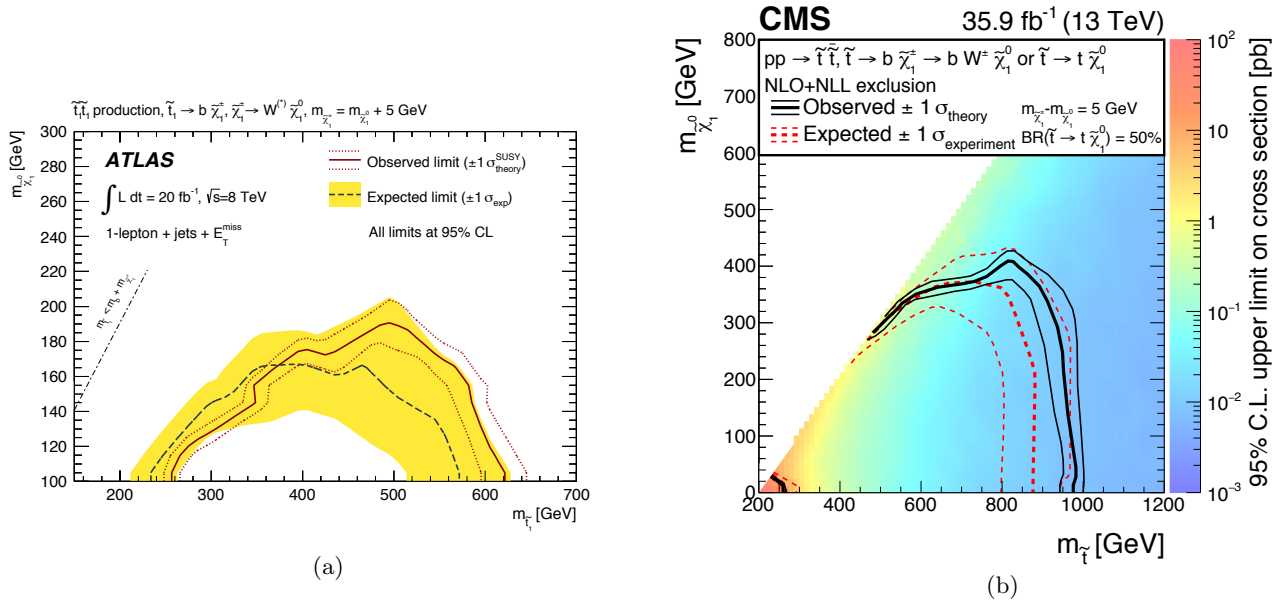

(a) (b)

Figure 2.8: The exclusion limits of the direct stop pair production decayed to $t\tilde{\chi}_1^0$ or $b\tilde{\chi}_1^\pm$ with $\Delta m(\tilde{\chi}_1^\pm, \tilde{\chi}_1^0) = 5$ GeV at pp collisions in (a) the ATLAS experiment [27] and (b) CMS experiment [28].

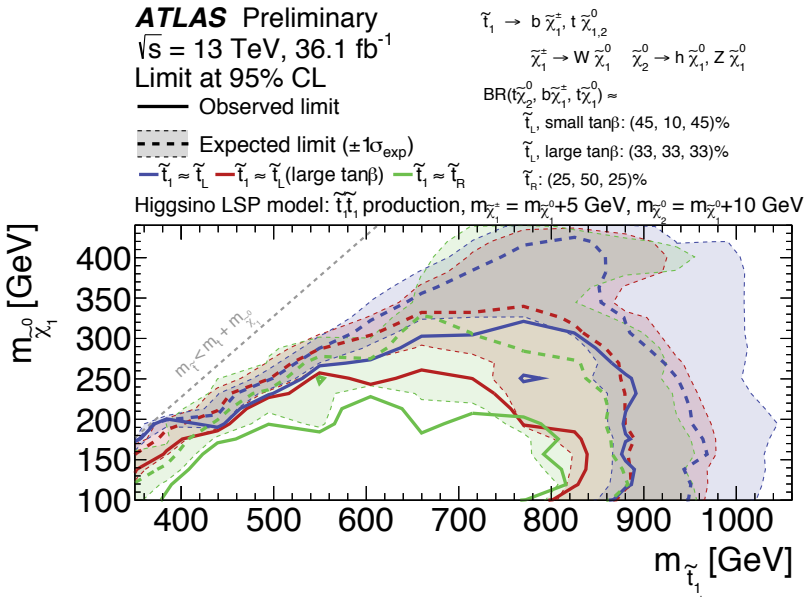

Figure 2.9: The exclusion limits of the direct stop pair production decayed to $t\tilde{\chi}_1^0$, $b\tilde{\chi}_1^\pm$, and $t\tilde{\chi}_2^0$ with $\Delta m(\tilde{\chi}_1^\pm, \tilde{\chi}_1^0) = 5$, $\Delta m(\tilde{\chi}_1^0, \tilde{\chi}_0^2) = 10$ GeV at pp collisions in the ATLAS experiment [26].

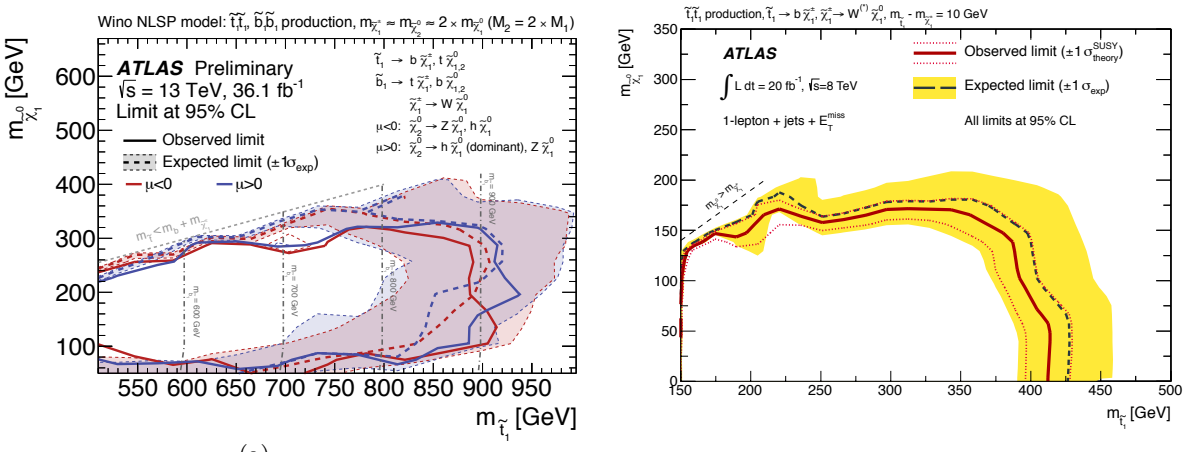

(a) (b)

Figure 2.10: The exclusion limits of the direct stop (sbottom) pair production decayed to $b\tilde{\chi}_1^\pm$ with (a) $m_{\tilde{\chi}_1^\pm} = 2m_{\tilde{\chi}_1^0}$ GeV [26], with (b) $\Delta m(\tilde{t}_1, \tilde{\chi}_1^\pm) = 10$ GeV [27] at pp collisions in the ATLAS experiment.

2.3 Target Scenarios for the Stop

We focus on searches in two compressed scenarios with final state of one isolated lepton, jets, and $E_{\mathrm{T}}^{\mathrm{miss}}$: (a) Higgsino LSP, (b) Wino NLSP. These scenarios assume some requirements such as:

- R-parity conservation;
- The neutralino is LSP;
- Decay channel: $\tilde{t}_1 \rightarrow b + \tilde{\chi}_1^\pm$ with BR($\tilde{t}_1 \rightarrow b + \tilde{\chi}_1^\pm$) = 100%.

Figure 2.11 shows the Feynman diagram of the target scenarios. The neutralinos, which appear as the LSPs from decays of the charginos, can not be detected similarly to the neutrino in the ATLAS detector, and become missing transverse energy ($E_{\mathrm{T}}^{\mathrm{miss}}$). One W boson decays to a lepton and a neutrino, and the other W boson decays into the hardonic jets. The neutrino also becomes the $E_{\mathrm{T}}^{\mathrm{miss}}$.

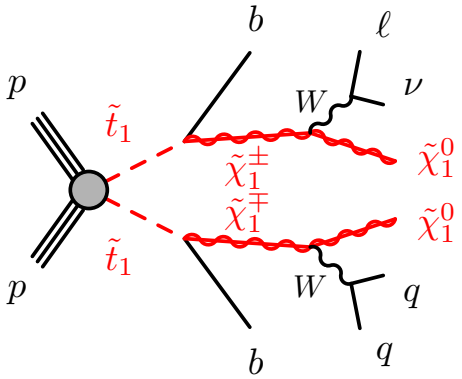

Figure 2.11: Feynman diagram of $\tilde{t}_1 \rightarrow b + \tilde{\chi}_1^\pm$ decay channel. The chargino decays into a W boson and a neutralino that is LSP for R-parity conservation. Large $E_{\mathrm{T}}^{\mathrm{miss}}$ is expected because of neutralinos and one neutrino originated from W boson.

(a) Higgsino LSP

Assuming the naturalness described in the Section 2.2.2, the higgsino mass must be small and the $\tilde{\chi}_1^\pm$ and $\tilde{\chi}_1^0$ mixing to form the mass eigenstates are favored to compress. This scenario is considered for a simplified model that the LSP is higgsino ($N_{3,4} \sim \tilde{\chi}_{1,2}^0$) and the bino and the wino are decoupled. Figure 2.12 shows the sparticle mass spectrum for the higgsino LSP scenario. Assuming these assumptions, the chargino of NLSP is also to be the higgsino-like same as the second component ($C_2 \sim \tilde{\chi}_1^\pm$).

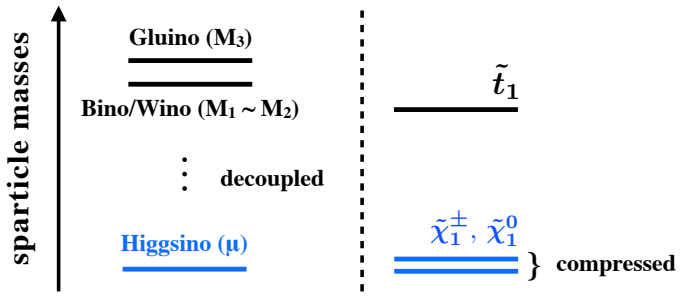

Figure 2.12: The mass spectrum of sparticles for the higgsino LSP scenario. The analysis of this thesis assumes that the higgsino decouple the bino and wino. In addition, the mass difference between chargino and the neutralino is compressed.

Figure 2.13 shows the searched two-dimensional mass plane ($m_{\tilde{t}_1}$, $m_{\tilde{\chi}_1^0}$). The stop can decay into either $b\tilde{\chi}_1^\pm$, $t\tilde{\chi}_1^0$, and $t\tilde{\chi}_2^0$, and these BRs depend on the $\tilde{t}_R$ and $\tilde{t}_L$ composition of the stop. The stop decaying into $t\tilde{\chi}_1^0$ and $t\tilde{\chi}_2^0$ are mostly originated from $\tilde{t}_L$, and the stop decaying into $b\tilde{\chi}_1^\pm$ from $\tilde{t}_R$. Therefore, in the boundary region stop is not able to decay into top quarks depending on $b\tilde{\chi}_1^\pm$, and we assume $\mathrm{BR}(\tilde{t}_1 \to b\tilde{\chi}_1^\pm) = 100\%$. It is possible to use simplified MC simulation for the stop pair production in the boundary region, however the stop is also degenerated for the chargino and the neutralino. Thus, the search becomes more difficult due to large backgrounds using final state particles with soft energy and momentum. On the other hand, other region where the stop can decay all channels should have mixing BRs of those channels. In this analysis, I focus and search on the boundary region with special kinematic selection assuming 5 GeV mass difference.

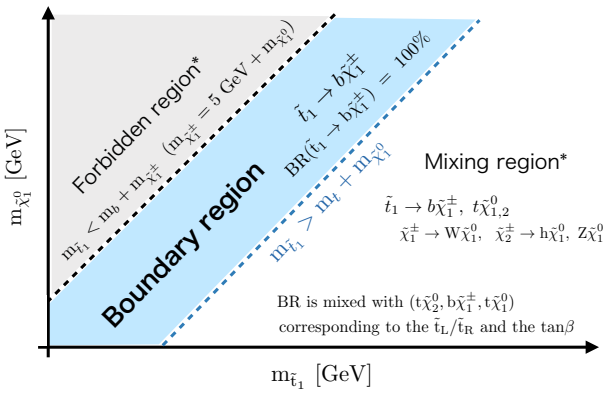

Figure 2.13: The illustration of the searched mass region in the two-dimensional mass plane ($m_{\tilde{t}_1}$, $m_{\tilde{\chi}_1^0}$). The boundary region depend on $b\tilde{\chi}_1^\pm$ channel and the mixing region depend on all channels. The search is almost impossible in the forbidden region because the final state particles have very soft energy and momentum, therefore, are not detectable in the ATLAS detector.

(b) Wino NLSP

From the point of view of the DM search, we consider the wino NLSP scenario, where the LSP and NLSP are the bino and wino ($N_{1,2} \sim \tilde{\chi}^0_{1,2}$). The stop in the wino NLSP scenario can decay into either $b\tilde{\chi}^\pm_1$, $t\tilde{\chi}^0_1$, and $t\tilde{\chi}^0_2$. We focus on the $b\tilde{\chi}^\pm_1$ simplified model with BR($\tilde{t}_1 \to b\tilde{\chi}^\pm_1$) = 100% assuming the mass difference between the stop and the chargino to be 10 GeV. Figure 2.14 shows the sparticle mass spectrum for the wino NLSP scenario. Assuming these assumptions, the chargino is to be wino-like same as the first component ($C_1 \sim \tilde{\chi}^\pm_1$).

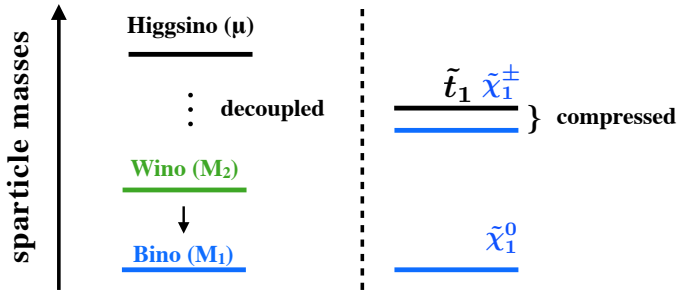

Figure 2.14: The mass spectrum of sparticles for the wino NLSP scenario. The analysis of this thesis assumes that the higgsino decouple the bino LSP and the wino NLSP. In addition, the mass difference between the stop and the chargino is assumed to be 10 GeV.

Figure 2.15 shows the searched mass region in the two-dimentional mass plane ($m_{\tilde{t}_1}$, $m_{\tilde{\chi}^0_1}$) for the wino NLSP scenario. Stop in model can be searched at widely mass plane to the boundary ($m_{\tilde{\chi}^\pm_1}$ ¡ $m_{\tilde{\chi}^0_1}$). Stop in this model could not be searched widely in the Run-1, and the obtained upper limit of stop mass was around 500 GeV.

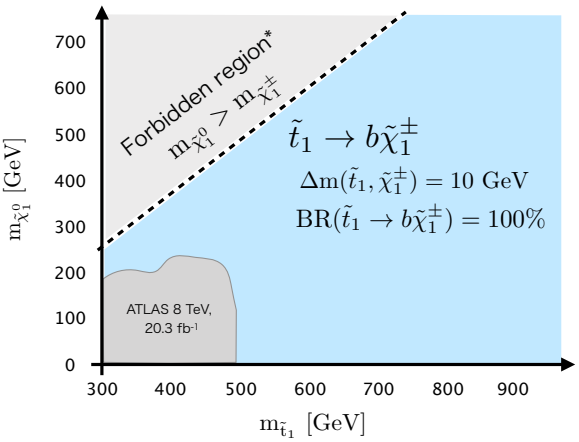

Figure 2.15: The illustration of two-dimentional searched mass region in the ($m_{\tilde{t}_1}$, $m_{\tilde{\chi}^0_1}$) plane. The $\tilde{t}_1 \to b\tilde{\chi}^\pm_1$ assuming BR($\tilde{t}_1 \to b\tilde{\chi}^\pm_1$) = 100% and the mass difference $\Delta m(\tilde{t}_1, \tilde{\chi}^\pm_1) = 10$ GeV can be searched widely for the wino NLSP scenario.

Chapter 3

Large Hadron Collider and ATLAS Detector

Signals expected by target scenarios of the stop pair production are searched for using data from LHC and ATLAS detector located at European Organization for Nuclear Research (CERN) in this analysis. The details of LHC and ATLAS detector are described in this chapter.

3.1 Large Hadron Collider

LHC shown in Figure 3.1 [29] is a circular accelerator with the pp collisions at CERN. There are four experiments (ATLAS, CMS, ALICE, LHCb) corresponding to the interaction points. The center-of-mass energy $\sqrt{s}$ of pp collisions is maximum 14 TeV.

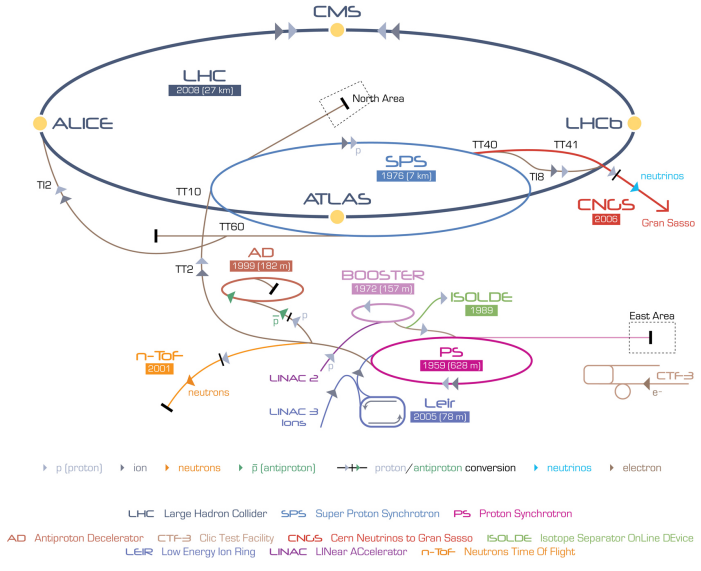

Figure 3.1: Schematic view of the CERN accelerator complex. There are 4 main experiments at the interaction points of LHC. Protons are generated by providing electromagnetic field for hydrogen gas. They are accelerated by some accelerators step-by-step such as protons → Linac2 (50 MeV) → Booster (1.4 GeV) → PS (25 GeV) → SPS (450 GeV) → LHC (7 TeV) [29].

Protons are accelerated with multistage accelerators. First, protons are generated from hydrogen gas and then accelerated to 50 MeV by a linear accelerator, Linac2. Thereafter, protons are accelerated to 1.4 GeV $\rightarrow$ 25 GeV $\rightarrow$ 450 GeV by several circular accelerators called by PSB, PS, and SPS respectively. Finally, protons are accelerated up to 7 TeV energy by LHC. Two proton beams are collided periodically in 25 ns time interval which is bunch spacing. A event rate is defined as:

$$\frac{dN}{dt} = \mathcal{L}_{\text{ins.}} \times \sigma. \tag{3.1}$$

The cross-section, σ, is the invariant physical quantity for interaction between two beams. The instantaneous luminosity $\mathcal{L}_{\text{ins.}}$, which indicates the quantity of the accelerator ability can be parametrized as:

$$\mathcal{L}_{\text{ins.}} = \frac{n_{\text{b}} f_{\text{r}} n_1 n_2}{2\pi \Sigma_{\text{x}} \Sigma_{\text{y}}}, \tag{3.2}$$

where n_1 and n_2 are beam populations, f_{r} is revolution frequency, n_{b} is the number of bunches, and Σ_{x} and Σ_{y} are beam width in x and y directions.

3.1.1 Data Taking in Run-2

The ATLAS experiment was started from 2009 and the run period, where the LHC ran with $\sqrt{s}$ = 7 (2011) and 8 (2012) TeV from 2011 to the end of 2012, was called Run-1. The maximum instantaneous luminosity was about $0.35 \times 10^{34}\text{cm}^{-2}\text{s}^{-1}$ and the integrated luminosities were about 6 fb^{-1} in 2011 and about 24 fb^{-1} in 2012. During the shutdown period, from 2013 to the end of 2014, the accelerator components such as beam pipe, magnets, etc. are upgraded for increasing energy and luminosity. The run period from 2015 to 2018, which is called Run-2, the LHC operates with $\sqrt{s}$ = 13 TeV and maximum $\mathcal{L}_{\text{ins.}} = 1.4 \times 10^{34}$ cm^{-2}s^{-1}. I used the *pp* collisions' data which were taken from 2015 to the end of the 2016 in Run-2. Figures 3.2 show the integrated luminosities in 2015 (a) and 2016 (b). The total delivered luminosity by LHC was 42.7 fb^{-1} and the total recorded luminosity in the ATLAS detector was 39.5 fb^{-1}. The loss of integrated luminosity is due to the detector or operation efficiency, but the high efficiency more than 90% was kept from 2015 to the end of 2016.

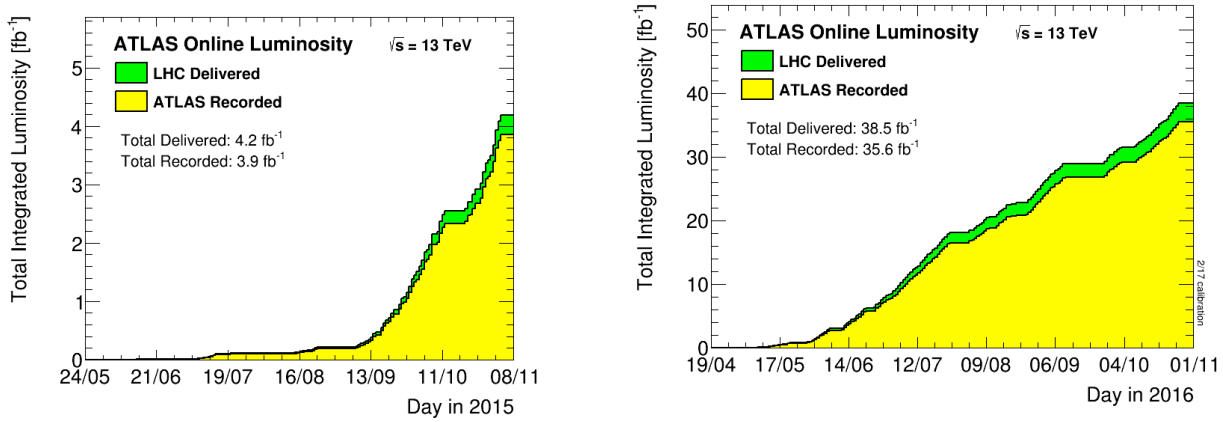

(a) (b)

Figure 3.2: The integrated luminosity in (a) 2015 and (b) 2016. The green histograms show the recorded (generated) luminosities in LHC and the yellow histograms show the recorded luminosities by using the ATLAS detector [30].

3.2 Overview of the ATLAS Detector

Figure 3.3(a) shows the schematic view of the ATLAS detector [31]. The detector is a cylindrical general purpose detector with the size of about 25 m diameter and about 44 m length. Inner detectors, a solenoid magnet, calorimeters, toroid magnets, and muon detectors are installed in this order from the innermost layer. This section introduces the coordinate system of ATLAS detector and the outline of each sub-detectors.

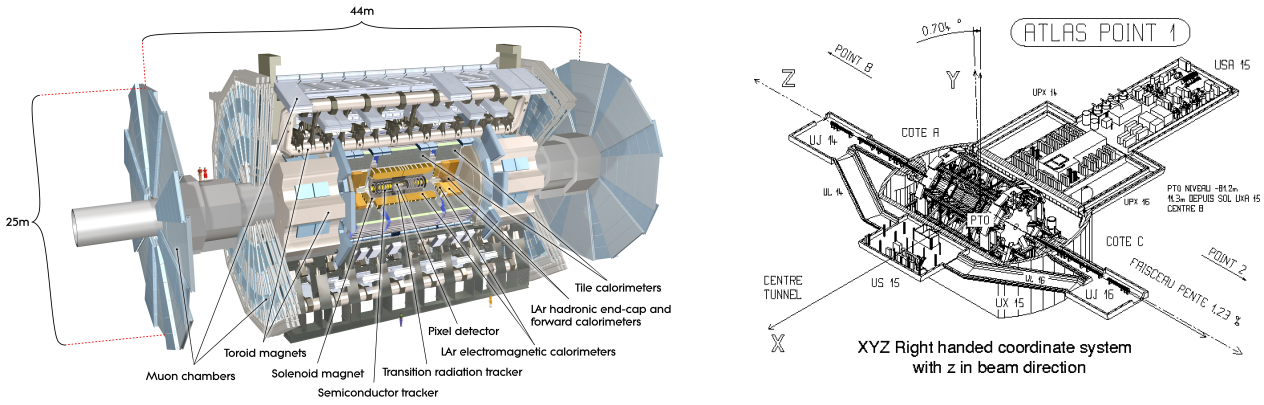

(a) (b)

Figure 3.3: (a) Schematic view of the ATLAS detector [31] and (b) the coordinate system of ATLAS [32]. This detector is a cylindrical generic detector with the size of ∼25 m diameter and ∼44 m length and it is constructed by subdetectors and magnets: the tracking inner detectors, the calorimeters, and the muon spectrometers. The center of LHC axis, the vertical of LHC axis, and the beam axis are defined as x-axis, y-axis, and z-axis, respectively.

3.2.1 The Coordinate System

The coordinate system of ATLAS detector is shown in Figure 3.3(b) [33]. The interaction point is defined as the origin. The Cartesian coordinate (x, y, z) is set as (horizontal direction, vertical direction, proton beam pipe direction). In addition, the length r $(= \sqrt{x^2 + y^2})$ in the transverse plane (x-y plane), the polar angle θ measured from the z-axis, and the azimuthal angle ϕ in the transverse plane are defined. Table 3.1 shows the summary of the commonly used variables. Especially, pseudorapidity (η) and transverse momentum (p_{T}) are often used.

3.2.2 Inner Detector

In the ATLAS experiment, huge number of tracks are generated from the interaction point at the timing of 25 ns bunch crossing. The inner detector (ID) [34, 35] located at the innermost part of the ATLAS detector is equipped to detect charged particles and precisely reconstruct the trajectory and momentum. The ID consists of the pixel detector including the Insertable B-Layer (IBL), the SemiConductor Tracker (SCT), and the Transition Radiation Tracker (TRT) in order from interaction point. Solenoid magnet with 2 T is installed in the outside of ID and the inner detector measures tracks of charged particles curved by magnetic field. The acceptance region is $|\eta| < 2.5$ which covers the barrel region ($|\eta| < 2.0$) and the endcap region ($|\eta| > 2.0$). In the barrel region, the IDs with concentric cylinder shape are installed around beam axis and in the endcap region, the disk shaped IDs are installed perpendicular to the beam axis. The designed p_{T} resolution is $\sigma_{p_{\mathrm{T}}}/p_{\mathrm{T}} = 0.05 \times p_{\mathrm{T}}$ (GeV) $\oplus$ 1%.

Table 3.1: The commonly used variables in the ATLAS experiment. These variables are used for particle information.

Variables	Descriptions	Definitions
$\boldsymbol{p}$	momentum	$\boldsymbol{p} = (p_x, p_y, p_z)$
p_{T}	Transverse momentum	$p_{\mathrm{T}} = \sqrt{p_x^2 + p_y^2}$
ϕ	Azimuthal angle in the transverse plane	$\phi = \tan^{-1}\frac{p_y}{p_x}$
θ	Polar angle from the z-axis	$\theta = \tan^{-1}\frac{p_{\mathrm{T}}}{p_z}$
η	Pseudorapidity	$\eta = -\ln(\tan\frac{\theta}{2})$
$\Delta\phi$	The minimum difference between 2 ϕ	$\Delta\phi_{i,j} = \min(\lvert\phi_i - \phi_j\rvert, \pi - \lvert\phi_i - \phi_j\rvert)$
$\Delta\eta$	The minimum difference between 2 η	$\Delta\eta_{i,j} = \min(\lvert\eta_i - \eta_j\rvert)$
ΔR	The distance in $\eta - \phi$ space	$\Delta R_{ij} = \sqrt{\Delta\phi_{ij}^2 + \Delta\eta_{ij}^2}$

Pixel Detector

Pixel detector described in Figure 3.4 consists of semiconducting silicon sensors and is installed closest to the beam pipe. In order to improve tracking robustness, luminosity effects, tracking precision and because of beam pipe replacement, and large radiation dose, IBL [36, 37] was installed in the innermost layer side from 2013 to 2014. There are 4 layers in the barrel and 5 layers of disk type in the endcap. The minimum pixel size is 50×400 μm^2, and in case of IBL, it is 50×250 μm^2. The hit pixel information is sent to readout electronics at the time when the charged particles pass through silicon sensors. The total number of channels in whole pixel detector is about 80×10^6, and the tracks are reconstructed by pattern matching method. The coverage region is $|\eta| < 2.5$. Figure 3.5 shows the relation between impact parameter (described in Section 5.1) resolution and transverse momentum. The impact parameter resolution is up about $\sim$100 μm for high momentum region.

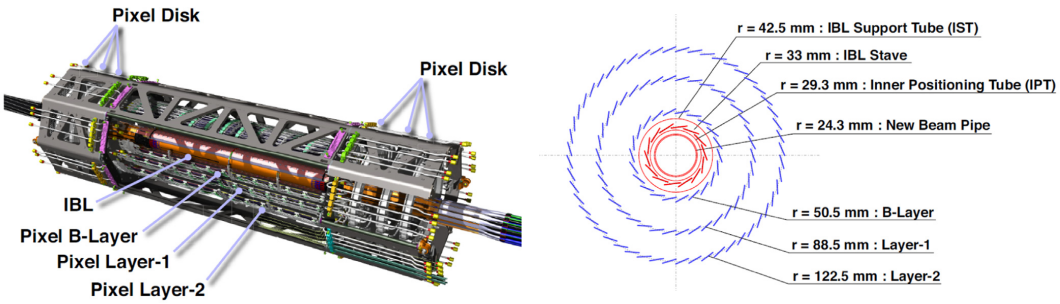

Figure 3.4: Schematic view of ATLAS 4-layer pixel detector for Run-2 [34].

Semiconductor Tracker

SCT is microstrip detector with p-on-n silicon and is constructed with 4 layers. This detector contains 61 m^2 of silicon detectors, with 6.2 million readout channels. Each silicon detector is 6.36×6.40 cm^2 size and it has 768 readout strips with 80 μm pitch. Each module consists of four single sided silicon sensors. Two sensors on each side of the module are glued together in back-to-back with 40 mrad angle difference. The coverage is $|\eta| < 2.5$ region and the resolutions of $R - \phi$ direction and Z direction are 16 μm and 580 μm. Therefore, SCT

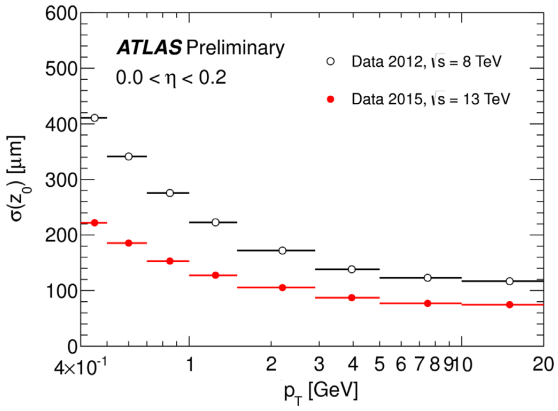

Figure 3.5: Z impact parameter resolution as a function of transverse momentum [34].

can reconstruct tracks 200 micron apart.

Transition Radiation Tracker

The purpose of TRT detector is to reconstruct tracks and identify the electron. The detector is constructed by straw tubes for fast electrons identification even in high event rates environment. In the barrel region, about 50000 straws are installed along z-axis and they are separated at the center. About 320000 straws are installed along radial direction in the endcap region. Thus, the total number of readout channels is about 400000, and typically 36 hits for one track are output in $|\eta| < 2.0$ region. To obtain good fast response, each straw has 4 mm diameter and it is constructed by a gold-plated W-Re wire (30 μm diameter) and mixed gas (Xe: 70%, CO_2: 20%, CF_4: 10%). Electrons are identified with transition photons generated from Xe gas. To combine multiple straw hits for one track, the position precision is required to be better than 50 μm in the LHC environment.

3.2.3 Calorimeter

The ATLAS calorimeter, described in Figure 3.6 [31], consists of the electromagnetic calorimeter and hadronic calorimeter. These calorimeters are located at outside of the solenoid magnet. In total, $|\eta| < 4.9$ is covered.

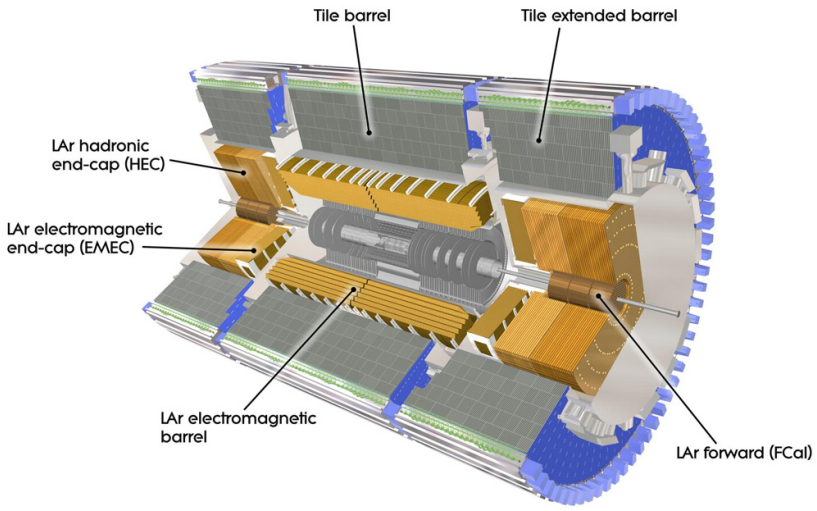

Figure 3.6: Schematic view of the ATLAS calorimeters [31].

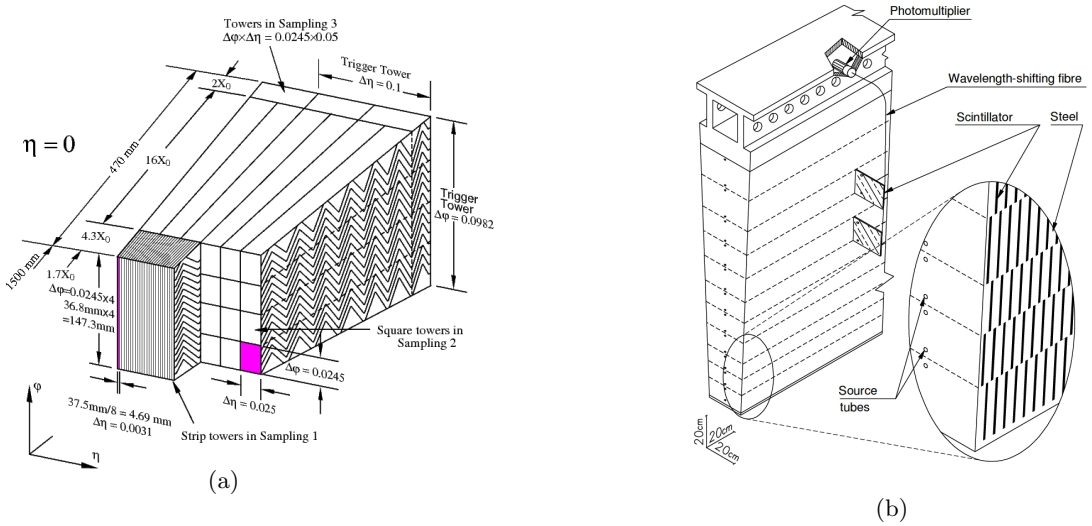

Figure 3.7: Structures of (a) the LAr electromagnetic calorimeter and (b) the hadronic calorimeter [31].

Electromagnetic Calorimeter

Electromagnetic calorimeter shown in Figure 3.7(a) is the lead/liquid argon (LAr) detector with accordion-shaped kapton electrodes and lead absorber plates. The calorimeter adopts accordion geometry, in order to obtain fast readout of signals and reduce dead space. The coverage region is $|\eta| < 1.475$ for barrel region and $1.375 < |\eta| < 3.2$ for endcap region. The pre-sampler detector ($|\eta| < 1.8$) is installed in inner size of calorimeters due to discrimination of the size of electromagnetic showers. Therefore, this geometry provides complete ϕ symmetry and there is no azimuthal cracks. The total number of readout channels is about 174000 channels.

The radiation lengths (X_0) are $> 22\ X_0$ in the barrel region and $> 24\ X_0$ in endcap region. The radiation length between the beam pipe and the pre-sampler is about 1.7 X_0. The strip section has about 4.3 X_0 and divides about 4 mm pitch position information in the η direction. It measures precise positions and identifies particles such as γ, ϕ^0, e, ϕ with high η resolution ($|\Delta\eta| \sim 0.0031$). The square section has $\Delta\eta \times \Delta\phi = 0.025 \times 0.025$ granularity and the radiation length of about 16 X_0. Back section has 0.05 η granularity and the radiation length of around $2X_0 \sim 12X_0$. The energy resolution satisfies $\sigma_E/E = 10/\sqrt{E(\mathrm{GeV})} \oplus 0.7\%$.

Hadronic Calorimeter

Hadronic calorimeter consists of the tile calorimeter in the barrel region ($|\eta| < 1.7$) described in Figure 3.7(b) and the LAr calorimeter in the endcap region ($1.5 < |\eta| < 3.2$). The tile calorimeter is sampling calorimeter with steal as the absorber and scintillator as the active material. The granularity in $\Delta\eta \times \Delta\phi$ is typically 0.1×0.1. The LAr calorimeter consists of LAr and tungsten/copper plates. There are two segments in each side with a typical granularity of $\Delta\eta \times \Delta\phi = 0.1 \times 0.1$ ($1.5 < |\eta| < 2.5$) and $\delta\eta \times \delta\phi = 0.2 \times 0.2$ ($2.5 < |\eta| < 3.2$). Extremely forward region ($3.1 < |\eta| < 4.9$) is covered by the special LAr calorimeter which adopts narrow tungsten tube to accommodate with high ionization rate. In order to reducing the punch-through into the muon system, the total interaction length in whole region is about 10. The energy resolutions satisfy $\sigma_E/E = 50/\sqrt{E(\mathrm{GeV})} \oplus 3\%$ in ($|\eta| < 3.2$) and $\sigma_E/E = 100/\sqrt{E(\mathrm{GeV})} \oplus 10\%$ in ($3.2 < |\eta| < 4.9$).

3.2.4 Muon Spectrometers

Muon Spectrometers (MSs) [31, 38–40] are installed at the outermost layer of ATLAS detector described in Figure 3.8 [31]. The aim is to trigger and to take the precision tracks of muons curved by the toroid magnetic field at fast. This is constructed by 4 muon detectors and is designed against the corresponding radiation backgrounds such as neutrons/photons from secondary interaction in the calorimeter, shield material and beam pipe. Thin Gap Chamber (TGC) and Resistive Plate Chamber (RPC) are used for level 1 trigger decision and Monitored Drift Tube (MDT) and Cathode Strip Chamber (CSC) are used for precision tracking.

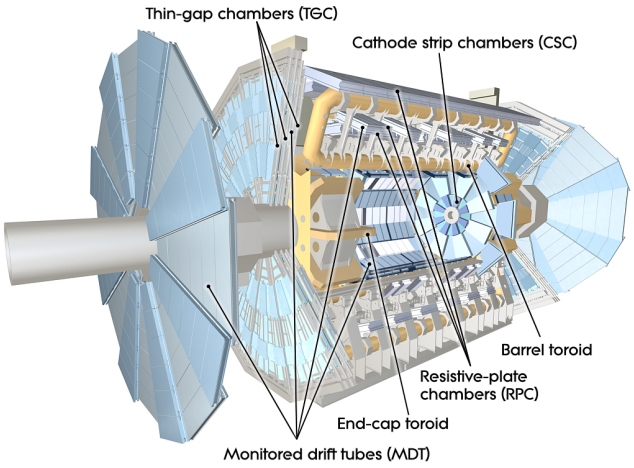

Figure 3.8: Schematic view of the ATLAS muon spectrometers [31].

Thin Gap Chamber

TGC is the multi-wired proportional chamber. The chamber can acquire the 2 dimensional hit position information (η, ϕ) from anode wire and cathode strip. In order to realize fast single muon trigger for 25 ns bunch space, this thickness design is adopted to reduce the maximum drift time. Tungsten wires with 50 μm diameter and gold plating are stretched with the pitch of 1.8 mm. The readout strips of copper plate with 30 μm thickness are laid vertically for wires. In addition, the gas mixture of 55% CO_2 and 45% $n-pentane$ circulates in the chamber for ionization and prevention of discharge. The detection efficiency of muons for a chamber is 99%. TGC is constructed by 3 stations described in Figure 3.9(a) and 3.9(b) in the end-cap region ($|\eta| > 1.05$) and total number of layers is 7 for wire and 6 for strip. The trigger efficiency for track of muon with $p_{\mathrm{T}} > 20$ GeV is about 90% efficiency.

Resistive Plate Chambers

RPC described in Figures 3.10(b) [41] is one of the gas detector with space-time resolution of typically 1 cm $\times$ 1 ns. The gas mixture of $C_2H_2F_4$ circulates in the 2 mm narrow gap sandwiched by 2 resistive plates called bakelite with 2 mm thickness, and this chamber provides the 2 dimensional position information (η, ϕ) from the readout strips put on the each plate. The 3 layers of RPC is installed in barrel region ($|\eta| < 1.05$) with symmetry for ϕ direction. Thus, the muon track is triggered and reconstructed with 3 layer coincidence.

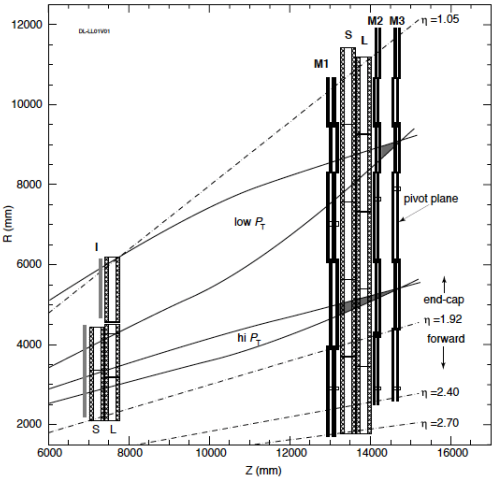

(a)

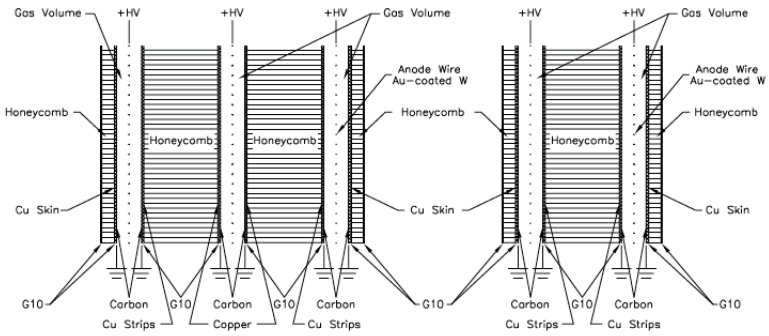

(b) M1 (left) and M2, M3 (right).

Figure 3.9: (a) Layout of three TGC stations, indicated by M1, M2, and M3 [40] and (b) the cross-sectional drawing of the TGC [31].

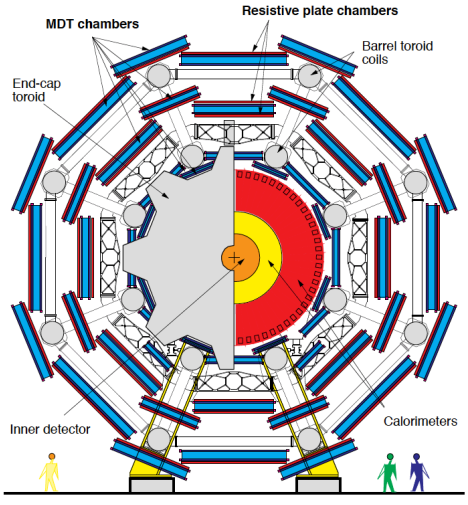

(a)

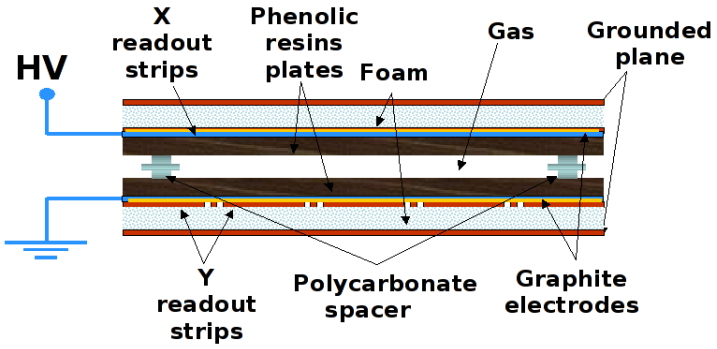

(b)

Figure 3.10: (a) Layout of three RPC layers [41] and (b) the cross-sectional drawing of the RPC [42].

Monitored Drift Tubes

MDT described in Figure 3.11(a) [39] is constructed by the aluminum tube gas detectors with 30 mm diameters and 400 μm thickness wall. The wire with 50 μm is strained into the tube and the gas mixture of $ArCH_4N_2$ is circulates in tubes. MDT has the good space-time resolution for 700 ns maximum drift time, small Lorentz angle and small gas amplification. The single-wire resolution is typically 80 μm (Figure 3.11(b)). To reconstruct the muon track precisely, 2×4 of tube layers are installed in inner station, and 2×3 of tube layers are installed in middle and outer station. To detect the strain of structure, the precise positions of MDT are monitored by laser displacement sensors and therefore MDT provides precision track reconstruction by the alignment.

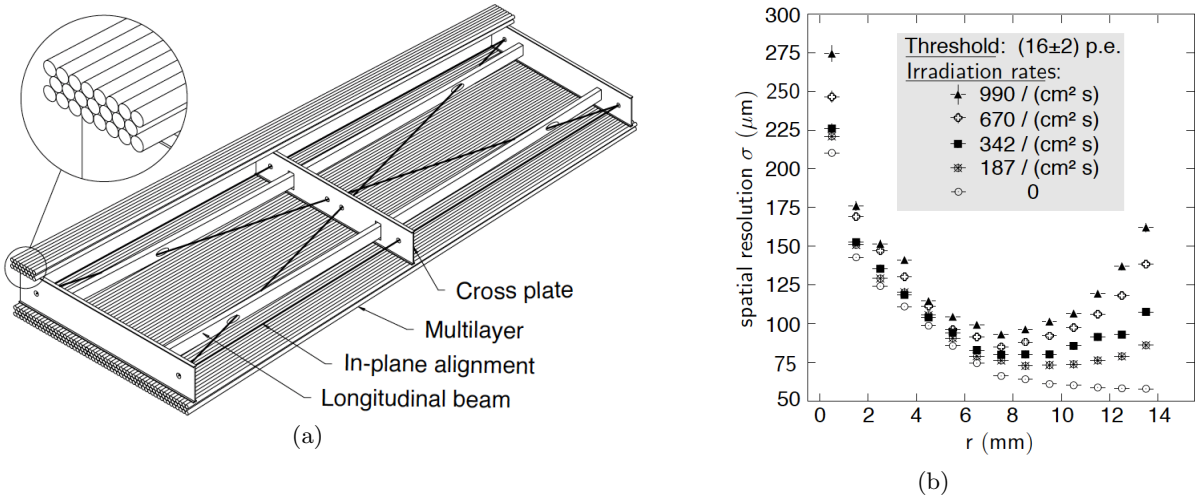

Figure 3.11: (a) Cross-sectional drawing of the MDT [39] and (b) the single-wire position resolution as a function of drift length [31].

Cathode Strip Chambers

Since a lot of quantum chromodynamics (QCD) jets or neutrons are generated by the pp collisions or the collisions between high energy particles and structure, the MDT hit rate in forward region ($|\eta| > 2.0$) may exceed the the tolerance rate of about 150 Hz/cm^2. Therefore, in this region, CSC with about 1000 Hz/cm^2 tolerance rate is installed instead of MDT. CSC is one of the multi-wired proportional chambers same as TGC, and it readouts the signals of η direction from cathode strips (Figure 3.12). CSCs are arranged in 2×4 layers and the gas mixture of $ArCO_2CF_4$ circulates in these chambers. The position resolution is better than 60 μm and CSCs have high performances about 7 ns time resolution and short drift time of ¡ 30 ns.

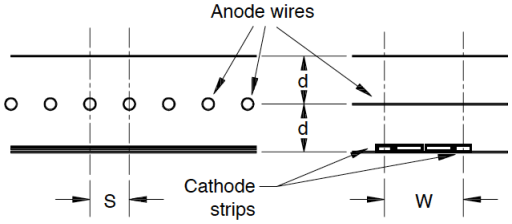

Figure 3.12: Cross-sectional drawing of the CSC. The size of s, W and d is 2.5 mm, 5.3 mm and 2.5 mm, respectively [39].

3.2.5 Superconducting Magnets

The ATLAS detector basically measures the momentum of charged particles curved by the effect of magnetic field. Super conducting solenoid and toroidal magnets are installed in the ATLAS detector described in Figure 3.13. The central solenoid provides the 2 $\sim$ 2.6 T magnetic field along the beam pipe for inner detector. The charged particles from a interaction point are curved to ϕ direction by effect of solenoid magnetic field. In order to reduce the energy deposit of electron or jets in the solenoid, the solenoid is constructed with minimum amount of material. The total X_0 of the coil and structure is about 0.66. The barrel/end-cap toroid magnet installed in outer of calorimeters provides about 4 T magnetic field along the ϕ direction. The charged particles such as muons are curved to η direction by the effect of toroidal magnetic field. The toroid magnet is designed in unique shape with 8 symmetric for phi direction and has "air-core" to reduce the amount of material for reconstruction of muon track with only muon spectrometers. Therefore, the strength of magnetic field is ununiform and depends on η and ϕ as described in Figure 3.14(a) for solenoid and 3.14(b) for toroid.

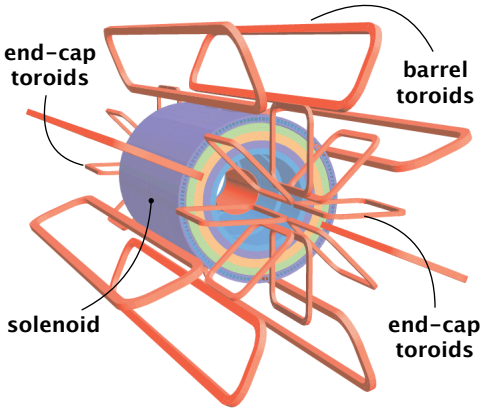

Figure 3.13: Schematic view of the solenoid and toroidal magnets [31].

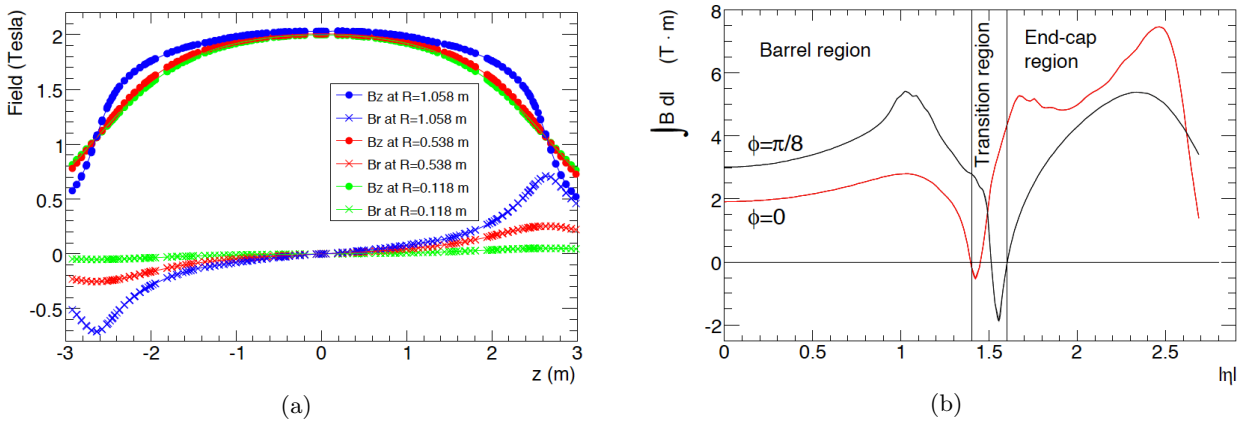

(a) (b)

Figure 3.14: Magnetic field strength supplied by (a) the solenoid magnet and (b) the toroidal magnet [31].

3.2.6 Trigger System

In order to collect the interested physics events (i.e. SUSY signal events) with high efficiency into the data storage, the ATLAS detector introduces two levels of triggers to select the interested physics events with eliminating background events. Figure 3.15 shows the trigger/data acquisition (DAQ) system in Run-2 [43]. When the data come from inner detectors, calorimeters and muon spectrometers, hardware-based level one (L1) trigger decision run parallel to stacking data in memories temporary. After L1 trigger is accepted, software-based high level trigger (HLT) run to reconstruct events rather precisely and execute decision based on the event type. Since the collision rate of proton called pile-up drastically increases corresponding to the LHC upgrade for the increases of the center of mass energy up to 13 TeV and of the instantaneous luminosity up to 10^{-34} cm^{-2}s^{-1}, the DAQ system also was upgraded.

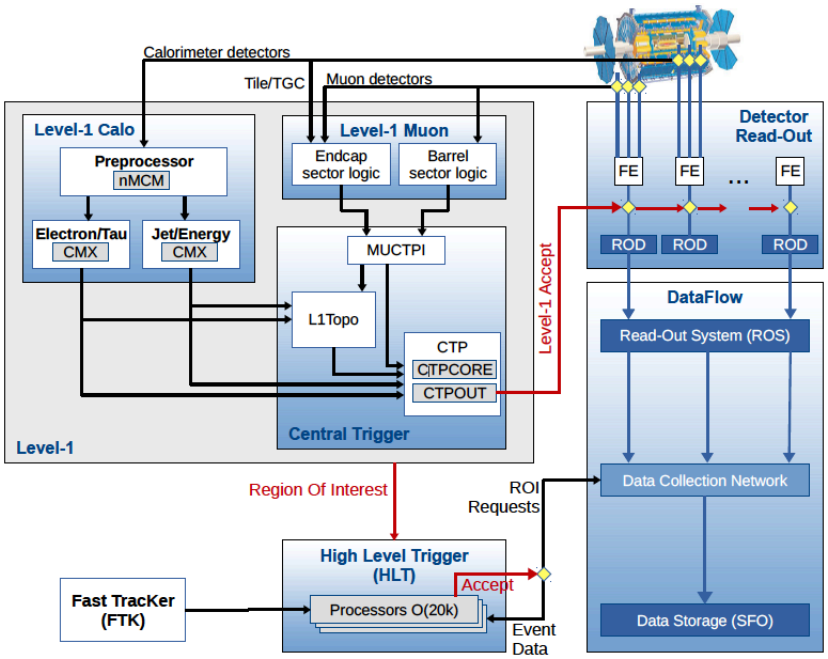

Figure 3.15: Illustration of the ATLAS trigger/data acquisition flow [43].

L1 Triggers

The L1 trigger provides information of the Regions of Interests (RoIs) in η and ϕ positions of the interested particle. The central trigger processor (CTP) decides the final L1 accepts by the integrated information of L1 trigger from each detector and it sends the L1 decision to each detector to flow the temporary stored data. The L1 trigger provides the L1 accepts to HLT with 100 kHz rate within 2.5 μs decision time. Figure 3.16 [44] shows total L1 rate as a function of time throughout a fill taken in October 2016 with a peak luminosity of $\mathcal{L}_{\text{ins.}} = 1.31 \times 10^{34}$ cm^{-2}s^{-1} and a peak pile-up of $\mu = 42$. The maximum L1 rate is up to 97 kHz by adding additional L1 total energy triggers. Subsequently the additional L1 rate is removed and the rate follows an exponential decay with decreasing luminosity during an LHC fill.

High Level Trigger

HLT constructed by CPUs and software selects the events with multiple pieces of information such as tracks, momentums of particles, etc. with full granularity information of detectors corresponding the L1 RoI region. It

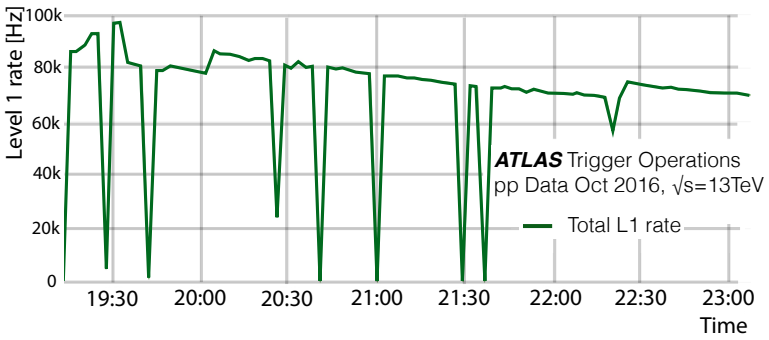

Figure 3.16: Total L1 rate as a function of time throughout a fill taken in October 2016 with a peak luminosity of $\mathcal{L}_{\text{ins.}} = 1.31 \times 10^{34}$ cm^{-2}s^{-1} and a peak pile-up of $\mu = 42$ [44].

makes the final trigger decision and reduces the 100 kHz L1 trigger rate to 1 kHz within about 200 ms processing time, and then it sends the passed events to the data storage servers.

3.2.7 Data Quality in Run-2

Data quality (DQ) system is prepared for taking the data in good quality. This system feedbacks the offline information to DAQ run as soon as possible to keep data in quality data. To process it with high speed, about 2% of data are stored in calibration stream where DQ runs. The data are analyzed at offline with high priority when DAQ run is finished, and then the histograms of detection efficiency, trigger quality, etc. are generated. The experts of each detector and data quality group check the histograms and the high quality data called "Good Run List (GRL)" able to use in the physics analysis are provided.

3.3 Data for this study

The data taking with $\sqrt{s} = 13$ TeV starts successfully from 2015. Finally, the integrated luminosity included in GRL of 2015 is 3.21 fb^{-1}and the integrated luminosity of 2016 is 32.9 fb^{-1}. The associated uncertainty for application of beam, detector and data quality is 3.2%. This analysis uses in total 36.1 fb^{-1}integrated luminosity in GRL.

Chapter 4

Phenomenology of Proton-Proton Collisions and Monte Carlo Simulation

SUSY particles can be generated from pair production or annihilation. Thus, the high energy pp collisions in the LHC have the potential to directly generate SUSY pairs. Since a proton consists of quarks and gluons bound by the strong interaction, the understanding of QCD calculations is essential in making precise predictions. This chapter discusses the basic features of *pp* collisions. The simulation does not fully reproduce the theoretical predictions of quantum electrodynamics (QED) and QCD, but rather includes numerical calculations and parametrizations of analytical results. More details are included in Reference [45, 46]. Finally, I presents an overview of the MC samples which are used in this analysis.

4.1 Production at the LHC

The cross-section (σ_{tot}) of *pp* collisions for a scattering processes $ab \to n$ (a, b : initial state partons, n : final state particle n) at the LHC experiment can be written by using the factorization approach [47]:

$$\sigma_{\text{tot}} = \sum_{a,b} \int_0^1 dx_a dx_b \int f_a^{h_1}(x_a, \mu_F) f_b^{h_2}(x_b, \mu_F) \frac{d\hat{\sigma}_{ab\to n}(\mu_F, \mu_R)}{d\boldsymbol{y}}, \tag{4.1}$$

where $x_{a,b}$ are parton fractions, $f_{a,b}^{h_{1,2}}$ are the parton distribution functionss (PDFs) where $h_{1,2}$ are parent hadrons such as protons, μ_F is the factorization scale, μ_R is the renormalization scale and the $d\hat{\sigma}_{ab\to n}/d\boldsymbol{y}$ is the parton-level cross section. The parton-level cross-section depends on the momenta ($\boldsymbol{y}$) given by the final state phase space Φ_n on the μ_F and the μ_R, and the fully differential parton-level cross-section is defined as

$$\frac{d\hat{\sigma}_{ab\to n}}{d\boldsymbol{y}} = \frac{d\Phi_n}{d\boldsymbol{y}} \frac{1}{2\hat{s}_{ab}} |M_{ab\to n}|^2, \tag{4.2}$$

where $M_{ab\to n}$ is the matrix element (ME) and $1/\hat{s}_{ab}$ is the parton flux equaled to $1/(2x_a x_b s)$ where s is the hadronic center-of-mass energy squared. The cross-section of two partons is related with only the initial state and the final state, and the ME can have all decay processes. Figure 4.1 shows the schematic view of the production of *pp* collisions and these processes are described below.

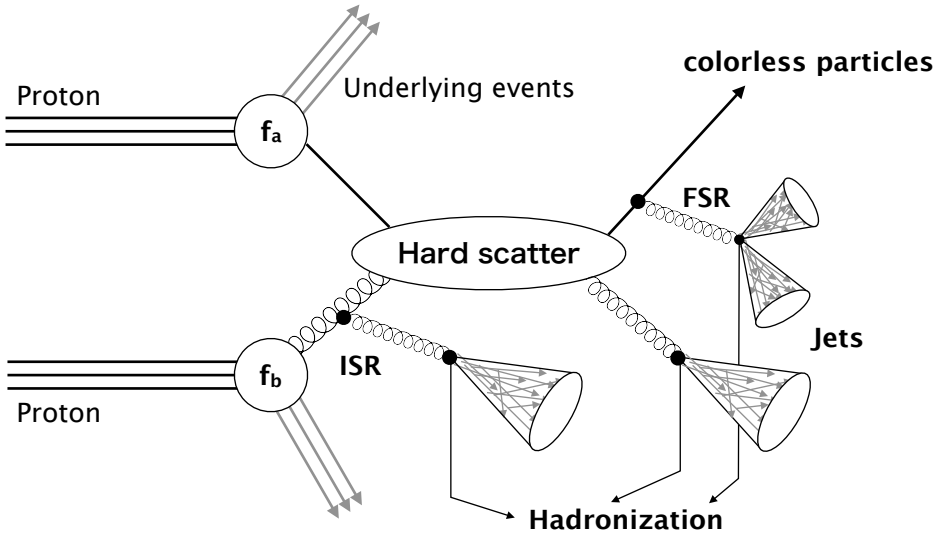

Figure 4.1: Schematic view of the production of pp collisions.

Parton Distribution Function (PDF)

The PDF's describe the probability to find the parton a (b) carrying the fraction x_a (x_b) of the momentum of the parent hadron h_1 (h_2) at the momentum transfer Q^2. The hard process from pp collisions cannot be calculated directly due to the dominant low-energy QCD effect in the parton structure, thus the factorization theorem is utilized. This theorem separates the calculation between the calculable short-distance process and the universal long-distance part, which can be derived from a fit to data. The factorization scale μ_F is used to separate the low-energy and high-energy effects and the evolutions of PDF's are described by the Dokshitzer-Gribov-Lipatov-Altarelli-Parisi (DGLAP) evolution equations [48–50]. In addition, the PDF including only non-perturbative QCD can also be estimated phenomenologically from the previous QCD measurement to match the pertubative QCD predictions. The combination and global fitting of several QCD measurements: deep inelastic scattering (DIS) and hadron-hadron collision (HERA, Tevatron) are applied, and thus the LHC experiment is mainly used these results: PDF4LHC [51], NNPDF [52], CT14 [53], MSTW [54].

Hadronization

This process is consequence of the so called "confinement" effect of strong interaction in QCD theory. In other words, for a free parton, the confinement potential ($V(r) = kr,$ where $k \sim 0.2$ GeV^2) increases distance, and finally diverges. The aggregate of fragmented hadrons produces partons in singlet color state. The hadronization describes these processes using the fragmentation function $D(z)$ (where z is the momentum fraction of the seed hadron) with the PDF. The most common model of the hadronization is the Lund-String-Model [55].

Additional Parton Radiations (ISR/FSR)

In the QCD processes considered, it is possible to add the additional gluons (which then hadronize to jets) to the initial state or the final state particles. These additional processes are defined initial state radiation (ISR) and the final state radiation (FSR).

Underlying Events

Besides the hard process of two collinding partons, many other hadronic processes take place in a collision event. These processes are called the underlying event (UE). The UE includes two categories of processes: the

beam remnants and the multiple parton soft QCD interaction (pile-up events). The protons involved in the hard scattering process are instantaneously converted into fragmented hadrons, which subsequently hadronise to final state particles. In addition, multiple parton interactions (e.g. $2 \to 2$) can also occur. The impact of the UE cannot be ignored for the performance of energy or momentum measurements, and thus several models of the MC, whose parameters can be tuned by using experimental results, are usually employed in the estimation.

Pile-up event (μ), first described in Section 3, are generated by the multiple pp interactions per the bunch crossing. It is correlated with the instantaneous luminosity of LHC. The average of μ increases up to ~ 40 at the Run-2, and this effect cannot be ignored. Thus, the hard process interactions are modeled and to these the pile-up particles are overlaid, by using pp collision events.

4.1.1 Parton Shower Simulation

The QCD matrix elements cannot be computed exactly, thus the ME is usually calculated by using the parton shower (PS) approximation. The QCD showering is well known from first principles, however the problem is that the divergence of soft or collinear emission produced by QCD shower cannot be ignored. These emissions provide the dominant contribution to the extra partons from the partons involved in the hard scattering. The PS approach can calculate the perturbation to all orders, in which the cross-section of an additional soft parton ($d\sigma_{n+1}$) is factorized from the original cross-section ($d\sigma_n$) and the probability of parton splitting $P_{i\to jk}$. The cross-section can be written as

$$d\sigma_{n+1} = \sigma_n \sum_{i\to jk} \frac{\alpha_S}{2\pi} \frac{d\theta^2}{\theta^2} dz P_{i\to jk}(z,\phi) d\phi, \tag{4.3}$$

where notations of i, j, k indicates the parent parton (i) and the children partons (j, k), z is the fraction of energy carried by parton k from its parent parton i, θ is an opening angle between the parton k and i, ϕ is an azimuthal angle of a parton j around an axis defined by i. The probabilities $P_{i\to jk}$ can be calculated by using the DGLAP evolusion equations, and thus the $P_{i\to jk}$ for all pattern of quarks and gluon emission can be obtained as

$$P_{q\to q\bar{q}} = \frac{z^2 + (1-z)^2}{2}, \tag{4.4}$$

$$P_{q\to qg} = \frac{4}{3}\frac{1+z^2}{1-z}, \tag{4.5}$$

$$P_{q\to gq} = \frac{4}{3}\frac{1+1(1-z)^2}{z}, \tag{4.6}$$

$$P_{q\to gg} = 3\frac{z^4+1+1+(1-z)^4}{z(1-z)} \tag{4.7}$$

The PS approximation has a significant issue that consists in a phase space overlap (double-counting) between jets. It should be corrected by the "matching" and "merging" procedures and the famous algorithms are the Catani-Krauss-Kuhn-Webber (CKKW) [56, 57] algorithm and the Michelangelo-L Mangano (MLM) algorithm [58].

4.2 Signal and SM Background Productions in the LHC

4.2.1 Stop Pair Production

Figure 4.2 shows the stop pair production at the LHC. The stop can be only pair-produced at the LHC. One W boson decays into one lepton and neutrino and other W boson decays hadronically as two jets. Thus, the

final state particles are one lepton, jets, and missing transverse momentum that account for a neutrino and two neutralinos.

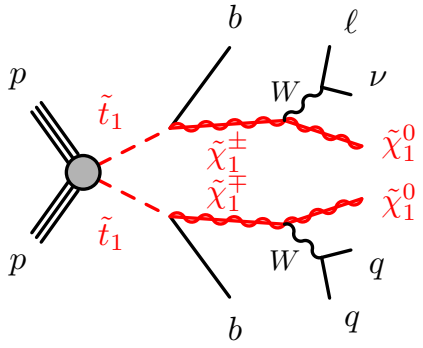

Figure 4.2: Feynman diagram of stop pair production at *pp* collisions.

4.2.2 SM Background Productions

The SM backgrounds, which are abundantly produced at the LHC, are $t\bar{t}$, W+jets, $t\bar{t}+W/Z$, single top, Z+jets, dibosons ($WW/WZ/ZZ$, etc). Figures 4.3 show these background productions. In all these physics processes there can be leptons, jets, and missing transverse energy, thus these background categories have a non negligible probability of passing the analysis selection.

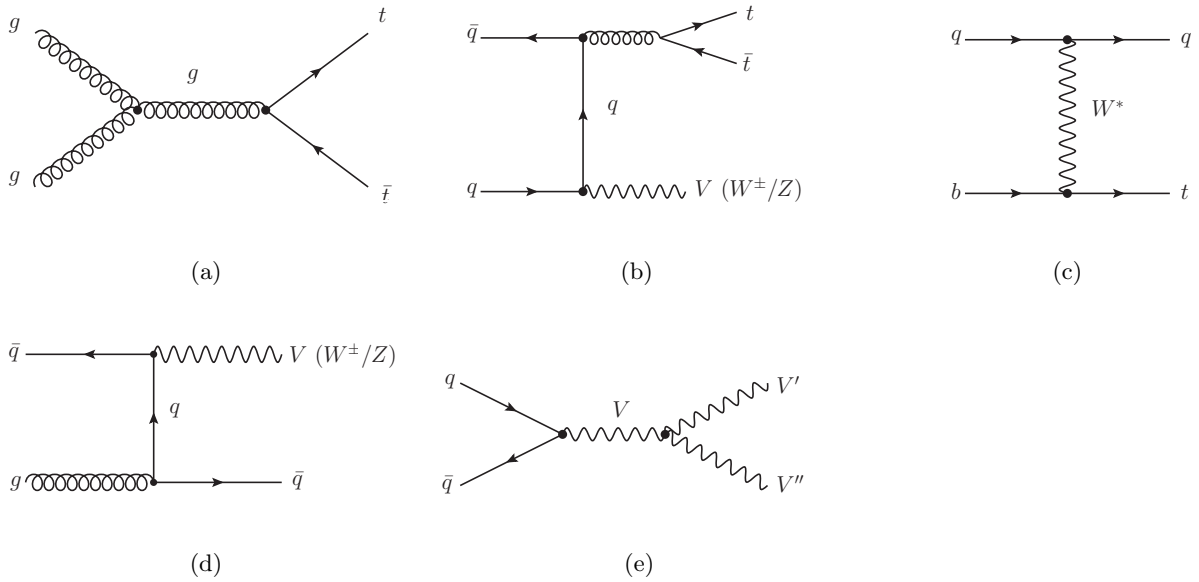

Figure 4.3: Feynman diagrams of SM background productions at *pp* collisions. Backgrounds, which are abundantly produced, are (a) $t\bar{t}$, (b) $t\bar{t}+W/Z$, (c) single top, (d) V+jets, (e) dibosons, where V means a vector boson (W, Z).

4.3 Simulated Samples

This section lists all the MC simulations for background processes and signal processes.

Table 4.1 shows details of the simulation samples including the ME generator, PDF set, the PS and hadronization model, the UE tune, and order of the cross-section calculation.

Table 4.1: Overview of the simulated samples.

Process	ME generator	PDF set	PS and hadronization	UE tune	Cross-section calculation
$t\bar{t}$	POWHEG-BOX v2 [59]	CT10 [60]	PYTHIA 6 [61]	P2012 [62]	NNLO + NNLL [63–68]
Single-top	POWHEG-BOX v2	CT10	PYTHIA 6	P2012	NNLO + NNLL [69–71]
V+jets (V = W/Z)	SHERPA 2.2.0 [72]	NNPDF3.0 [52]	SHERPA	Default	NNLO [73]
Diboson	SHERPA 2.2.1	CT10	SHERPA	Default	NLO
$t\bar{t}$+V	MG5_aMC@NLO 2.2.2 [74]	NNPDF3.0	PYTHIA 8 [75]	A14 [76]	NLO [74]
SUSY signal	MG5_aMC@NLO 2.2 - 2.4	NNPDF2.3 [77]	PYTHIA 8	A14	NLO+NLL [78]

The ME generators include POWHEG [59] [79–82], SHERPA [72] and MADGRAPH [74], in addition the modeling of b-hadron decay is simulated by using EVTGEN v1.2.0 [83] for all samples.

Tune of the Underlying Events including Pile-up

The UEs including the pile-up (minimum-bias interactions) to be overlaid to the hard-scattering event are produced in all samples to simulated the effect of multiple *pp* collisions in the same or nearby bunch crossing. The number of minimum-bias interactions is tuned using the multiparton interaction (MPI) parameters of PYTHIA 6(8) that are generated from "P2012" and "A14" tune series. These tune series are generated by the several PDFs: CTEQ6L1 [84], MSTW2008LO [54], NNPDF23LO [85], and HERAPDF15LO [86].

Detector Simulation

All background samples are processed with the full simulation based on the GEANT 4 [87], and the signal samples are processed with the ATLAS fast simulation [88] that are based on the parametrization of the electromagnetic calorimeters and hadron calorimeters simulated by the GEANT 4.

4.3.1 Background Samples

The $t\bar{t}$ and single-top are calculated to the Next-to-Next-to-Leading Order (NNLO) with the resummation of the soft gluon emission in the Next-to-Next-to-Leading Logarithmic (NNLL) accuracy. These MEs are generated by using POWHEG and it is interfaced to PYTHIA 6 for calculation of the PS and hadronization.

MADGRAPH and SHERPA are mostly used for the process which have many jets including the ISR and FSR because these MC simulations can precisely calculate better than other glsplMC. The W/Z+jets and diboson samples are prcessed with SHEPRA 2.2.0 and 2.2.1. These ME generators use Comix [89] and OpenLoop [90] ME calculations. For calculations of the PS and hadronization, the default PS calculator of SHERPA [91] with ME+PS@NLO prescription [92] is used. The NNPDF3.0 PDF set is used in conjunction. The W/Z+jets are only normalised to NNLO cross-section.

The ME of $t\bar{t}$+V are calculated by using the MADGRAPH and PYTHIA 8 interfaced to MADGRAPH is used for PS and hadronization.

4.3.2 Signal Samples

The ME generator for signal processes is MADGRAPH and the ME is calculated to Leading Order (LO). The generator includes up to two extra partons, and is interfaced to PYTHIA 8 for the PS and hadronization. Signal cross-sections for stop pair production are calculated to NLO in the strong coupling constant, adding the resummation of soft gluon emission at NLL accuracy (NLO+NLL). Figure 4.4 shows the relation between the stop mass ($m_{\tilde{t}_1}$) and cross-section ($\sigma_{\tilde{t}_1}$). The band corresponds the cross-section uncertainties calculated by the cross-section predictions using different PDF sets. For the higgsino LSP scenario, the assumed mass difference between chargino and neutralino is set to 5 GeV. For the wino NLSP scenario, the assumed mass difference between stop and chargino is set to 10 GeV. Both scenarios can use the simplified models of MC, where BR($\tilde{t}_1 \to b\tilde{\chi}_1^{\pm}$) is set to 100% because the searched regions are constrained by the masses of stop, chargino and neutralino and the other decay channels (e.g. $\tilde{t}_1 \to t\tilde{\chi}_1^0$) is forbidden.

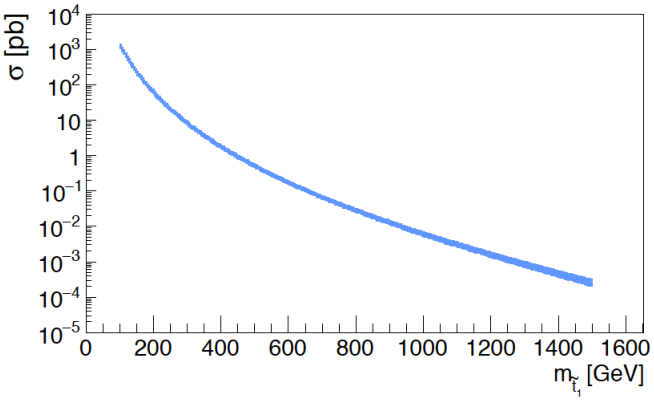

Figure 4.4: Cross-section of stop pair production as a function of stop mass at NLO and NLL accuracy. The error band corresponds to the uncertainty.

Chapter 5

Object Reconstructions and Definitions

The data passing the online trigger requirements are recorded, and the events contained in the recorded raw data are reconstructed offline using several event reconstruction procedures. All objects contained in each event are reconstructed and identified with four-momentum and track information. In this chapter, an overview of several reconstruction or identification methods and the definition of the objects that will be used in this analysis will be given.

5.1 Tracks and Primary Vertex

The tracks used for physics analysis are produced by the baseline offline track reconstruction algorithm from the ID's. Only the muon tracks are reconstructed by the combination of the ID's and MS's and it is described in Section 5.3. The baseline track reconstruction algorithm consists of 3 steps [93]. In the first step the three-dimensional hit points referred to as space-points from pixel and SCT detectors are collected. In the Pixel detector, each cluster, which is a set of connected pixels, equates to one space-point, while in the SCT detector, clusters are defined as the combination of both sides of a strip layer. To obtain the space-point that corresponds to the clusters the pixel detector, the charge in the pixel sensor is collected on multiple pixels. The intersection of a charged particle and a pixel sensor is determined by the connected component analysis (CCA) [94] and a linear approximation refined with a charge interpolation technique. Finally, the clusters are determined by the neural network (NN) technique [95]. The second step is the iterative combinational track finding. After the creation of the clusters, seeds are formed with sets of three space-points of Pixel or SCT detectors. The four different combination types of seeds can be made by satisfying the condition that some space-points come from pixel(SCT) and one space-point from SCT(pixel). One additional space-point compatible with the seed is also required to improve the purity. After that, the track candidates are reconstructed by a combinational Kalman filter [96] with seeds. Since the purity is further improved, TRT extension [97] is included to the track finding. The third step consists in the reconstruction of the tracks. A weight, called track score, is applied to track candidates (e.g. missing clusters on the track trajectory reduce the score). The χ^2 of the track fit, which is same as the ATLAS global track fit [98], is also applied to reconstruct the track momentum. Finally, tracks are determined considering these values.

A refined algorithm called "Tracking In Dense Environment (TIDE)" [93] is used. It was developed to improve the track reconstruction efficiency of the NN and to handle the multiple tracks from pile-up due to the luminosity increase. Figure 5.1 shows the average efficiency for the reconstruction of jets with different jet-flavor tagging. The latter is determined exploiting the lifetime of b-quarks measured by the track impact parameters (described in Figure 5.2), the identification, and properties of displaced vertices. More information of b-quark

reconstruction is shown in Section 5.4. Both light-flavor jets and b-jets efficiencies are improved by about 10% by the use of TIDE.

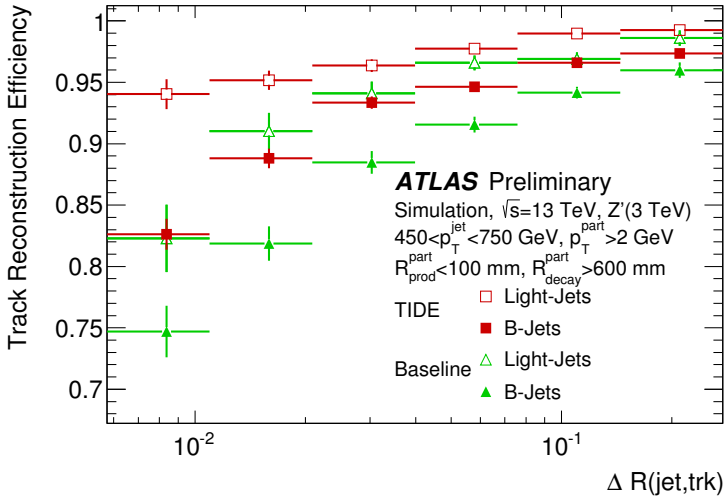

Figure 5.1: Average reconstruction efficiencies of jets with different jet-flavor tagging. The p_{T} of the selected jets ranges from 450 GeV to 750 GeV. The efficiencies increases by about 10% with respect to the Run-1 result [93].

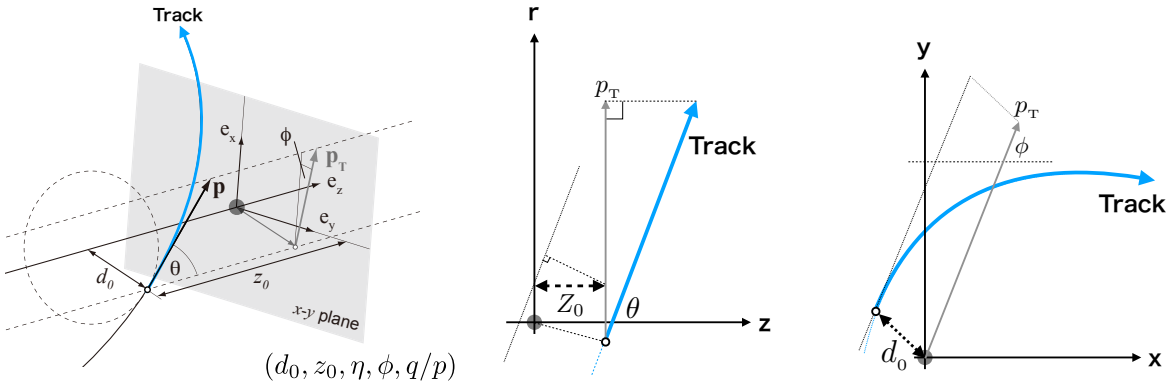

(a) (b) (c)

Figure 5.2: Definition of the impact parameters for a track. (a) is a three-dimentionsional illustration, (b) is its projection on the Z-R plane, and (c) is the projection on the X-Y plane.

The determination of the primary vertex [99] is important to reconstruct the tracks and the momentum of particles. The method for the reconstruction of vertices [100] in the ATLAS experiment consists in an iterative approach to vertex finding and fitting. It can work with good performance up to an average of pile-up events (μ) up to 40. From Run-2, μ is greater than 40, and the effect is not negligible. Thus, a new algorithm [99] that reduce the dependence on the pile-up of the vertex finding efficiency has been introduced. The new algorithm is similar to an imaging algorithm and it can identify simultaneously all vertex locations in the LHC bunch crossing by using all tracks. After the identification of vertex positions, vertices are determined with the vertex finding and fitting algorithm. When several vertices are identified, the vertex with the highest $\sum_{\mathrm{tracks}} p_{\mathrm{T}}^2$ and

with at least two tracks associated to it is defined as the primary vertex. In this analysis, to improve the purity of the hard-scattering collisions of interest, the selection of tracks with $p_{\mathrm{T}} > 400$ MeV is required.

5.2 Electrons

Electrons are among the final state particles of interest of this analysis. Electron tracks are detected by using the inner detectors and their energies are determined by using the energy deposit in the electromagnetic (EM) calorimeter. The dominant backgrounds background sources are hadrons and non-prompt electrons that originate predominantly from photon conversions and heavy flavor hadron decays. Thus, identification and isolation criteria to reduce these backgrounds and to improve the purity are also required. The reconstruction of electrons proceeds through several steps:

Seed-cluster Reconstruction
At first, the "seeds", defined as longitudinal towers with total transverse energy above 2.5 GeV are found into the sliding window with a size 3×5 in units of $0:025 \times 0:025$ that corresponds to the granularity of the EM calorimeter middle later. The next step is to form the clusters and to reconstruct their kinematics using the clustering algorithm [101] with the seeds information. The clustering efficiencies are 95% for transverse energy above 7 GeV and 99% for transverse energy above 15 GeV.

Track Reconstruction
After the seed reconstruction, the loose track reconstruction proceeds from the track seeds produced by the inner detectors. This reconstruction has two steps. The first one is the pattern recognition using the energy loss information. Two pattern recognitions corresponding to the pion hypothesis and electron hypothesis are included in the this process. The pattern recognition using pion hypothesis is the same as the standard ATLAS pattern recognition and this algorithm allows up to 30% energy loss at each intersection of the tracks to take into account for possible bremsstrahlung. If the track seeds have transverse momentum above 1 GeV, the pion pattern recognition algorithm is discarded. In this case, the electron pattern recognition algorithm, which allows large energy loss, is performed. The second step is to fit the tracks using the ATLAS global χ^2 track fitter [98], which is the same as the baseline track reconstruction.

Electron Specific Track Fit
In case the track reconstruction passed the electron hypothesis, the specific track re-fit algorithm proceeds. This algorithm requires the match between tracks having more than 4 silicon detector hits and EM clusters determined at seed-cluster reconstruction phase. After that, these tracks are reconstructed by using the Gaussian Sum Filter (GSF) [102], which takes into account the non-linear bremsstrahlung.

Electron or Photon Candidate Reconstruction
If several electron track candidates are found, the primary tracks is determined by using the cluster-track distance $\Delta R = \sqrt{\Delta\eta^2 + \Delta\phi^2}$ calculated with different momentum hypotheses and inner detector information such as the number of pixel hits. If no associated hit in the inner detectors is found, this candidate is considered as a photon candidate. To increase the reconstruction quality of electron and photon, some selections on the associated hits and tracks information are introduced and the calibrated energy described in Section 5.2.1 is also recalculated by re-forming the clusters using the multivariate techniques [103] in this step.

The combination between tracks and primary vertex is required to reduce the backgrounds originating from conversions and secondary particles. The following selection on the track parameters such as d_0, z_0, Δz_0, and

σ_{d_0} is required: $d_0/\sigma_{d_0} < 5$ and $\Delta z_0 \sin\theta < 0.5$ mm. Figure 5.3 shows the reconstruction efficiency corresponding to the E_{T} (a) and η (b) that are obtained by using the $Z \to ee$ events for both MC and data. The reconstruction efficiency for electrons associated to good quality tracks varies from 97% to 99%. The compatibility between data and MC is good.

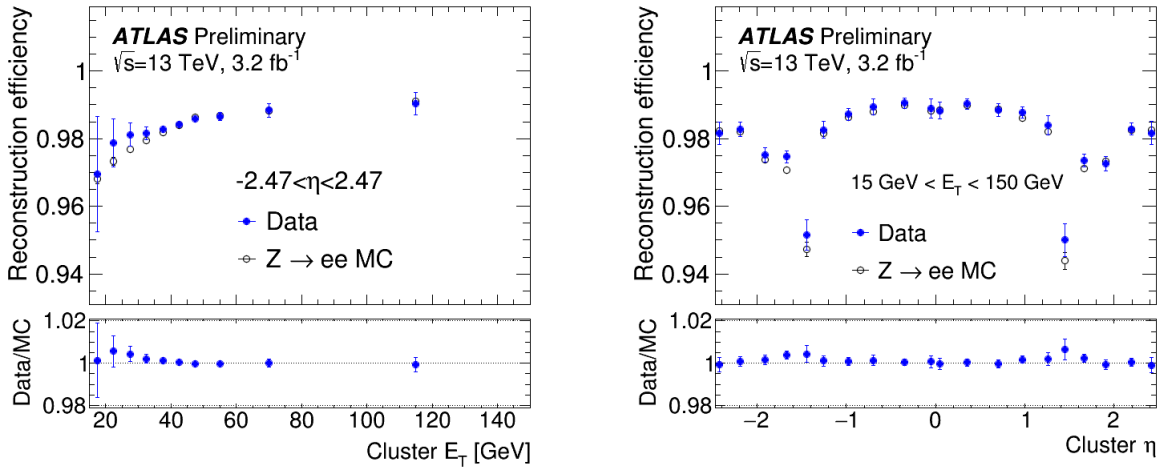

(a) (b)

Figure 5.3: Measurement of the reconstruction efficiency (a) as a function of E_{T} integrated over the full pseudorapidity range and (b) as the function of η for 15 GeV $< E_{\mathrm{T}} <$ 50 GeV [101].

The electron candidates determined from the electron reconstruction algorithm could originate from backgrounds such as hadronic jets or converted photons. To improve the purity of real electrons, the identification algorithm is applied. This algorithm uses several properties of clusters, tracks and energy (e.g. the electron cluster, the calorimeter shower shape, etc.) with two selections. The first selection is the number of IBL hits information to reduce the photon conversion and the second is the likelihood-based on the TRT high-threshold hit. The baseline identification algorithm uses the likelihood-based (LH) method which is one of the multivariate analysis (MVA) techniques. It can take into account several properties of electron candidates at the same time. The output value of the LH method is the likelihood-ratio between the likelihood signal probability and the sum of likelihood signal and background probabilities, defined as:

$$dL = \frac{\mathcal{L}_{\mathrm{S}}}{\mathcal{L}_{\mathrm{S}} + \mathcal{L}_{\mathrm{B}}}, \quad \mathcal{L}_{\mathrm{S}} = \prod^{n} P_{\mathrm{S(B)}}, \tag{5.1}$$

where $P_{\mathrm{S(B)}}$ is the probability density function.

The identification criteria are defined for three different levels of background rejection (loose, medium, tight). Each criterion is determined by using the several operation points of the relation between background rejection and electron identification efficiency. Some variables such as the shower shape depend on the $|\eta|$ and E_{T}, and thus the operation points are optimized in each region separately for $|\eta|$ and E_{T}. Figure 5.4 [104] shows the combined the reconstruction and identification efficiency as a function of E_{T} (a) and η (b) that is measured by using the $Z \to ee$ events for both MC and data. There is good agreement between data and MC, and the data/MC ratio ranges from 90% to 99%.

To further discriminate the signal originating from a hard-scattering process of interest and backgrounds (photon conversion, etc), electron isolation criterion are also introduced for electron reconstruction. This

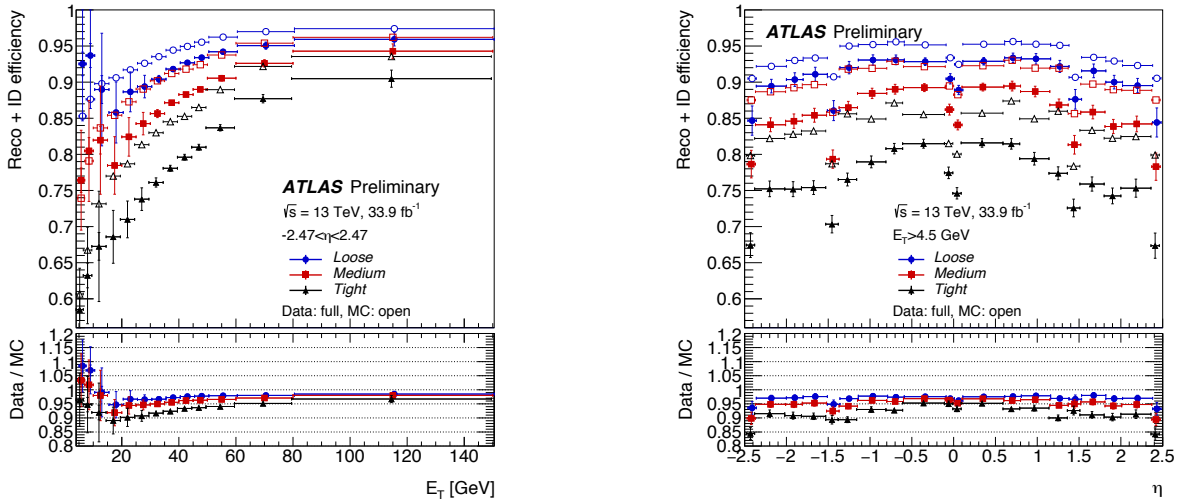

(a) (b)

Figure 5.4: Combined electron reconstruction and identification efficiencies (a) as a function of E_{T} integrated over the full pseudorapidity range and (b) as the function of η for $E_{\mathrm{T}} > 4.5$ GeV [104].

criterion uses two variables based on E_{T} and p_{T}. The one is the $E_{\mathrm{T}}^{\mathrm{cone0.2}}$ which is defined as the sum of transverse energies of the topological clusters within a cone of $\Delta R = 0.2$ around the candidate electron cluster. The other is the $p_{\mathrm{T}}^{\mathrm{varcone0.2}}$, defined as the sum of transverse momentum of all tracks within a cone of $\Delta R = \min(0.2, 10\mathrm{GeV}/E_{\mathrm{T}})$ around the candidate electron track. These tracks must pass the following requirements; $E_{\mathrm{T}} > 1$ GeV; $(n_{\mathrm{Si}} \geq 7, n_{\mathrm{Si}}^{\mathrm{hole}} \leq 2, n_{\mathrm{Pixel}}^{\mathrm{hole}} \leq 1, n_{\mathrm{Si}}^{\mathrm{mod}} \leq 1)$, where $n_{\mathrm{Si}}^{\mathrm{hole}}$ and $n_{\mathrm{Pixel}}^{\mathrm{hole}}$ are the numbers of missing hits in the pixel and SCT and $n_{\mathrm{Si}}^{\mathrm{mod}}$ is the number of hits in the silicon detector assigned to more than one track; $\Delta z_0 \sin\theta < 3$ mm.

Differences between data and MC for all reconstruction, identification and isolation methods are taken into account by a correction factor called scale factor. The scale factor is calculated by using the $Z \to ee$ and $J/\psi \to ee$ events.

5.2.1 Energy Calibration

The energy calibration is important for physics analysis and more details are given in reference [103, 105]. The baseline calibration procedure is the same as in Run-1 and the procedure for Run-2 has been tuned for higher luminosities and energies: 1) data-driven corrections optimized to mitigate the non-uniformity of detector response; 2) simulation-based calibration; 3) data-driven correction of energies scale factor for data and resolution for MC. The correction between data and MC for mis-calibration is defined as:

$$E_i^{\mathrm{data}} = E_i^{\mathrm{MC}}(1 + \alpha_i), \tag{5.2}$$

where E_i^{data} and E_i^{MC} are the electron energies in data and simulation, and α_i represents the deviation, where the index i indicates the pseudorapidity region. The electron energy calibration resolution is defined as:

$$\frac{\sigma(E)}{E} = \frac{a}{\sqrt{E}} + \frac{b}{E} + c, \tag{5.3}$$

where a and b are parameters that describe respectively the shower fluctuations and electronic noise in the calorimeter and c is a constant term. The values of most of the systematic uncertainties have been taken from Run-1 results and the relative uncertainty on the energy resolution is better than 10% with $Et < 50$ GeV.

5.2.2 Definition

Table 5.1 shows the definition of the two criteria for the electron channel in this analysis: baseline electron and signal electron. The baseline criterion applies the loose selection for electron candidates and the signal criterion applies the tight selection. To reduce the fake electron candidates and also to improve the purity of real electron, electron candidates should be signal electrons. In addition, there are two electron selections defined as "**soft**" and "**hard**", depending on the energies (momentum) for each criterion. The soft electron selection is used for the higgsino LSP search described in Section 6, because the momenta of the final state particles are usually very low. The momentum selection value of electron candidates should be greater than 5 GeV, which is the threshold for efficient detection. The identification and the isolation criteria should be tight, in order to remove the fake-electrons. On the other hand, the hard electron selection is used for the wino NLSP search described in Section 7. The final state particles of this scenario are not sensitive populate the low momentum region. The momentum selection threshold can be high and the purity is also expected to be very high. Thus, we can loosen the identification and isolation requirements.

Table 5.1: Definition of baseline and signal electron.

baseline soft(hard) electron	signal soft(hard) electron
$p_{\mathrm{T}} > 5$ GeV	$p_{\mathrm{T}} > 5(27)$ GeV
$\|\eta\| < 2.47$, included crack region ($1.37 < \|\eta\| < 1.52$)	$\|\eta\| < 2.47$, included crack region ($1.37 < \|\eta\| < 1.52$)
VeryLooseLH	TightLLH (LooseAndBLayerLH)
-	$\|z_0 \sin\theta\| < 0.5$ mm, $\|d_0/\sigma_{d_0}\| < 5$
-	FixedCutTight(LooseTrackOnly) Isolation

5.3 Muon

Muons [106] are also among the final state particles considered in this analysis. Similar to the electron object reconstruction, muons are also reconstructed following the several selections to reduce the non-prompt muons originating form hadron decays: identification, and isolation. Muon tracks are basically reconstructed by the ID and the MS independently. Finally, the muon tracks are produced by using the combination of these track candidates. The muon reconstruction in the ID's is the same as the general track reconstruction described in Section 5.1. In the case of MS's, the MS tracks are reconstructed by using the hit pattern from the MDT and trigger chambers with hough transform algorithm [107]. This algorithm finds at least two seed-segments in the middle layers of MDT and the muon tracks are reconstructed by using ATLAS global χ^2 fit with these seed-segments and other hits. After that, several combinational reconstruction techniques are used to get the muon tracks with high purity:

Combined (CB) Muon
This algorithm is the basic reconstruction algorithm for muon tracks. It generates the muon combined tracks by using the global re-fit of hits corresponding to the ID tracks and the MS tracks. To generate high purity tracks, some hits of a MS track are removed or added to increase the fit quality.
Segmented Tagged (ST) Muon
This algorithm is used to increase the acceptance of muons with low p_{T}. The ID tracks identified as muon-like objects should match at least one segment of MDT or CSC and the combined muon tracks are reconstructed.
Calorimetered Tagged (CT) Muon
To cover and to increase the acceptance of muon tracks passing through the MS dead region ($|\eta| < 0.1$), this

algorithm is used. This technique is almost the same as that of ST muon, and in addition the positions of energy deposits in the calorimeters matched to the ID tracks are used instead of MS tracks.

Extrapolated (ME) Muon

The ME muon technique is included in combined muon algorithms for the high eta range ($2.5 < |eta| < 2.7$).

Muon track candidates are searched for in this order CB > ST > CT > ME. The muon identification criteria is defined to suppress backgrounds originating from pions, kaons, etc. This criterion uses several variables to increase the purity of the muon sample. These are:

- q/p significance, defined as the absolute value of the difference between the ratio of the charge and the momentum detected by ID and MS;
- ρ', defined as the absolute value of the difference between the transverse momenta detected by ID and MS;
- normalized χ^2 of the combined track fit.

The identification criterion includes the basic selection ($n_{\text{pixel}} \geq 1; n_{\text{SCT}} \geq 5; n^{\text{hole}}_{\text{pixel or SCT}} < 3$) for robustness of the momentum measurements and it can separate three different categories (loose, medium, tight) with different values of purity and efficiency. The medium category is the ATLAS default selection and it has the lowest systematics. It uses the CB muon and ME muon and the selection is defined as:

- Total hits ≥ 3 with at least $n_{\text{MDT}} \geq 2$;
- q/p significance < 7.

The loose category uses all combined muon tracks to increase the identification efficiency. The selection requirement is the same as the medium selection. For higher purity, the tight category is defined and it requires only CB muon. The selection for the tight category is the same as the medium selection and it adds more requirements: hits must be present in two MS stations; normalized $\chi^2 < 8$; two-dimensional cut between q/p vs ρ'. Table 5.2 shows the efficiencies for prompt muons from W decays and hadrons decaying in-flight and misidentified as prompt muons computed using a $t\bar{t}$ MC. The efficiency of loose category is more than 96% for both p_{T} regions and the misidentification rate is less than 0.8%. In case of tight category, that is also good agreement; the efficiency is more than 89% and the rate is less than 0.2%.

Table 5.2: Efficiency for prompt muons from W decays and hadrons [106].

Selection	$4 < p_{\text{T}} < 20$ GeV		$20 < p_{\text{T}} < 100$ GeV	
	$\epsilon^{\text{MC}}_{\mu}$ [%]	$\epsilon^{\text{MC}}_{\text{Hadron}}$ [%]	$\epsilon^{\text{MC}}_{\mu}$ [%]	$\epsilon^{\text{MC}}_{\text{Hadron}}$ [%]
Loose	96.7	0.53	98.1	0.76
Medium	95.5	0.38	96.1	0.17
Tight	89.9	0.19	91.8	0.11

Figure 5.5 [108] shows the reconstruction efficiencies with the medium identification criteria measured by using tag-and-probe method for the $Z \to \mu\mu$ and $J/\psi \to \mu\mu$ events. The average efficiencies for medium identification are around 98% and the data are in good agreement with the MC. The efficiency for loose identification is almost the same as the efficiency for the medium identification. For tight identification, the efficiency is a few percent lower than that of the medium identification. There are some inefficient regions corresponding to the eta and phi arising from the poor alignment of MDT. For this analysis, the loose and tight categories are used.

The prompt muons produced by the decay of heavy particles such as the W boson are isolated. On the other hand, non-prompt muons originating from the decay of hadronic jets are not isolated, being specially

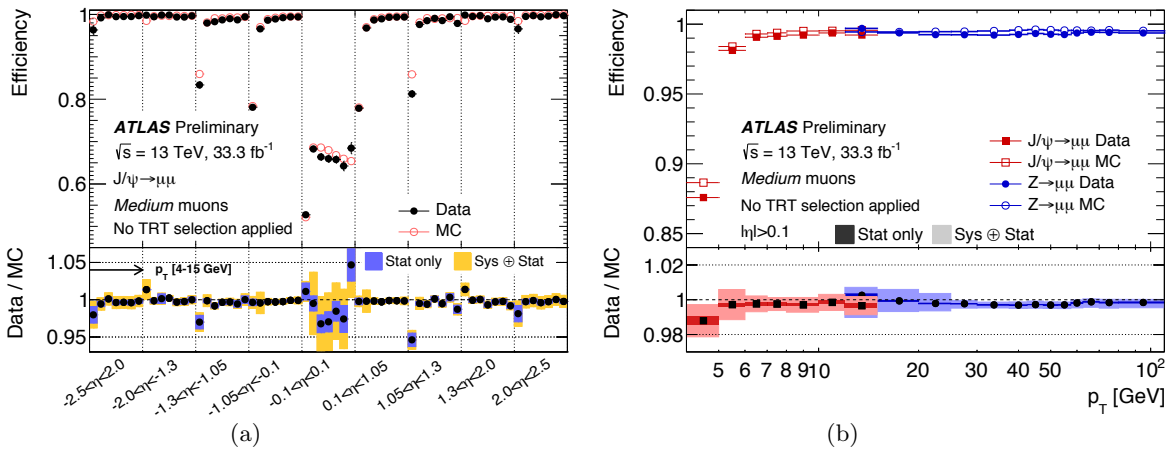

Figure 5.5: Combined electron reconstruction and identification efficiencies (a) as a function of η integrated over the full ϕ and p_{T} range with $p_{\mathrm{T}} > 10$ GeV selection and (b) as the function of p_{T} integrated over the full ϕ and η range [108].

close to other particles. Thus, the isolation criteria to reduce these backgrounds is required similarly as for the electron reconstruction. This criterion uses two isolation techniques: track based and calorimeter bases. The track based technique uses the $p_{\mathrm{T}}^{\mathrm{varcone0.3}}$ variable, which is the sum of transverse momenta for tracks of the charged particles with $p_{\mathrm{T}} > 10$ GeV into the $\Delta R < 0.3$, excluding the tracks of the muon candidate. The calorimeter based uses $E_{\mathrm{T}}^{\mathrm{topocone0.2}}$, which is the sum of the transverse energies corresponding to the energy deposits of the calorimeter tower, including also the muon candidate track. The isolation criteria is selected by using several working points and this analysis uses the "FixedCutTightTrackOnly" criterion, which requires $p_{\mathrm{T}}^{\mathrm{varcone0.3}}/p_{\mathrm{T}}^{\mu} < 0.06$ to increase the purity of prompt muons.

5.3.1 Muon Calibration

The muon calibration is also performed to correct the simulation of the muons in order to match the data, by using only CB muons. In particular, the transverse momentum in MS ($p_{\mathrm{T}}^{\mathrm{MS}}$) is affected by the energy loss in the calorimeter. The corrected transverse momentum is defined as:

$$p_{\mathrm{T}}^{\mathrm{Cor,Dec}}(\mathrm{Dec} = \mathrm{ID}, \mathrm{MS}) = \frac{p_{\mathrm{T}}^{\mathrm{MC,Dec}} + \sum_{n=0}^{1} s_n^{\mathrm{Dec}}(\eta,\phi)(p_{\mathrm{T}}^{\mathrm{MC,Dec}})^n}{1 + \sum_{m=0}^{2} \Delta r_m^{\mathrm{Dec}}(\eta,\phi)(p_{\mathrm{T}}^{\mathrm{MC,Dec}})^{m-1} g_m}, \tag{5.4}$$

where $p_{\mathrm{T}}^{\mathrm{MC,Dec}}$ is the uncorrected transverse momentum in simulation, $\Delta r_m^{\mathrm{Dec}}$ and s_n^{Dec} are the momentum resolution smearing and the scale correction in a specific (η, ϕ) detector region, and g_m are normally distributed random variables with zero mean and unit width. The numerator describes the momentum scales and the denominator describes the momentum smearing with the relative p_{T} resolution in simulation. The relative p_{T} resolution is defined as:

$$\frac{\sigma(p_{\mathrm{T}})}{p_{\mathrm{T}}} = r_0/p_{\mathrm{T}} \oplus r_1 \oplus r_2 \cdot p_{\mathrm{T}}, \tag{5.5}$$

with $\oplus$ denoting a sum in quadrature.

5.3.2 Definition

Table 5.3 shows the definition of the two criteria for the muon channel in this analysis: baseline muon and signal muon. The baseline criterion applies the loose selection for muon candidates and the signal criterion applies the

medium selection. In addition, there are also two muon selections defined as "**soft**" and "**hard**" in the same way ad for the electrons selections.

Table 5.3: Definition of baseline and signal muon.

baseline muon	signal soft(hard) muon
$p_{\mathrm{T}} > 4$ GeV	$p_{\mathrm{T}} > 4(27)$ GeV
$\|\eta\| < 2.7$	$\|\eta\| < 2.7$
Loose	Medium
-	$\|z_0 \sin\theta\| < 0.5$ mm, $\|d_0/\sigma_{d_0}\| < 5$
-	FixedCutTightTrackOnly Isolation

5.4 Jets

If high energy partons emitted, these unstable partons are decayed and hadronized into pre-stable particles: γ, $\pi^{\pm}$, K, p, n, etc. These pre-stable particles can interact with the material of the calorimeters and the showers, which are a lump of the reaction process called "jets", are reconstructed. To observe jets, a jet clustering algorithm is needed; this section describes the general jet clustering algorithm, reconstruction, calibration, and definition.

5.4.1 Jet Clustering Algorithm and Reconstruction

In general, the anti-k_t algorithm [109] is used for jet clustering at the ATLAS experiment. It is based on the k_t [110] and Cambridge/Aachen [111, 112] algorithms. This algorithm uses the distance between particles defined as:

$$d_{ij} = \min(k_{t,i}^{2p}, k_{t,j}^{2p}) \frac{\Delta_{ij}^2}{R^2}, \tag{5.6}$$

where $k_{t,i}$ is the transverse momentum ($k_{t,i} = p_{t,i}$) for a particle "i", $\Delta_{ij}^2 = (y_i - y_j)^2 + (\phi_i - \phi_j)^2$, where y_i and ϕ_i are respectively the rapidity and azimuth of a particle "i". R is the radius parameter for the cone of a jet, and p is the parameter that defines the power of transverse momentum. The distance is used to cluster particles for jet reconstruction. In case of $p = 1$, this algorithm is the same as the k_t algorithm, and the case of $p = -1$ is the anti-k_t algorithm. The k_t algorithm iteratively merges two particles (starting from those with lowest p_{T}) that are closest to each other. On the other hand, the anti-k_t algorithm iteratively merges two particles (starting from those with highest p_{T}) closest to each other. For example of anti-k_t algorithm, assuming one hard particle "1" and a soft particle "i" which are closest than any other particles, the $d_{1i} = min(1/k_{t1}^2, 1/k_{ti}^2)\Delta_{1i}^2/R^2$ is exclusively determined by the k_{t1} of hard particle and Δ_{1i} separation. In other words, soft particles tend to cluster to the hard ones, and if there are no other hard neighbouring particles within a distance $2R$, a perfectly conical jet based on the hard particles "1" can be generated by simple accumulation of all the soft particles within a circle of radius R. If another hard particle "2" exists, with $R < \Delta_{12} < 2R$, two hard jets are reconstructed. In case of $k_{t1} >> k_{t2}$, the shape of jet based on the hard "1" is perfectly conical, and the shape of jet based on the hard "2" is partly conical due to the removal of overlapping particles. In case of $k_{t1} \sim k_{t2}$, both cones are divided by a straight line with the distance b between the boundary and the center of the jet, which is determined by the requirement $\Delta R_{1b}/k_{t1} = \Delta R_{2b}/k_{t2}$. The clustering algorithm is working iteratively until $\min_{ij}(d_{ij}) > \min_i(k_{Ti}^{-2})$.

Figures 5.6 shows the results of jet clustering with different algorithms: (a) k_t algorithm, (b) anti-k_t algorithm. The event used is a simple parton-level event together with many random soft "ghosts". In case of k_t

algorithm, the shapes of jets are not uniform and the boundaries are ambiguous. On the other hand, the jets clustered by using anti-k_t algorithm have the perfectly/partly conical shape and jets are well separated. In this analysis, the radius parameter R is set to 0.4.

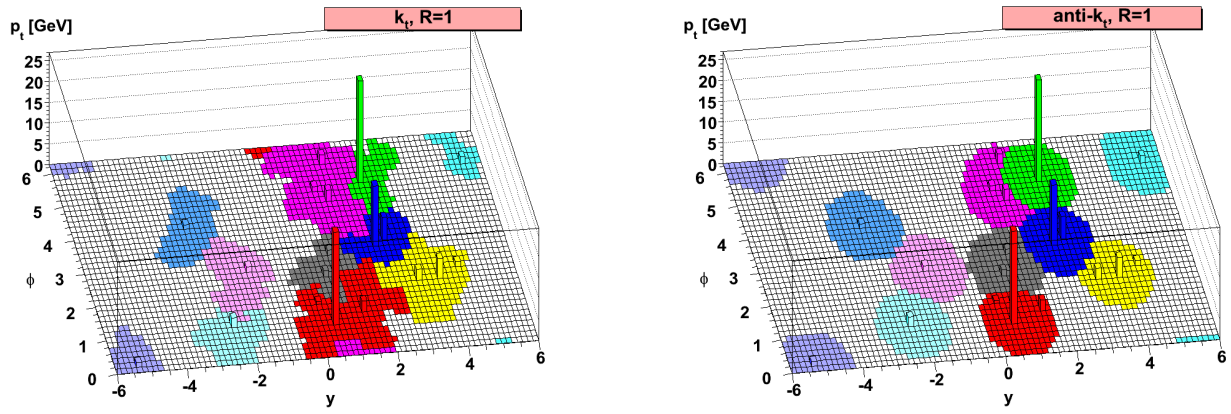

(a) (b)

Figure 5.6: The results of jet clustering corresponding to (a) the k_t algorithm and (b) anti-k_t algorithm. The event used is a simple parton-level event generated by Herwig simulation with many random soft "ghost" [109].

The input parameters for the anti-k_t algorithm are a collection of three-dimensional, massless, positive-energy topological clusters (topo-clusters), made of calorimeter cell energies. Topo-clusters are generated from the cells that contain energies above a noise threshold estimated by the electronic noise and simulated pile-up noise. In addition, the jet is compared to a true jet estimated from MC generator, which has the particle-level energy scale. The reconstructed jet is required to match the true jet with $p_{\mathrm{T}} > 7$ GeV and $|eta| < 4.5$ using the distance $\Delta R = \sqrt{(\Delta\eta)^2 + (\Delta\phi)^2}$.

5.4.2 Jet Energy Calibration

The reconstructed jet is calibrated to restore the jet energy scale to that of the true jet reconstructed at the particle-level energy scale. The full four-momentum of a reconstructed jet is scaled generally, and the Figure 5.7 presents an overview of the calibration steps for EM-scale calorimeter jets. Each step is briefly described in the following subsections and more details are given in reference [113].

First, to improve the η resolution, the four-momenta of jets are recalculated to point to the hard-scatter primary vertex. The four-momentum of the jet is recalculated for both data and MC simulation, and a correction factor called origin correction is estimated from the ratio between the reconstructed and simulated jets.

Pile-up Corrections

Next, since the extra energy from the pile-up is removed, the pile-up is corrected in two steps. The first step is the area-based correction which subtracts the per-event pile-up contribution to the p_{T} of each jet according to its area. This correction is calculated from the median p_{T} density ρ of jets in the $\eta - \phi$ plane and the definition is $\rho = p_{\mathrm{T}}/A$ where A is the area of a jet that is calculated by using the ghost association. The *rho* is calculated by using the k_t algorithm, which is chosen for its sensitivity to soft radiation. To reduce the bias from hard

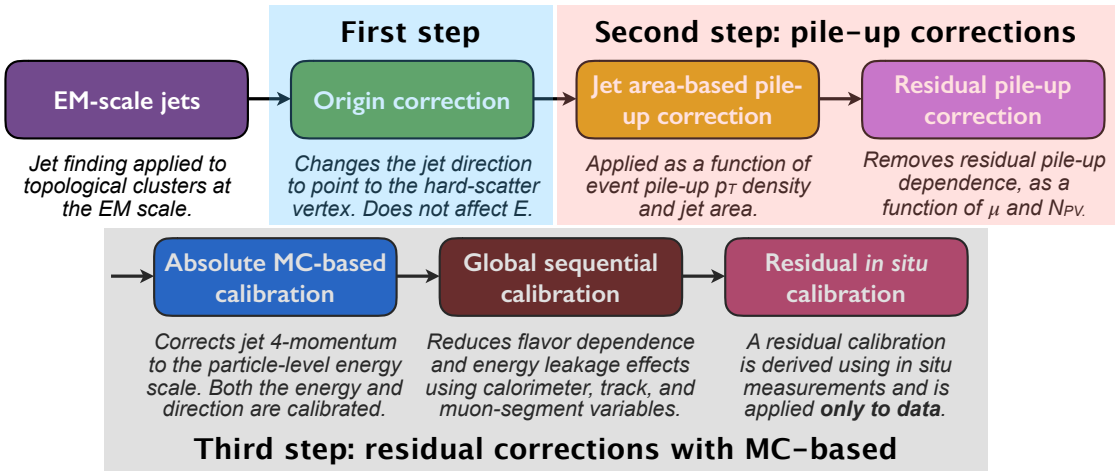

Figure 5.7: Overview of the calibration steps for EM-scale calorimeter jets [113].

scatter jets, the median p_{T} density is used for ρ. The second step is to correct for the residual p_{T} dependence on the number of primary vertices (N_{PV}) and the average number of pile-up events (μ). This dependence can be approximated from linear fits without correlation between N_{PV} and μ. The fit parameters are α and β, which correspond to the N_{PV} and μ, and the fits are done separately in bins of $p_{\mathrm{T}}^{\mathrm{truth}}$ and $|\eta|$. The pile-up corrected p_{T} ($p_{\mathrm{T}}^{\mathrm{corr}}$) is given by:

$$p_{\mathrm{T}}^{\mathrm{corr}} = p_{\mathrm{T}}^{\mathrm{reco}} - \rho \times A - \alpha \times (N_{\mathrm{PV}} - 1) - \beta \times \mu. \tag{5.7}$$

MC-based Corrections

After the pile-up correction, reconstructed jets are also corrected by using a 3-step MC-based procedure. First, the four-momentum of a reconstructed jet is corrected by using the particle-level energy scale of the simulation. The correction uses the ratios of p_{T} and η between the reconstructed jet and true jet, and they depend on p_{T} and η: $R_{p_{\mathrm{T}}}(p_{\mathrm{T}}, \eta) = p_{\mathrm{T}}^{\mathrm{reco}}/p_{\mathrm{T}}^{\mathrm{truth}}$, $R_{\eta}(p_{\mathrm{T}}, \eta) = \eta^{\mathrm{reco}}/\eta^{\mathrm{truth}}$. At the second step, the calorimeter response and jet reconstruction are sensitive to the fluctuations of the particle composition of a jet and its energy distributions. The residual after pile-up corrections and first MC-based correction is corrected by using the global sequential calibration (GSC) method, which uses information of all EM calorimeters plus all hadronic calorimeters. Finally, since the MC simulation cannot perfectly model the detector responses and the interactions between the particles and the detector material, they are corrected by using three well measured reference objects (Z, γ, multi-jets). Figure 5.8 shows the average energy response as a function of η_{det} of jets. The energy response is corrected for pile-up and is parametrized as a function of E^{reco}.

5.4.3 Flavor Tagging

The final state of signals for this analysis contains b-jets originated from the b-quarks. The flavor tagging for reconstruction and identification of b-jets from jets is important for this analysis. Basically, three different algorithms described below are used for flavor tagging:

- impact parameter based algorithm;
- inclusive secondary vertex reconstruction algorithm;
- decay chain multi-vertex reconstruction algorithm.

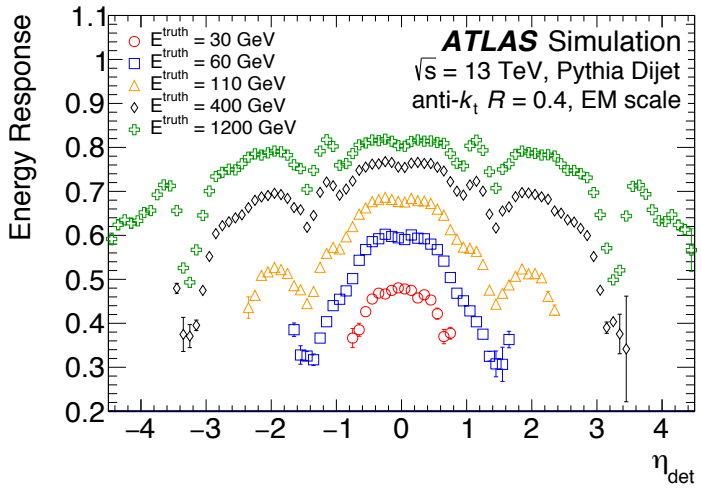

Figure 5.8: The average energy response as a function of η_{det} for jets [113].

Finally, a multivariate algorithm called MV2c20 is used to discriminate b-jets and other flavor jets by using the output variables obtained from each algorithm. This section describes these algorithms and more details are given in reference [114].

All of flavor tagging algorithms use the charged track information generated from IDs. A given track is associated with only one jet and if it satisfies the association criteria with respect to more than one jet, the jet with minimum ΔR(track, jet) is chosen. Moreover, tracks must satisfy the additional requirements (e.g. p_{T}, η) corresponding to the each algorithm.

Impact Parameter Based Algorithms: IP2D, IP3D

Impact parameter based algorithms [115] are based on the fact that a hadron containing a b-quark has long lifetime ($c\tau \sim 450\mu$m). Tracks corresponding to a b-jet tend to have a larger impact parameter than the tracks correspond-ing to the other flavor jets. Thus, the signed impact parameter ($d_0, Z_0 \sin\theta$) significances are used for these algorithms. These algorithms calculate the log likelihood ratio for b- and other-flavor hypothesises, and it discriminates between a b-jet and another flavor jet.

The difference between the IP2D and IP3D algorithms is whether the longitudinal impact parameter ($Z_0 \sin\theta$) is used or not. The IP2D algorithm uses only the transverse impact parameter (d_0), while the IP3D algorithm uses both impact parameters. Typically the longitudinal impact parameter is not affected by the pile-up, and the IP2D algorithm has good robustness against the effects of pile-up. Figure 5.9 shows the distributions of the log-likelihood ratio for the IP2D (a) and IP3D (b) b-tagging algorithm. The shape of light-flavor (dotted red) jets distribution for IP2D has a clear exponential tail at high positive values. On the other hand, the shape of light-flavor (dotted red) jets distribution for IP3D is affected by small effects of pile-up on the longitudinal impact parameter. Both distributions of b-jets (solid green) for each algorithm obtain higher value of log-likelihood ratio, compared to the light-flavor jets.

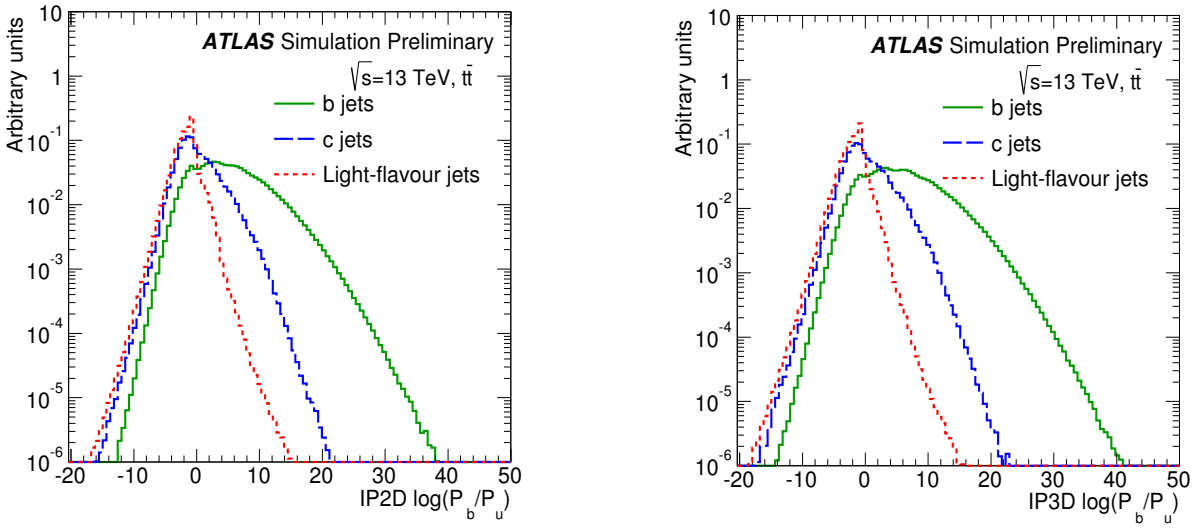

(a) (b)

Figure 5.9: The distributions of the log likelihood ratio for (a) IP2D and (b) IP3D b-tagging algorithm [115].

Second Vertex Finding Algorithm: SV

This algorithm is used to explicitly reconstruct an inclusive displaced secondary vertex within the jet. This algorithm reconstructs two-track vertices from the candidate tracks, and these tracks are rejected if they form a secondary vertex originated from the decay of unstable particles: long-lived particles (e.g. K_S, Λ), photon conversion, or particles produced by the hadronic interaction with the detector material. After that, a single vertex is reconstructed by using the tracks that survive this preselection.

Decay Chain Multi-Vertex Algorithm: JetFitter

The multi-vertex reconstruction algorithm can reconstruct the decay for PV $\rightarrow$ b-jet $\rightarrow$ c-jet using the topological structure of a weak b- and c-hadron decay. The output of this algorithm can be obtained by a Kalman filter approximating the b-hadron flight path.

Multivariate Algorithm: MV2

Finally, b-jets and other-flavor jets are discriminated by using a multivariate analysis called MV2 [116] that is based on a boosted decision tree (BDT) which takes as input the output variables generated from three basic algorithms. BDT training uses 5 million $t\bar{t}$ events. Figure 5.10 shows the MV2c20 output for b- and other-flavor jets in $t\bar{t}$ events, and the light-flavor and c-jet rejection as a function of b-jet efficiency for MV2c00, MV2c10, MV2c20 b-tagging algorithms in $t\bar{t}$ events. All MV2 algorithms use a sample of jets containing b-jets as signal and other-flavor jets as backgrounds for BDT training, and they differ by the ratio of the contamination of b-jets and other-flavor jets. MV2c00 algorithm uses only background jets that are light-flavor jets for the training, while the background composition for MV2c10 is 93% light-flavor jets and 7% c-jets, and for MV2c20 it is 80% light-flavor jets and 20% c-jets.

MV2c10 has a larger rejection for c-jets, however it has a lower rejection for light-flavor jets, while the performance of MV2c10 and MV2c20 is comparable. This analysis uses the MV2c10 algorithm for b-tagging.

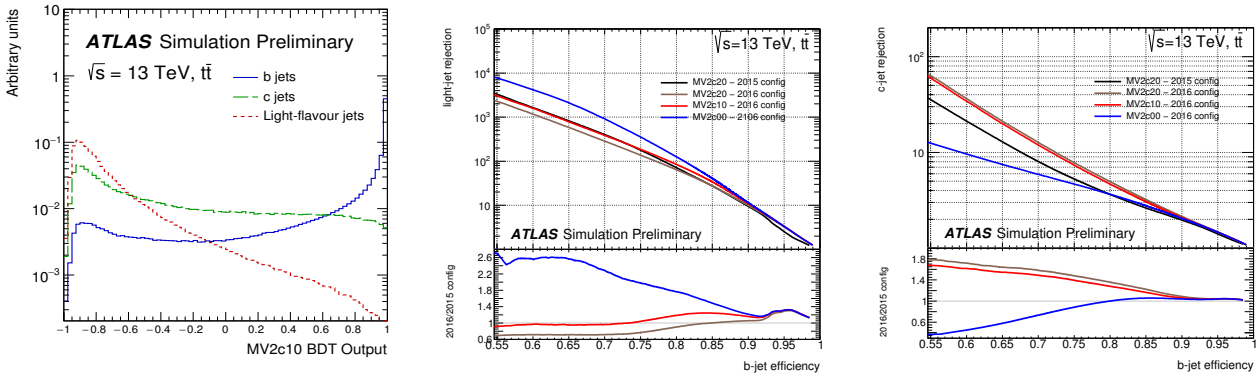

(a) (b) (c)

Figure 5.10: (a) MV2c10 output for b- and other-flavor jet, and (b) the light-flavor and (c) c-jet rejection as a function of b-jet efficiency in $t\bar{t}$ events [116].

Table 5.4 shows the definition of the operating points calculated when integrating over all jets in the $t\bar{t}$ sample. According to the above results, we decided to use in this analysis the third row operating point with 77% b-jet efficiency.

Table 5.4: Operating points for MV2c10 b-tagging algorithm [116].

BDT Cut value	b-jet Efficiency [%]	c-jet Rejection	τ-jet Rejection	Light-jet Rejection
0.9349	60	34	184	1538
0.8244	70	12	55	381
0.6459	77	6	22	134
0.1758	85	3.1	8.2	33

5.4.4 Suppression of Pile-up Jets

Since the pile-up becomes an important component for the jet energy fraction and it affects the flavor tagging, we need to reduce the pile-up jets [117]. The additional transverse energy (E_{T}) originated from the pile-up jet can be estimated typically to subtract on average from the signal interaction of interest. The jet-vertex-fraction (JVF), defined as the ratio of the transverse momentum sum can remove the pile-up jet with minimal JVF requirement:

$$\mathrm{JVF} = \frac{\sum_k p_{\mathrm{T}}^{\mathrm{trk_k}}(\mathrm{PV}_0)}{\sum_l p_{\mathrm{T}}^{\mathrm{trk_l}}(\mathrm{PV}_0) + \sum_{n\geq 1}\sum_l p_{\mathrm{T}}^{\mathrm{trk_l}}(\mathrm{PV}_n)}. \tag{5.8}$$

Here, PV_0 is the hard-scatter vertex and $\mathrm{PV}_j; j \geq 1$ corresponds to primary vertices that are generated by the pile-up interactions in the same bunch crossing. The case of JVF $= -1$ indicates that there are no tracks associated to jets. The number of reconstructed primary vertices increases corresponding to the increase of the number of pile-up tracks, and the denominator also increases corresponding to the number of reconstructed primary vertices. Hence, in case of a signal jet originated from hard-scatter interaction, the value of JVF tends to shift to small values.

The point is that the hard-scatter jet efficiency depends on the number of reconstructed primary vertices

($N_{\mathrm{V_{tx}}}$). To fix this dependency, two track-based variables are developed: corrJVF and $R_{p_{\mathrm{T}}}$. The pile-up jet and the signal jet are discriminated by using a multivariate analysis that takes as input the variables corrJVF and $R_{p_{\mathrm{T}}}$. Both variables are computed from the combined information of the calorimeter and tracking and they are defined as:

$$\mathrm{JVF} = \frac{\sum_k p_{\mathrm{T}}^{\mathrm{trk_k}}(\mathrm{PV}_0)}{\sum_l p_{\mathrm{T}}^{\mathrm{trk_l}}(\mathrm{PV}_0) + \frac{\sum_{n\geq 1}\sum_l p_{\mathrm{T}}^{\mathrm{trk_l}}(\mathrm{PV}_n)}{k\cdot n_{\mathrm{trk}}^{\mathrm{PU}}}}, \quad R_{p_{\mathrm{T}}} = \frac{\sum_k p_{\mathrm{T}}^{\mathrm{trk_k}}(\mathrm{PV}_0)}{p_{\mathrm{T}}^{jet}}. \tag{5.9}$$

Basically, corrJVF is similar to the JVF. To correct the linear increase of an average of $p_{\mathrm{T}}^{\mathrm{PV}}$, the term which denotes the scalar p_{T} sum of the associated tracks originated from pile-up interactions is divided by the total number of pile-up tracks ($n_{\mathrm{trk}}^{\mathrm{PU}}$) and its coefficient. Figure 5.11(a) shows the distribution of corrJVF for pile-up and hard-scatter jets with $20 < p_{\mathrm{T}} < 30$ GeV. The distributions of corrJVF for pile-up and hard-scatter jets are different. The next variable $R_{p_{\mathrm{T}}}$, shown in Figure 5.11(b), is defined as the scalar p_{T} sum of the tracks associated with the jet. These tracks originate from the hard-scatter vertex divided by the fully calibrated jet p_{T}. Finally, a new discriminant called the jet-vertex-tagger (JVT) is constructed using the corrJVF and $R_{p_{\mathrm{T}}}$. Figure 5.11(c) shows the JVT distribution for hard-scatter and pile-up jets with $20 < p_{\mathrm{T}} < 30$ GeV. A value of JVT = -1 is assigned to jets with no associated tracks.

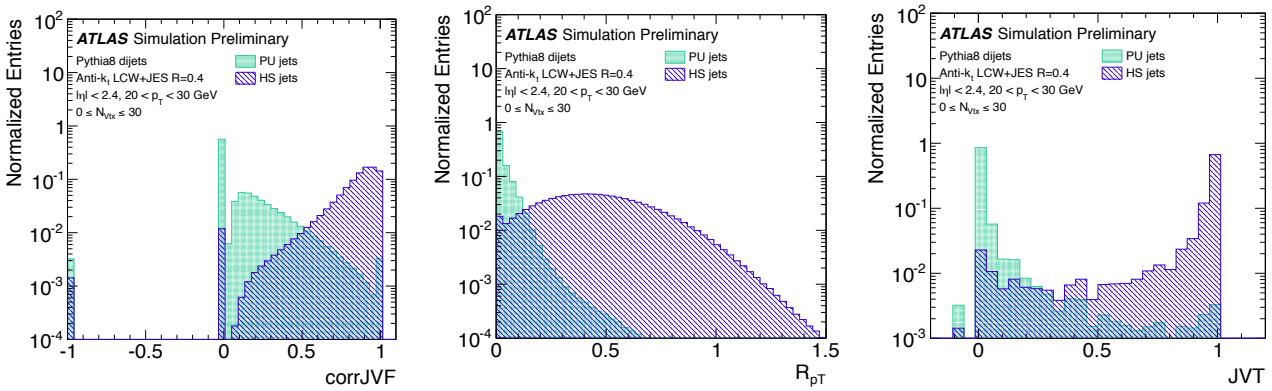

(a) (b) (c)

Figure 5.11: (a) The distribution of corrJVF for pile-up and hard-scatter jets with $20 < p_{\mathrm{T}} < 30$ GeV, (b) the distribution of $R_{p_{\mathrm{T}}}$ for pile-up and hard-scatter jets and (c) JVT distribution to input the outputs generated from corrJVT and $R_{p_{\mathrm{T}}}$ [117].

5.4.5 Jet Definition

Table 5.5 shows the definition of the three criteria for jets and b-tagging used in this analysis: baseline jet, signal jet, b-tagged jet. The baseline criterion is applied only for jet candidates with p_{T} above 20 GeV, and the signal criterion adds η and JVT selection values. In addition, the criterion of b-jets includes the signal jet criterion and additional MV2c10 selection for b-tagging, except for the p_{T} selection value, which is the same as for the baseline criterion.

5.5 Missing Transverse Momentum

The final states of the signal considered in this analysis contains two neutralinos and one neutrino, which cannot be detected by the ATLAS detector. For this reason, the direct reconstruction of any neutralinos and neutrinos is impossible, and we need to reconstruct of the momenta of these particles using kinematic information of the

Table 5.5: Definition of baseline jets, signal jets, and b-jets.

baseline jet	signal jet	b-jet
$p_{\mathrm{T}} > 20$ GeV	$p_{\mathrm{T}} > 25$ GeV $\|\eta\| < 2.5$ JVT = 0.59 for $\|\eta\| < 2.4$ and $p_{\mathrm{T}} < 60GeV$	$p_{\mathrm{T}} > 20$ GeV $\|\eta\| < 2.5$ JVT = 0.59 for $\|\eta\| < 2.4$ and $p_{\mathrm{T}} < 60GeV$ MV2c10 > 0.6459 ($\epsilon_{b-tagging} > 77\%$)

final state particles. In case of the pp collisions, the longitudinal momentum, which is parallel to the beam axis is not constrained due to the unknown initial parton momentum, but fortunately the transverse momentum is known. The missing transverse momentum ($E_{\mathrm{T}}^{\mathrm{miss}}$) is measured as an imbalance in the sum of visible transverse momenta and it includes the transverse momenta of the invisible particles, such as neutralinos and neutrinos. The $E_{\mathrm{T}}^{\mathrm{miss}}$ reconstruction uses the calibrated hard objects and soft-term containing the residual visible momenta mainly from soft jets ($p_{\mathrm{T}} < 20$ GeV) and misidentified muons, and it is defined as:

$$E_{\mathrm{T}}^{\mathrm{miss}} = \sqrt{(E_x^{\mathrm{miss}})^2 + (E_y^{\mathrm{miss}})^2}, \tag{5.10}$$

$$\text{components: } E_{x(y)}^{\mathrm{miss}} = \sum_{\text{particles}=(\mathrm{e},\gamma,\tau,\text{jets},\mu)} E_{x(y)}^{\mathrm{miss,particles}} + E_{x(y)}^{\mathrm{miss,soft-term}}, \tag{5.11}$$

where $E_{x(y)}^{\mathrm{miss}}$ is the component of $E_{\mathrm{T}}^{\mathrm{miss}}$ and they can be calculated from the sum of object terms. Each object term is given by the negative vectorial sum of the momenta corresponding to each particle ($E_{x(y)}^{\mathrm{miss,particles}} = -\sum p_{x(y)}^{\mathrm{miss,particles}}$). This calculation uses all baseline electrons, muons, photons, τ, and jets, and the overlap of these objects is removed. The soft-term is calculated by the track soft term algorithm (TST)) [118], and the TST sums over the momenta of tracks that are reconstructed by using the information of only inner detectors and not associated to any jets. In addition, the tracks with momentum uncertainties larger than 40% are removed.

5.5.1 $E_{\mathrm{T}}^{\mathrm{miss}}$ Triggers

This analysis focuses on both signal topologies with high $E_{\mathrm{T}}^{\mathrm{miss}}$ described in Section 6 and 7. Thus, we use the datasets which are selected by $E_{\mathrm{T}}^{\mathrm{miss}}$ triggers called xe trigger to get signal-like events. The threshold of the xe trigger are sometimes changed during the run in order to keep trigger rates under control and thus the datasets corresponding to the $E_{\mathrm{T}}^{\mathrm{miss}}$ trigger used in this analysis are:

- HLT_xe70_L1XE50 (2015);
- HLT_xe90_mht_L1XE50 (2016, A-D3);
- HLT_xe100_mht_L1XE50 (2016, D4-F1);
- HLT_xe110_mht_L1XE50 (2016, F2-L).

Here, L1XE indicates the use to the $E_{\mathrm{T}}^{\mathrm{miss}}$ trigger based on roughly reconstructed $E_{\mathrm{T}}^{\mathrm{miss}}$ from the L1 calorimeter RoIs. The transverse energy threshold is above 50 GeV. After passing the L1 trigger, the HLT trigger algorithms (HLT_xe) are used. The HLT_xe70_L1XE50 used in 2015 data-taking is calculated based on the calorimeter cells approach. This calculates the contribution of $E_{\mathrm{T}}^{\mathrm{miss}}$ by the summation of $p_{x,y}^{i} = E_i \cos\theta_i \sin\phi_i$ obtained at each cell in both LAr and tile calorimeter. Finally, $E_{\mathrm{T}}^{\mathrm{miss}}$ is calculated by the negative vectorial sum of each cell's contribution. The xe trigger with mht calculates $E_{\mathrm{T}}^{\mathrm{miss}}$ directly by summing over the jets reconstructed with the trigger algorithm.

To identify the trigger plateau, the efficiency for the xe trigger is studied. For this purpose, we use events taken by the single lepton trigger and we select events with exactly 1 lepton, at least 4 jets and least 1 b-tag. In other to reduce the contamination from multi-jet events, further cleaning cuts are applied: $m_T > 30$ GeV, $|\Delta\phi(\text{jet}_i, \vec{p}_{\text{T}}^{\text{miss}})| > 0.4$ with $i = 1.2$. Figure 5.12 shows the $E_{\text{T}}^{\text{miss}}$ trigger efficiencies as a function of the offline $E_{\text{T}}^{\text{miss}}$. The agreement of the trigger efficiency in data and MC is good in both channels down to 200 GeV. The trigger efficiency is above 98% for $E_{\text{T}}^{\text{miss}} > 230$ GeV , and thus this analysis requires the offline threshold value to be 230 GeV.

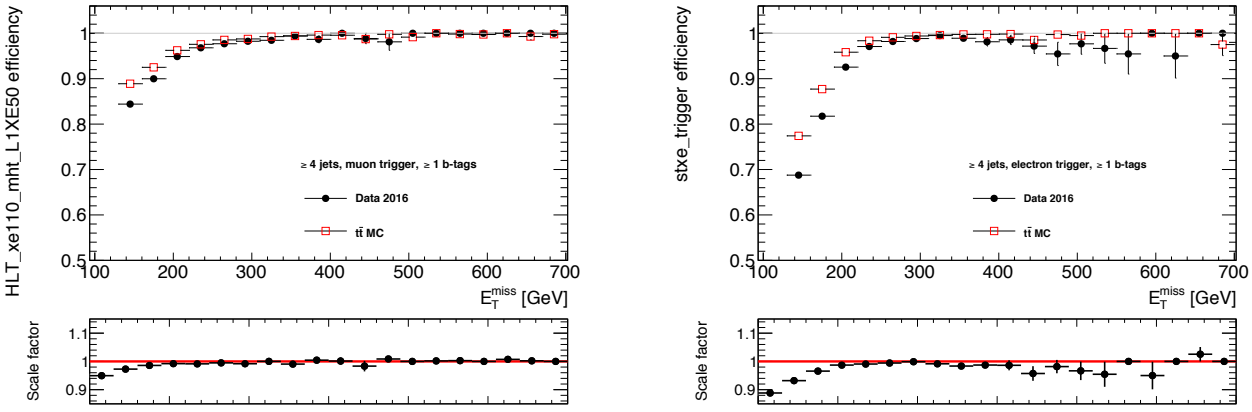

(a) (b)

Figure 5.12: Trigger efficiency (a) for HLT_xe110_mht_L1XE50 in muon events and (b) for stxe trigger (including xe90, xe100 and xe110) electron events.

5.6 Overlap Removal

When candidates that pass the object selection overlap with each other, we need to remove the overlap in order to avoid double-counting. The overlap removal (OR) procedure restores the correct objects by comparing candidates with the selection corresponding to each object. In addition, the OR procedure is based on an improved acceptance for real leptons, and the optimal OR procedure is detailed below:

1. Electron/Muon OR: The loose muons are reconstructed from the calo-tagged muons, and they can also be reconstructed as electrons. If a muon and an electron overlap within $\Delta R < 0.01$, the muon is removed if it is a calo-tagged muon, else the electron is removed;
2. Electron/Jet OR: If a baseline electron and a baseline non b-tagged jet are found within $\Delta R < 0.2$, the object is interpreted as an electron and the overlapping jet is removed;
3. Muon/Jet OR: If a baseline muon can be the same as a baseline non b-tagged jet with the ghost-matched algorithm within $\Delta R < 0.4$, the object is interpreted as a muon if either of the following requirements is satisfied:
   - The jet has less than 3 tracks with $p_{\text{T}} > 500$ MeV,
   - The p_{T} ratio of the muon and jet is greater than 0.7 ($p_{\text{T}}^{\mu}/p_{\text{T}}^{\text{jet}} > 0.7$);
4. Jet/Lepton OR: If a jet passing previous OR steps overlaps with a lepton in a cone of radius $R = 0.04 + 10/p_{\text{T}}^{\ell}$ (up to a maximum radius of 0.4), the lepton is removed;
5. Electron/Tau OR: If an electron passing previous OR steps overlaps with a tau in a cone of radius $R = 0.1$, the tau is removed;

6. Tau/Jet OR: Tau objects are only used to compute the m_{T2}^{τ} variable described in reference [119] and veto on it. If the event passes the veto the tau object is no longer used and instead the jet object is considered for the rest of the computations.

Chapter 6

Analysis for the Higgsino LSP Scenario

This chapter describes the search for stop pair production in the higgsino LSP scenario. The sections provide the target event topology, the event selection, the background estimation, the statistical analysis, the systematic uncertainties, and the result.

6.1 Event Topology

Figure 6.1 shows the target event topology of the analysis of the higgsino LSP scenario. This analysis focuses on a scenario with mass difference between the chargino and the neutralino to be 5 GeV. The momentum of final state particles and $E_{\mathrm{T}}^{\mathrm{miss}}$ are relatively low because a large part of the momentum or the energy of the chargino is used to generate the neutralino. It is challenging to detect low momentum particles with a high detection efficiency and an effective suppression of background particles. Therefore, a specific topology with the ISR with high momentum (high-ISR) is employed. The final state particles are boosted and can have higher momenta. The target event contains at least one high-p_{T} jet, large $E_{\mathrm{T}}^{\mathrm{miss}}$, and one isolated soft lepton (ℓ). The event selection has been optimized for two benchmark parameter sets (a) $(m_{\tilde{t}_1}, m_{\tilde{\chi}_1^\pm}, m_{\tilde{\chi}_1^0})$ = (350 GeV, 305 GeV, 300 GeV) and (b) $(m_{\tilde{t}_1}, m_{\tilde{\chi}_1^\pm}, m_{\tilde{\chi}_1^0})$ = (300 GeV, 255 GeV, 250 GeV).

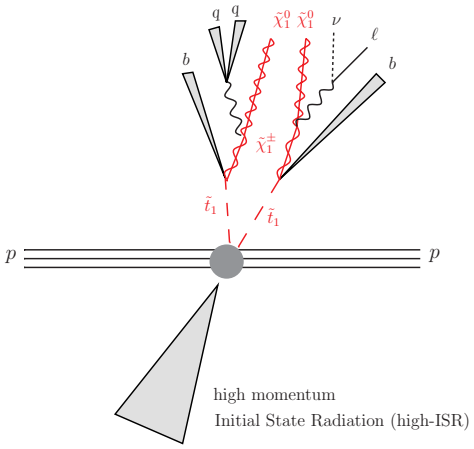

Figure 6.1: Illustration of the target event topology with high-ISR.

There are two main SM backgrounds. One is the $t\bar{t}$ background and the other is the W + jets background. The $t\bar{t}$ production has a large cross section in pp collisions, and a top quark decays into one W boson and b quark with nearly 100% BR. In case a W boson decays into lepton pair, the final state has exactly same particles. In case a lepton is reconstructed for the $t\bar{t}$ events with hadronic W decays (fake lepton), the event constitute a background. The W + jetsbackground arises when the W boson decays to a lepton pair and the jets include a high-p_{T} jet. Figures 6.2 show the illustrations of the event topology for signal, $t\bar{t}$, and W + jets. Typically, $t\bar{t}$ and W + jets backgrounds have decay products in both directions with respect to $\vec{p}_{\mathrm{T}}^{\,\mathrm{miss}}$.

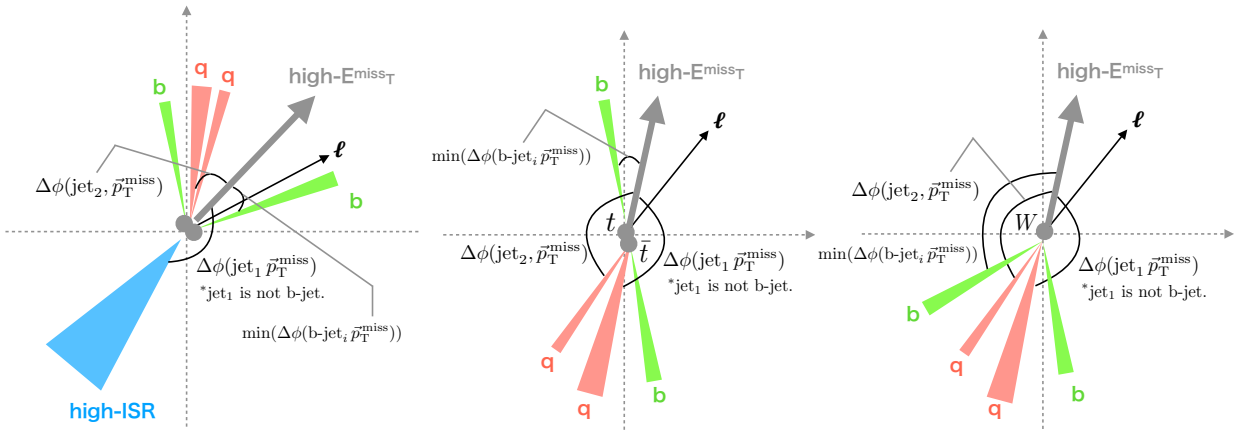

Figure 6.2: Event topologies for (a) signal and main backgrounds (b) $t\bar{t}$ and (c) W + jets.

6.2 Event Selection for Signal Region

The events of pp collisions' data have to be selected to obtain the signal like events. A signal region (SR) is defined with kinematic variables. Table 6.1 shows the summary of SR for the higgsino LSP scenario. The requirements on kinematic variables are determined as explained in the following subsections.

6.2.1 Preselection

Preselection of the events is defined for the higgsino LSP scenario. The jet with the highest p_{T} should not be a b-tagged jet because ISR is mostly light flavor quarks. It is required to have p_{T} higher than 400 GeV. $E_{\mathrm{T}}^{\mathrm{miss}}$ is required to be higher than 230 GeV so that the trigger efficiency is inside the plateau region (see Section 5.5.1). Exactly one lepton with p_{T} higher than 4 GeV for a muon (5 GeV for an electron) is required. At least two jets including minimum one b-tagged jet are required.

6.2.2 Kinematic Variables

Several kinematic variables are defined to reduce the SM backgrounds and to enhance the signal sensitivity in the SR.

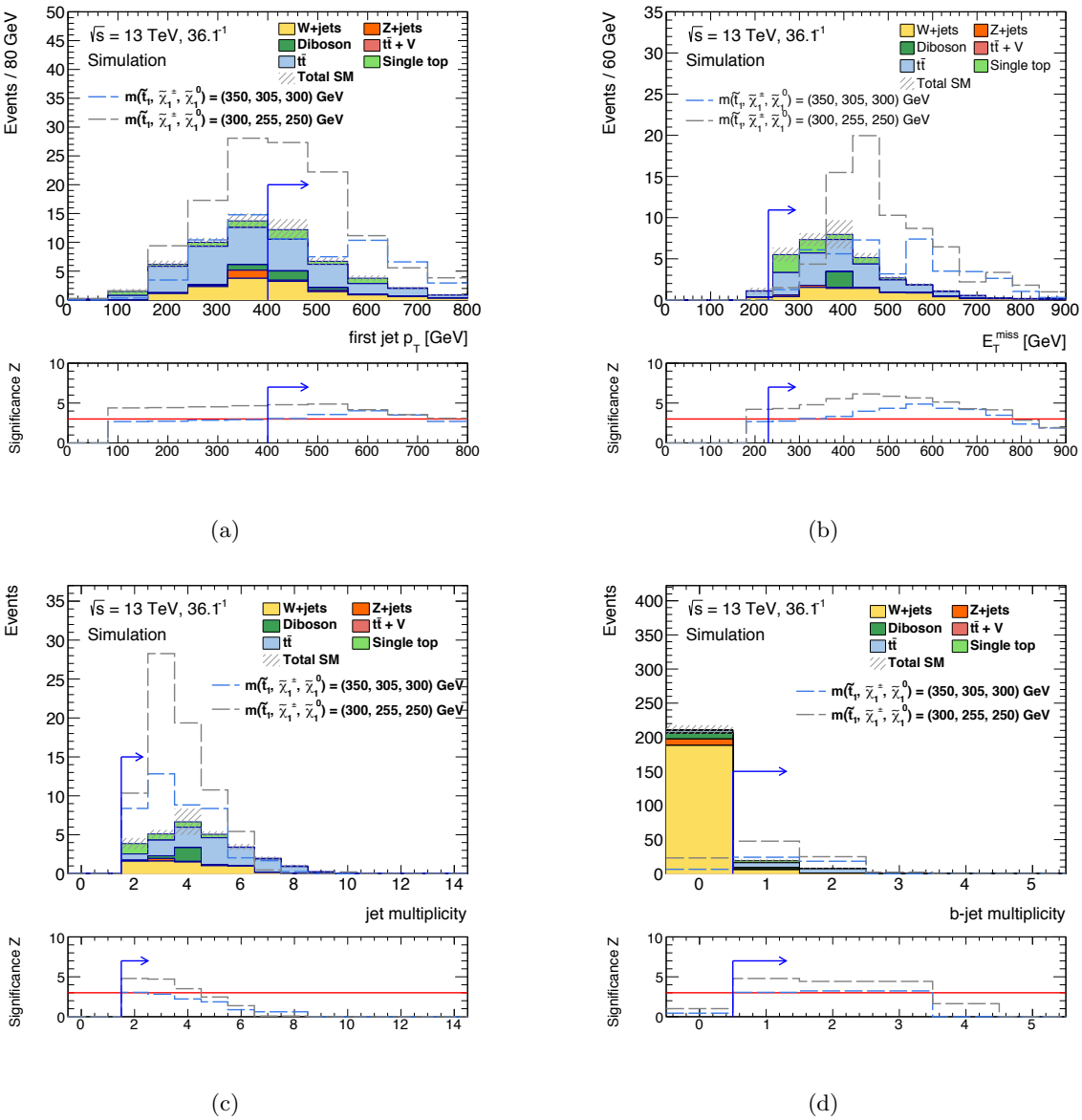

Figure 6.3: Distributions of the variables used for preselection for the higgsino LSP scenario: (a) $p_{\mathrm{T}}^{\mathrm{jet}_1}$, (b) $E_{\mathrm{T}}^{\mathrm{miss}}$, (c) jet multiplicity, and (d) b-tagged jet multiplicity.

Table 6.1: Summary of the event selection for SR of the higgsino LSP scenario. The jet with the highest p_{T} among the jets in an event should not be b-tagged.

Cut Variables	Requirements
Trigger	$E_{\mathrm{T}}^{\mathrm{miss}}$ triggers
Data quality	Jet cleaning, cosmic-ray muon veto, primary vertex
Second lepton veto	No additional baseline lepton
Number of lepton, tightness	= 1 signal soft lepton
Lepton p_{T} [GeV]	≥ 4 for μ, ≥ 5 for e
Number of (signal jets, b-tags)	(≥ 2, ≥ 1)
Jet p_{T} [GeV]	(> 400 for the highest p_{T}, > 25 for the other)
m_{T} [GeV]	< 50
$E_{\mathrm{T}}^{\mathrm{miss}}$ [GeV]	> 300
$\lvert\Delta\phi(\mathrm{jet}_1, \vec{p}_{\mathrm{T}}^{\mathrm{miss}})\rvert$, $\lvert\Delta\phi(\mathrm{jet}_2, \vec{p}_{\mathrm{T}}^{\mathrm{miss}})\rvert$	> 0.4, > 0.4
$\min(\Delta\phi(\vec{p}_{\mathrm{T}}^{\mathrm{miss}}, b\text{-jet}))$	< 1.5
$p_{\mathrm{T}}^{\ell}/E_{\mathrm{T}}^{\mathrm{miss}}$	< 0.02
$m_t^{\mathrm{reclustered}}$ [GeV]	< 150

Transverse Mass

Transverse mass m_{T} is defined as the invariant mass calculated from the energy and momentum in a plane perpendicular to the beam axis for a particle which decays into two particles. This variable can be calculated from one visible particle and another invisible particle such as neutrino:

$$m_{\mathrm{T}} = \sqrt{2 \cdot p_{\mathrm{T}}^{\ell} \cdot E_{\mathrm{T}}^{\mathrm{miss}} \ (1 - \cos\Delta\phi(\vec{\ell},\ \vec{p}_{\mathrm{T}}^{\mathrm{miss}}))}. \tag{6.1}$$

Here p_{T}^{ℓ} is the lepton p_{T}, and $\Delta\phi(\vec{\ell},\ \vec{p}_{\mathrm{T}}^{\mathrm{miss}})$ is the azimuthal angle between the lepton and $\vec{p}_{\mathrm{T}}^{\mathrm{miss}}$ directions. This variable is used to characterize the mass of a leptonically decaying W boson. The distribution provides a Jacobian peak at W boson mass (about 80 GeV). Since only transverse information is used to calculate m_{T}, m_{T} is a good kinematic variable to separate the signal and the background in the environment where the longitudinal information of a neutrino can not be obtained.

Minimum Azimuthal Opening Angle

The minimum azimuthal opening angle $\min(\Delta\phi(\vec{p}_{\mathrm{T}}^{\mathrm{miss}}, b\text{-jet}))$ is defined as the minimum azimuthal angle between b-jet and $\vec{p}_{\mathrm{T}}^{\mathrm{miss}}$ among all possible pairs of b-jet and $\vec{p}_{\mathrm{T}}^{\mathrm{miss}}$. The signal events have smaller value due to high-ISR.

Ratio between Lepton Transverse Momentum and Missing Transverse Energy

The ratio between lepton transverse momentum and missing transverse energy $p_{\mathrm{T}}^{\ell}/E_{\mathrm{T}}^{\mathrm{miss}}$ is lower for signal events due to low-p_{T} lepton and high $E_{\mathrm{T}}^{\mathrm{miss}}$.

Reconstructed Top Mass

The reconstructed top mass $m_t^{\mathrm{reclustered}}$ is used to suppress $t\bar{t}$ backgrounds with di-leptonic or semi-leptonic decays. Figure 6.4 shows the illustrations of the top reconstruction algorithm. An algorithm based on the anti-k_t clustering of small-radius jets is used. First, all small-radius jets in the event are clustered by using the anti-k_t algorithm with a large radius parameter $R_0 = 3.0$. Next, each of the resulting very-large-radius jets are

iteratively shrunk, until their radius matches their p_{T}, following the approximation $R(p_{\mathrm{T}}) = 2 \times 175\ \mathrm{GeV}/p_{\mathrm{T}}$ within the range $(0.3 < R < 0.5)$. Figure 6.5 shows the distribution of the mass of the reconstructed top candidates for di-leptonic or semi-leptonic $t\bar{t}$ events. The semi-leptonic $t\bar{t}$ event has the peak around 175 GeV.

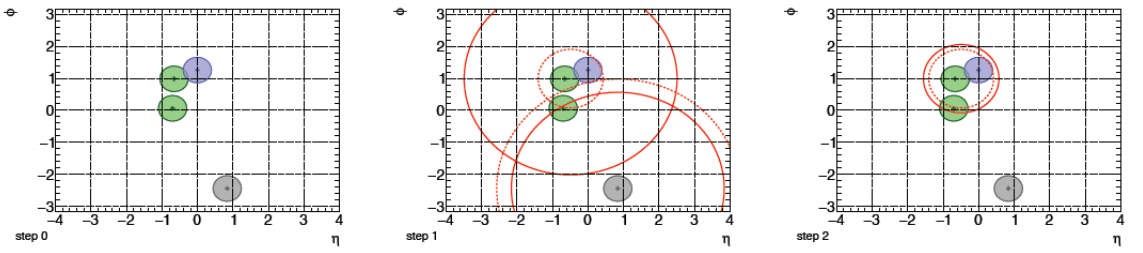

(a) All jets in the event.

(b) Initial clustering with $R_0 = 3.0$, yielding two candidate objects.

(c) Final step of the algorithm, with one candidate shrunk to fit the p_{T} and the other one discarded.

Figure 6.4: The illustration of the top reconstruction algorithm.

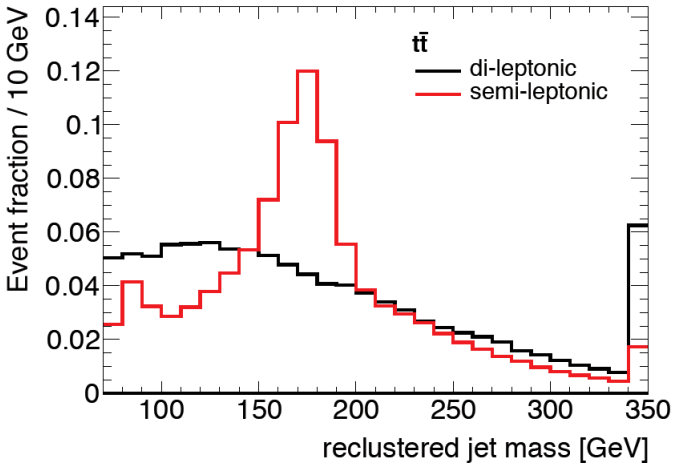

Figure 6.5: The black (red) histogram shows the reclustered jet mass for $t\bar{t}$ events with di-leptonic (semi-leptonic) decays.

6.2.3 SR Optimization

The selection for the SR was optimized to reject the SM backgrounds as much as possible and to obtain a high sensitivity of the excess from the SM prediction. All SM backgrounds, which are considered to remain in the SR, were taken into account by using the MC simulation: $t\bar{t}$, W + jets, single-produced top quark (single-top), top quark pair production in association with vector boson ($t\bar{t} + V$), Z boson production in association with jets (Z + jets) and two vector-bosons production (diboson). The total background systematic uncertainty was assumed to be 30% for this optimization.

The expected sensitivity is calculated by using the statistical method described in Appendix A. A background-only hypothesis testing was used. The significance Z value ($Z = \Phi^{-1}(1-p)$, where p is the p-value), which is approximated by using numerical method [120, 121], is used for the SR optimization. If $Z = 3$ (it is equivalent

to $p = 1.3 \times 10^{-3}$), an evidence of the inconsistency between the data and the background-only hypothesis is implied.

6.2.4 Selection Optimization Scan

The selection is optimized to obtain a higher Z value. The baseline selections are set before the optimization:

- exactly one signal soft lepton (described in Section 5.2.2 and 5.3.2)
- $E_{\mathrm{T}}^{\mathrm{miss}} > 230$ GeV for $E_{\mathrm{T}}^{\mathrm{miss}}$ trigger efficiency plateau,
- $N_{\mathrm{jets}} \geq 2$ signal jets (signal jets described in Section 5.4.5),
- $p_{\mathrm{T}}^{\mathrm{jet}_1} > 400$ GeV,
- $N_{\text{b-jets}}(p_{\mathrm{T}}^{\text{b-jets}} > 25 \text{ GeV}) \geq 1$.

After requiring the baseline selection, the requirements for other kinematic variables are optimized. To reduce the uncertainty on the expected Z value, the selection is optimized with the number of events after the selection no to be too small. Table 6.2 shows the scanned cut values. The final optimal values are shown in Table 6.1.

Table 6.2: The list of scanned cut values of several kinematic variables.

Cut variables	Scanned cut values
$E_{\mathrm{T}}^{\mathrm{miss}}$ [GeV]	$> 230, > 300, > 360, > 420, > 480$
m_{T} [GeV]	$< 150, < 125, < 100, < 75, < 50$
$\min(\Delta\phi(\vec{p}_{\mathrm{T}}^{\mathrm{miss}}, b\text{-jet}))$	$< 2.2, < 1.8, < 1.5, < 1.3, < 0.9$
$p_{\mathrm{T}}^{\ell}/E_{\mathrm{T}}^{\mathrm{miss}}$	$< 0.05, < 0.04, < 0.03, < 0.02, < 0.01$
$m_t^{\mathrm{reclustered}}$ [GeV]	$< 250, < 200, < 150, < 100, < 50$

If the cut value of $E_{\mathrm{T}}^{\mathrm{miss}}$ (Figure 6.3(b)) is 300 GeV, the Z value is more than 3 for the benchmark point (a). The peak Z value is obtained with $E_{\mathrm{T}}^{\mathrm{miss}} > 420$, but the numbers of events for signal and backgrounds are less and the statistical uncertainty becomes larger. Therefore, the $E_{\mathrm{T}}^{\mathrm{miss}}$ is 300 GeV. Figure 6.6(a) shows the m_{T} distribution for the events for which all the requirements except for the m_{T} requirement are applied. Since the $t\bar{t}$ and W + jets backgrounds can have one lepton and neutrino from W boson decay, m_{T} distributions of those backgrounds have a peak around the W boson mass. In addition, m_{T} distribution for dileptonic $t\bar{t}$ events, where one lepton is not identified, is outside the detector acceptance, or is a hadronically decaying tau lepton, tend to have a higher value due to a requirement of high $E_{\mathrm{T}}^{\mathrm{miss}}$. Therefore, m_{T} is required to be less than 50 GeV. Figure 6.6(b) shows the distributions of $\min(\Delta\phi(\vec{p}_{\mathrm{T}}^{\mathrm{miss}}, b\text{-jet}))$ for the events for which all the requirements except for the $\min(\Delta\phi(\vec{p}_{\mathrm{T}}^{\mathrm{miss}}, b\text{-jet}))$ requirement are applied. To reduce W + jets background, which has flat $\min(\Delta\phi(\vec{p}_{\mathrm{T}}^{\mathrm{miss}}, b\text{-jet}))$ distribution restriction of the direction for b-tagged jets, $\min(\Delta\phi(\vec{p}_{\mathrm{T}}^{\mathrm{miss}}, b\text{-jet}))$ is required to have less than 1.5. Figure 6.6(c) shows the $p_{\mathrm{T}}^{\ell}/E_{\mathrm{T}}^{\mathrm{miss}}$ distribution. The signal has a soft lepton and high $E_{\mathrm{T}}^{\mathrm{miss}}$, while, the backgrounds such as $t\bar{t}$ and W + jets have a high-p_{T} lepton when they have high $E_{\mathrm{T}}^{\mathrm{miss}}$. Therefore, the ratio for the signal has the peak in the low $p_{\mathrm{T}}^{\ell}/E_{\mathrm{T}}^{\mathrm{miss}}$ region and $p_{\mathrm{T}}^{\ell}/E_{\mathrm{T}}^{\mathrm{miss}}$ is required to be less 0.02. Figure 6.6(d) shows the $m_t^{\mathrm{reclustered}}$ distribution. Since a stop of the signal event can not decay into the top quark, the signal events have a peak at around zero. The $t\bar{t}$ backgrounds have a peak at around 175 GeV. Therefore, $m_t^{\mathrm{reclustered}}$ is required to be less than 150 GeV.

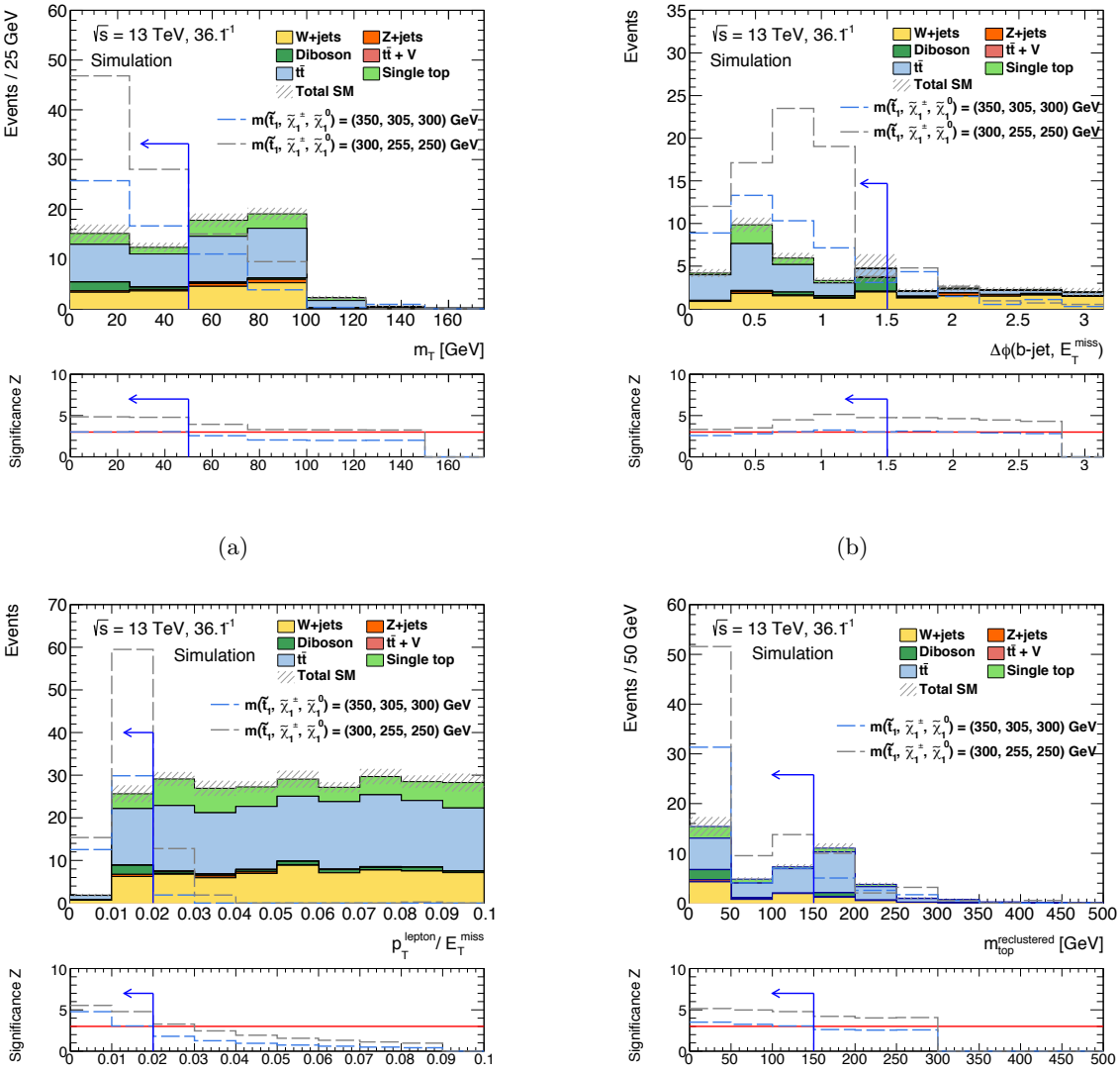

Figure 6.6: Distributions of kinematic variables after the event selection except for the requirements on the variable for which the distribution is shown for the higgsino SR optimization: (a) m_{T}, (b) $\min(\Delta\phi(\vec{p}_{\mathrm{T}}^{\,\mathrm{miss}}, b\text{-jet}))$, (c) $p_{\mathrm{T}}^{\ell}/E_{\mathrm{T}}^{\mathrm{miss}}$, and (d) $m_t^{\mathrm{reclustered}}$.

6.3 Background Estimations

After the selection, which have topologies similar to the signal, remain in this SR. The background events in SR should be precisely estimated. A semi-data driven method called control region (CR) technique is used for the estimation of some backgrounds. The fake lepton background originating from the QCD/multi-jets processes possibly affects SR. The effect of this background was estimated with fully data-driven method called "fake factor method". Other minor backgrounds such as the dilepton, single-top, Z + jets, and $t\bar{t}$+V have small contribution and are estimated by using MC simulation.

6.3.1 Semi-Data Driven Method

The semi-data driven method uses the CRs in which background events are dominant. The background events in SR in the MC sample are corrected by the number of events in CR in the data sample. The background predictions in SR called "normalized background predictions" are estimated with MC samples scaled using the "normalization factors" (μ_p) which are computed with the fit in the corresponding CRs. The relation between the normalized background predictions and normalization factors are defined as:

$$N_p(\mathrm{SR}) = \frac{N_p(\mathrm{CR},\ \mathrm{data})}{\mathrm{N}_p(\mathrm{CR},\ \mathrm{MC})} \times \mathrm{N}_p(\mathrm{SR},\ \mathrm{MC}) = \mu_p \times \mathrm{N}_p(\mathrm{SR},\ \mathrm{MC}) \tag{6.2}$$

where the $N_p(\mathrm{SR})$ is the number of events of normalized background predictions and $\mathrm{N}_p(\mathrm{CR},\ \mathrm{MC})$ and $\mathrm{N}_p(\mathrm{SR},\ \mathrm{MC})$ are the numbers of MC events in CR and SR, respectively. The total uncertainty for the backgrounds in the SR is a combination of the statistical uncertainties in the CRs and the residual systematic uncertainties for extrapolation. The CRs are designed with the following requirements to reduce the extrapolation uncertainties to the SR:

- high purity for one type of dominant background,
- free of signal contamination,
- looser selection than signal region.

In this analysis, the main backgrounds are $t\bar{t}$ and $W+$jets. The definitions of the CR for the $t\bar{t}$ background (TCR) and the CR for the $W+$jets background (WCR) are summarized in Table 6.3. For validations of the estimation, the validation region (VR) is defined as shown in Table 6.3.

Table 6.3: Overview of the event selections for SR, CRs, and VRs. Square brackets are used to show a range of the requirement.

Cut Variables	SR	TCR	TVR	WCR	WVR
Number of b-tagged jets	≥ 1	≥ 1	≥ 1	$= 1$	$= 1$
m_{T} [GeV]	< 50	< 160	< 160	< 160	< 160
$\min(\Delta\phi(\vec{p}_{\mathrm{T}}^{\mathrm{miss}}, b\text{-jet}))$	< 1.5	< 1.5	< 1.5	> 1.5	> 1.5
$p_{\mathrm{T}}^{\ell}/E_{\mathrm{T}}^{\mathrm{miss}}$	< 0.02	[0.03,0.1]	< 0.03	[0.03,0.1]	< 0.03
$m_t^{\mathrm{reclustered}}$ [GeV]	< 150	> 150	> 150	< 150	< 150

6.3.2 QCD/Multi-Jets Estimation

The lepton p_{T} of the higgsino SR is relatively low. A low momentum particle in the QCD/multi-jets events can be misidentified as a lepton. It is important to estimate the QCD/multi-jets effect. A data-driven method called "fake factor method" is used for the estimation.

Two types of lepton selection criteria are used in this method. They are defined as "ID lepton" and "Anti-ID lepton" described in Table 6.4. The ID lepton is required to pass the tight identification criterion, which is the same as that used for "signal lepton". On the other hand, Anti-ID lepton is required to mass the loose identification criterion, which is the same as that used for "baseline lepton", and is required not to pass the "signal lepton" criterion. The Anti-ID lepton includes more fake leptons. The QCD/multi-jets event in SR is estimated by the following three steps: 1) fake factor measurement, 2) QCD CR measurement, and 3) QCD/multi-jets estimation.

Table 6.4: Definition of ID and Anti-ID leptons

ID electron (identical to signal e)	ID muon (identical to signal μ)
$p_{\mathrm{T}} > 5$ GeV	$p_{\mathrm{T}} > 24$ GeV
$\lvert\eta\rvert < 2.47$, included crack region ($1.37 < \lvert\eta\rvert < 1.52$)	$\lvert\eta\rvert < 2.7$
TightLLH	Tight
$\lvert z_0 \sin\theta\rvert < 0.5$ mm, $\lvert d_0/\sigma_{d_0}\rvert < 5$	$\lvert z_0 \sin\theta\rvert < 0.5$ mm, $\lvert d_0/\sigma_{d_0}\rvert < 3$
FixedCutTight Isolation	FixedCutTightTrackOnly Isolation
Anti-ID electron (almost identical to baseline e)	**Anti-ID muon (almost identical to baseline μ)**
$p_{\mathrm{T}} > 5$ GeV	$p_{\mathrm{T}} > 4$ GeV
$\lvert\eta\rvert < 2.47$, included crack region ($1.37 < \lvert\eta\rvert < 1.52$)	$\lvert\eta\rvert < 2.7$
LooseAndBLayerLLH	Medium
No isolation	No isolation
fail one of ID electron criteria	fail one of ID muon criteria

1) Fake Factor Measurement

The fake factor (F) is defined as:

$$F_{\mathrm{lepton}} = \frac{N_{\mathrm{ID}}^{\mathrm{lepton}}}{N_{\mathrm{Anti-ID}}^{\mathrm{lepton}}} \ (\mathrm{lepton} = e \text{ or } \mu), \tag{6.3}$$

where the nominator is the number of ID lepton ($N_{\mathrm{ID}}^{\mathrm{lepton}}$) and the denominator is the number of Anti-ID lepton ($N_{\mathrm{Anti-ID}}^{\mathrm{lepton}}$). It is measured in a low $E_{\mathrm{T}}^{\mathrm{miss}}$ region, where the QCD/multi-jets event is enhanced. The jet enriched data samples triggered by several pre-scaled single leptons instead of the $E_{\mathrm{T}}^{\mathrm{miss}}$ trigger are used. The fake factor depends on the lepton p_{T} and it is calculated independently in five bins of the lepton p_{T}. Table 6.5 shows the relation between the bin of lepton p_{T} and pre-scaled triggers. Since the pre-scale values are independent and the integrated luminosity is different for each pre-scaled trigger, the data and MC samples are normalized with an arbitrary luminosity, that is 10 pb^{-1} in this analysis.

Table 6.5: The relation between pre-scaled single electron and muon triggers and the bin of lepton p_{T}. "lhvloose" means that the likelihood selection for a trigger selection is loose and the backgrounds are enriched in the data. "L1EM" indicates the L1 trigger for electromagnetic objects, with the following number showing the threshold in a unit of GeV. The character "mu" indicates the muon trigger with the follwing number showing the threshold in a unit of GeV.

Pre-scaled electron trigger	scaled luminosity [nb^{-1}]	lepton p_{T} region [GeV]
e5_lhvloose	259	[0, 5], [5, 10]
e10_lhvloose_L1EM7	692	[10, 15]
e15_lhvloose_L1EM13VH	14243	[15, 20]
e20_lhvloose	27061	[20, 100]
Pre-scaled muon trigger	**scaled luminosity [nb^{-1}]**	**lepton p_{T} region [GeV]**
mu4	758	[0, 5], [5, 10]
mu10	8017	[10, 15]
mu14	38802	[15, 20]
mu18	75412	[20, 100]

In the high m_{T} region, the real-lepton backgrounds arising from the $t\bar{t}$ and $W+$jets processes are dominant instead of fake lepton background. Therefore, the fake factor CR and fake factor SR are defined as in Figure 6.7.

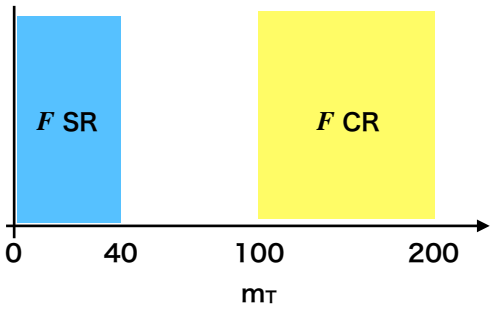

Figure 6.7: Definition of the fake factor SR ($m_{\mathrm{T}} < 40$ GeV) and CR (100 GeV $< m_{\mathrm{T}} <$ 200 GeV).

The normalization factor is measured with the m_{T} distribution in the fake factor CR, and the real-lepton backgrounds are estimated by applying this factor to the number of events in the fake factor SR. Table 6.6 shows the result for the normalization factors.

Table 6.6: Normalization factors calculated in the fake factor CR.

Normalization factor	Anti-ID lepton	ID lepton
$\mathrm{NF_{el}}$	2.87 ± 0.28	1.51 ± 0.1
$\mathrm{NF_{mu}}$	1.54 ± 0.18	1.11 ± 0.06

Since almost all lepton candidates which pass Anti-ID lepton criterion are not real-leptons, the difference between data and MC is larger than the ID lepton events. Figures 6.8 and 6.9 show the $E_{\mathrm{T}}^{\mathrm{miss}}$ and m_{T} distributions with the normalization factors applied. Data in high m_{T} region is consistent to MC applied normalization factors. The data of $E_{\mathrm{T}}^{\mathrm{miss}}$ distributions are rough because the statistic of data taken by pre-scaled triggers is very low.

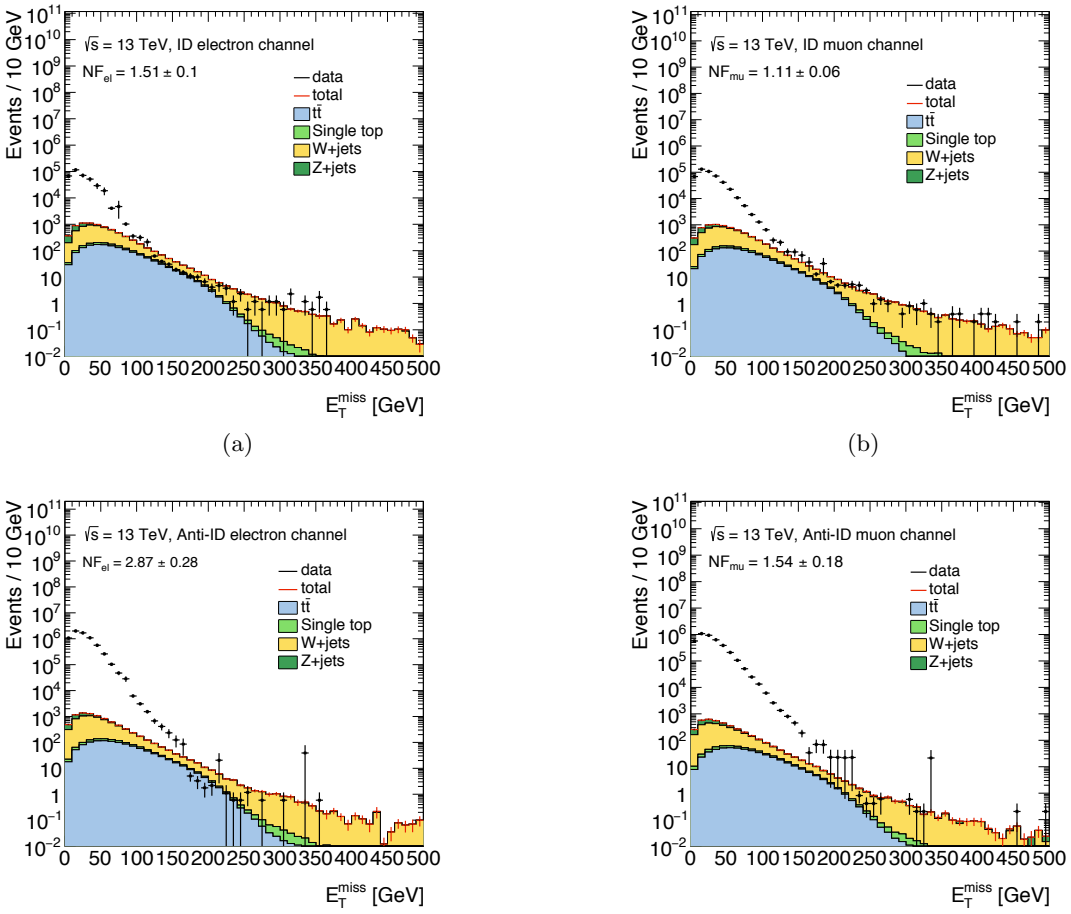

Figure 6.8: $E_{\mathrm{T}}^{\mathrm{miss}}$ distributions for (a) ID electron, (b) ID muon, (c) Anti-ID electron, and (d) Anti-ID muon. All distributions are obtained by applying the normalization factors.

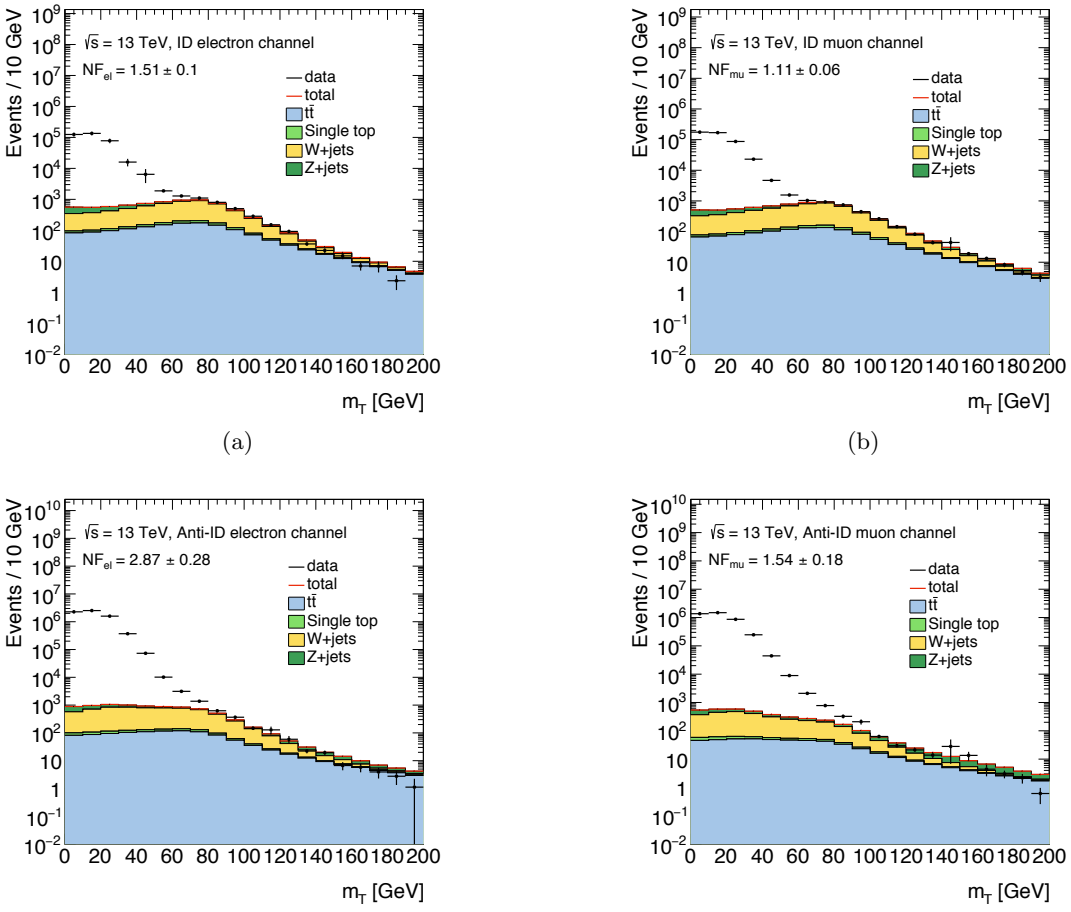

Figure 6.9: m_{T} distributions for (a) ID electron, (b) ID muon, (c) Anti-ID electron, and (d) Anti-ID muon. All distributions are obtained by applying the normalization factors.

Figures 6.10 show the lepton p_{T} distributions of ID and Anti-ID leptons. The fake factors are computed by taking the ratio of the number of ID leptons to the number of Anti-ID leptons as a function of p_{T}. The real lepton contamination is subtracted when measuring the fake factor.

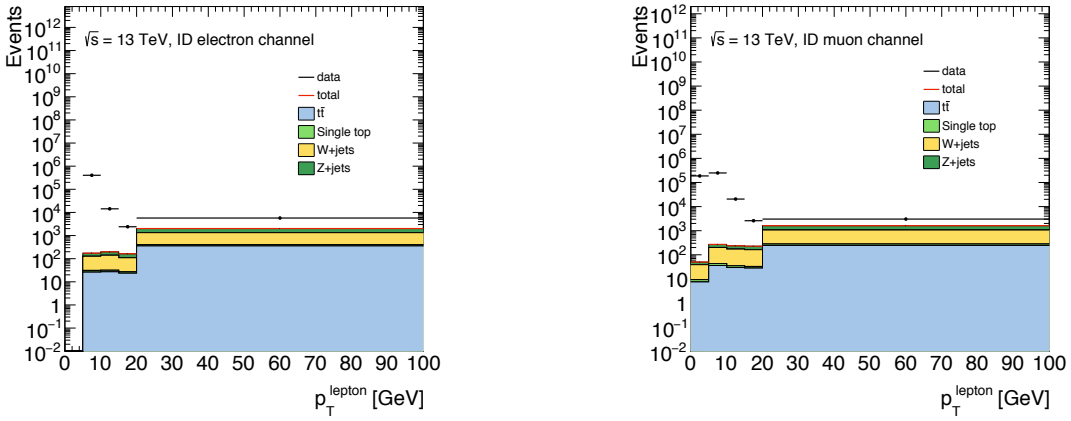

(a)

(b)

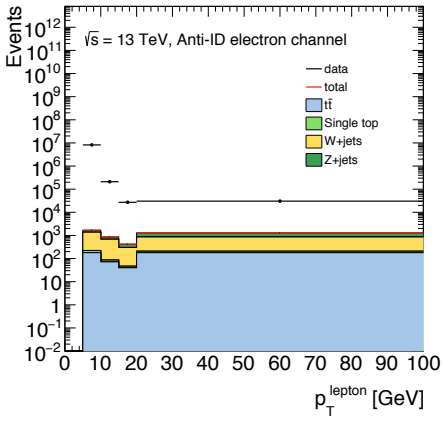

(c)

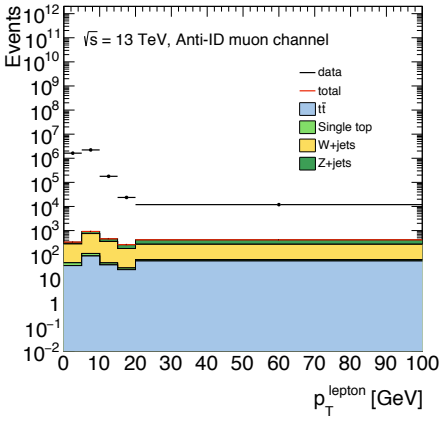

(d)

Figure 6.10: Lepton p_{T} distributions of (a) ID electron, (b) ID muon, (c) Anti-ID electron and (d) Anti-ID muon in the fake factor SR ($m_{\mathrm{T}} < 40$ GeV).

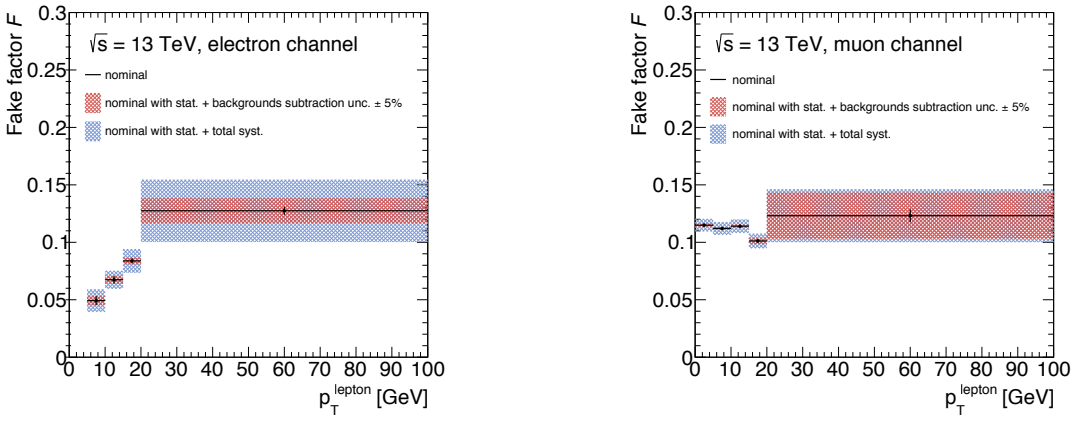

(a) (b)

Figure 6.11: Fake factor distributions for (a) electron and (b) muon. The red hatched region indicates the statistical uncertainty plus background subtraction uncertainty (±5%). The blue hatched region indicates the total uncertainty including the uncertainty shown by red hatched region plus the sample composition uncertainty.

The results of fake factor are shown in Figures 6.11. Backgrounds may not be estimated correctly due to some effects: pre-scaled trigger effect, insufficient backgrounds statistics, etc. The systematic uncertainty is the maximum difference between fake factors when the total number of ID and Anti-ID backgrounds are changed by ±5% as shown in Figures 6.12.

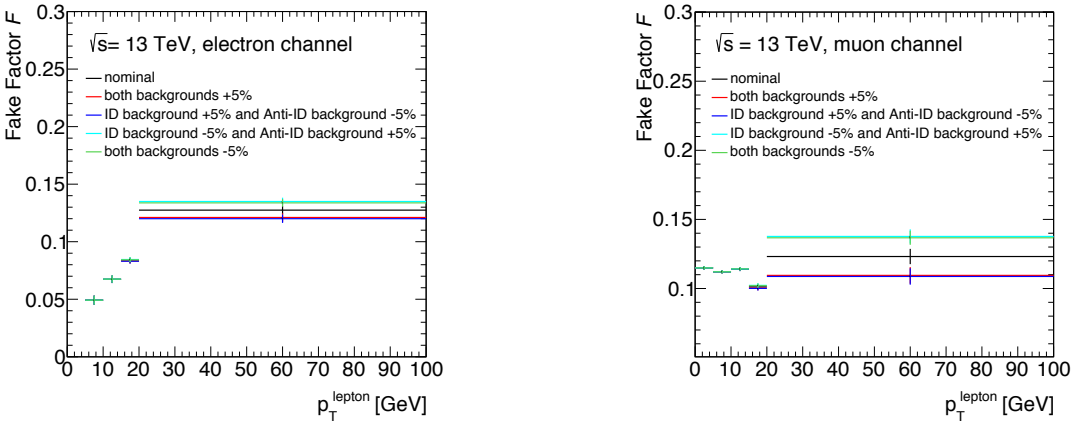

(a) (b)

Figure 6.12: Fake factor distributions for (a) electron and (b) muon with different background subtractions.

The systematic uncertainty due to the difference of the fake lepton composition between SR and a region where the fake factor is measured. Figure 6.13 shows this uncertainty. The p_{T} of the away-side jet is varied by changing the composition. The total uncertainty of fake lepton is around 30%.

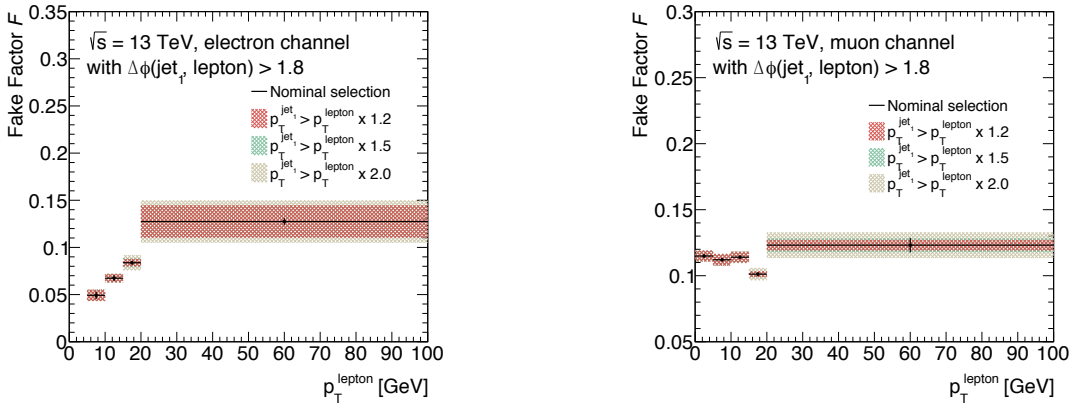

(a) (b)

Figure 6.13: Fake factor distributions for (a) electron and (b) muon with different background subtractions.

2) QCD/Multi-Jets CR Measurement

QCD/multi-jets CR is defined by the same requirements as those for SR except for Anti-ID lepton criteria instead of ID lepton criteria. In this sample, the Anti-ID leptons are treated with the same way as the ID leptons in the SR, for example in the $E_{\mathrm{T}}^{\mathrm{miss}}$ calculation and the overlap removal. The number of QCD CR events ($N_{\mathrm{QCR}}^{\mathrm{QCD}}$) affected by only QCD/multi-jets is defined as:

$$N_{\mathrm{QCR}}^{\mathrm{QCD}} = N_{\mathrm{QCR}} - N_{\mathrm{QCD}}^{\mathrm{non-QCD}}. \tag{6.4}$$

It is estimated by subtracting SM backgrounds ($N_{\mathrm{QCD}}^{\mathrm{non-QCD}}$) from the total number of events in QCD CR (N_{QCR}). Since the usual lepton scale factors are not appropriate due to the use of Anti-ID lepton criteria, the normalization of the SM backgrounds is not trivial. Therefore, the dedicated normalization factors need to be applied. The normalization factors are calculated in the soft-lepton preselection described in Table 6.7.

Table 6.7: Soft-lepton preselection for the normalization factor calculation.

Selection	Comments
$E_{\mathrm{T}}^{\mathrm{miss}}$ triggers	
jet cleaning	veto events that contain a jet that fails the loose jet cleaning criteria
exactly one soft lepton	$p_{\mathrm{T}} > 4(5)$ GeV for muon(electron), no additional baseline leptons
	$p_{\mathrm{T}} < 25$ GeV for data/MC plots (no cut for the higgsino SR)
≥ 2 signal jets	
≥ 1 b-jet	
Leading and second jet $p_{\mathrm{T}} > 25$ GeV	
$E_{\mathrm{T}}^{\mathrm{miss}} > 230$ GeV	start of the $E_{\mathrm{T}}^{\mathrm{miss}}$ trigger plateau
$\lvert\Delta\phi(j_{1,2}, \vec{p}_{\mathrm{T}}^{\mathrm{miss}})\rvert > 0.4$	control of QCD/multi-jet backgrounds

To reduce the QCD/multi-jets effect and to increase the SM backgrounds effect, the $E_{\mathrm{T}}^{\mathrm{miss}}$ and m_{T} selections are varied. The results are shown in Figure 6.14.

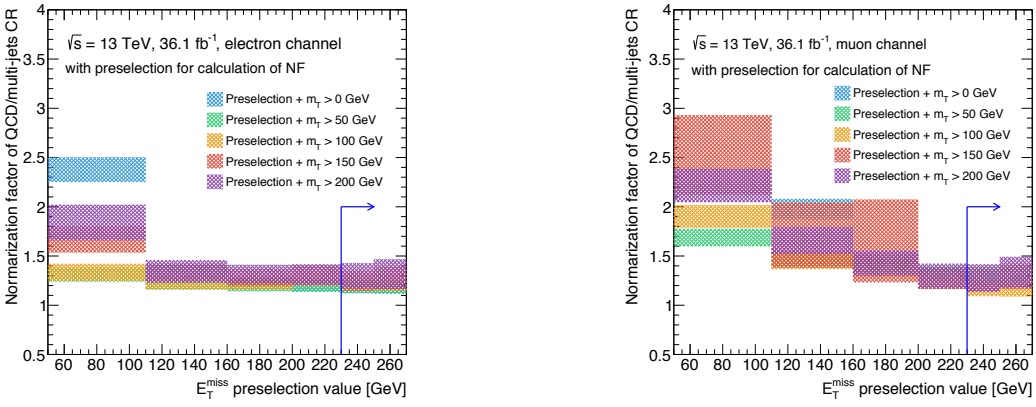

(a) (b)

Figure 6.14: Normalization factors for (a) electron and (b) muon with various selections.

The normalization factors are saturated in high $E_{\mathrm{T}}^{\mathrm{miss}}$ and m_{T} region, and the requirement on $E_{\mathrm{T}}^{\mathrm{miss}}$ is 230 GeV and the requirement on m_{T} is 100 GeV. The normalization factor for election is 1.23 $\pm$ 0.07 and the

normalization factor for muon is 1.18 ± 0.06. The backgrounds composition uncertainty is included in these errors.

Figure 6.15 shows $E_{\mathrm{T}}^{\mathrm{miss}}$ and m_{T} distributions in QCD CR with the selection shown in Table 6.7 replacing $E_{\mathrm{T}}^{\mathrm{miss}} > 230$ GeV by $E_{\mathrm{T}}^{\mathrm{miss}} > 50$ GeV. There is a large difference between data and SM backgrounds in low $E_{\mathrm{T}}^{\mathrm{miss}}$ and m_{T} regions due to the QCD/multi-jets background. On the other hand, there is no significant difference in high $E_{\mathrm{T}}^{\mathrm{miss}}$ and m_{T} regions, and the data is consistent with SM background except for QCD/multi-jets. The effect of QCD/multi-jets is smaller in high momentum regions.

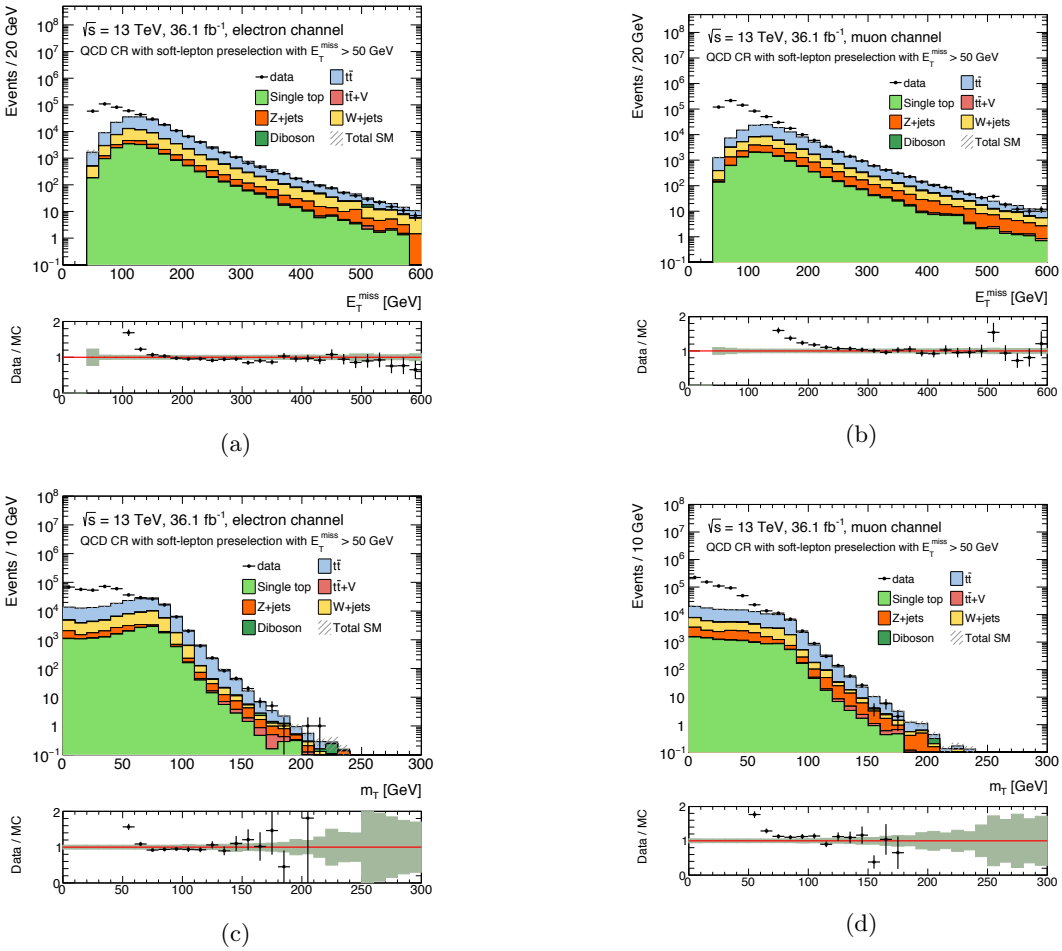

Figure 6.15: $E_{\mathrm{T}}^{\mathrm{miss}}$ distributions in the fake lepton CR for (a) electron channel and (b) muon channel, and m_{T} distributions in the fake lepton CR for (c) electron channel and (d) muon channel.

3) QCD/Multi-Jets Estimation

The QCD/multi-jets background in the SR ($N_{\mathrm{SR}}^{\mathrm{QCD}}$) is estimated by multiplying the fake factor to $N_{\mathrm{QCR}}^{\mathrm{QCD}}$:

$$N_{\mathrm{SR,lepton}}^{\mathrm{QCD}} = N_{\mathrm{QCR,lepton}}^{QCD} \times F_{lepton} \text{ (lepton} = e \text{ or } \mu). \tag{6.5}$$

The QCD/multi-jets estimation is validated with the selection summarized in Table 6.7. Figure 6.16 shows the $E_{\mathrm{T}}^{\mathrm{miss}}$ distributions and m_{T} distributions with $E_{\mathrm{T}}^{\mathrm{miss}} > 50$ GeV instead of $E_{\mathrm{T}}^{\mathrm{miss}} > 230$ GeV for both lepton channels. Figure 6.17 shows the lepton p_{T} distributions with the same selection. The QCD/multi-jets are well predicted in both of electron and muon channels. The QCD/multi-jets background are estimated for the higgsino SR is summarized in Table 6.8.

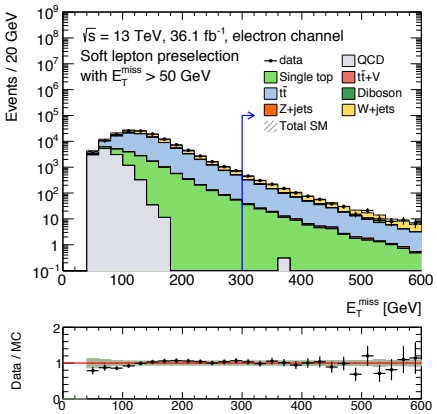

(a)

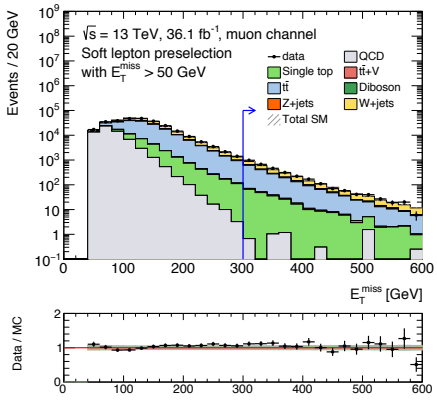

(b)

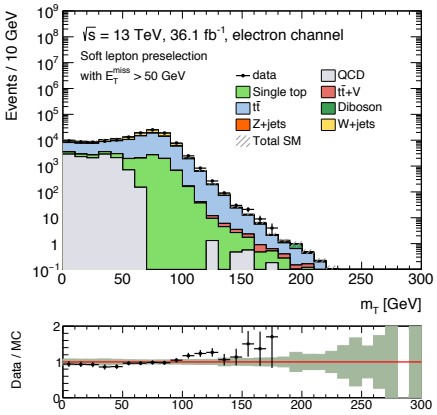

(c)

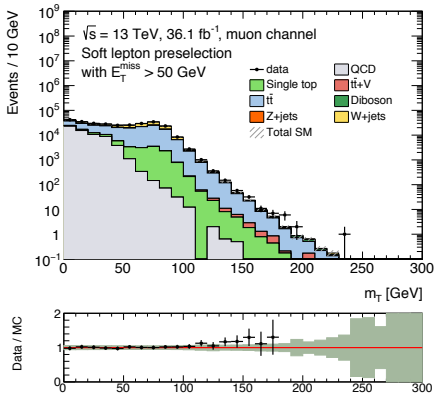

(d)

Figure 6.16: $E_{\mathrm{T}}^{\mathrm{miss}}$ distributions in the SR with $E_{\mathrm{T}}^{\mathrm{miss}} > 50$ GeV selection for (a) electron and (b) muon, and m_{T} distributions in the SR with $E_{\mathrm{T}}^{\mathrm{miss}} > 50$ GeV selection for (c) electron and (d) muon.

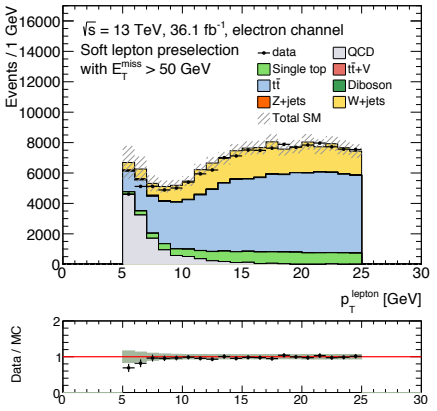

(a)

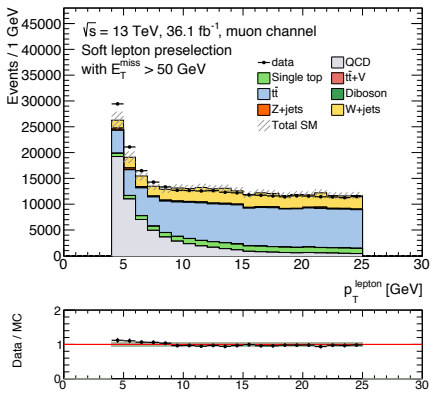

(b)

Figure 6.17: Lepton p_{T} distributions in the SR with $E_{\mathrm{T}}^{\mathrm{miss}} > 50$ GeV selection for (a) electron channel and (b) muon channel.

Table 6.8: Result of the QCD/multi-jets estimation for the higgsino SR.

Signal region	Total SM (before normalization)	QCD/multi-jets
higgsino SR	27.50 ± 4.28	2.45 ± 0.13
		e = 0.42 ± 0.10
		μ = 2.03 ± 0.09

The statistical and systematic uncertainties of SM backgrounds except for QCD/multi-jets background described in Section 6.5 is around 5. The QCD/multi-jets background is relatively small, and neglected in this analysis.

6.4 Systematic Uncertainties

In order to quantify the evidence of new physics with small statistics from the comparison between data and MC, the statistical significance is needed to certify with the all systematics. This section discusses the statistical analysis for this analysis and all systematic uncertainties considered in this analysis.

6.4.1 Systematic Uncertainties

The systematic uncertainties impact on the signal and background estimations. The main components are experimental uncertainties and theoretical uncertainties. These systematic uncertainties are included as nuisance parameters with Gaussian constraints ($\boldsymbol{\theta}$) and these parameters are profiled in the likelihood fit.

There are two types of uncertainties. The one affects the extrapolation from the CRs into the SRs. The uncertainties with this type are implemented as the uncertainties on the transfer factor (TF):

$$\mathrm{TF} = \frac{\text{Number of MC events in SR (VR)}}{\text{Number of MC events in CR}}. \tag{6.6}$$

The other one affects the overall normalization of the MC samples. They are not cancelled out at the extrapolation.

The nuisance parameters are determined with optimal values simultaneously when the profiled likelihood ratio is fitted. In order to improve the fit stability and the fast execution of the fit, the uncertainties with small values, which do not greatly impact on the fit result, are removed from the fit.

Experimental Uncertainties

The experimental uncertainties are generated mainly from the ones related to detectors that include the effects of object reconstruction, identification, and energy/momentum measurement. It does not only includes object-based uncertainties, but also the uncertainties corresponding to LHC, e.g. integrated luminosity, pile-up, etc. The dominant uncertainties of the experimental uncertainties are shown below.

- **Jet uncertainties**
  The imperfect knowledge of Jet Energy Scale (JES) and Jet Energy Resolution (JER) [122] become the dominant experimental uncertainties. There are parametrised by 74 independent JES uncertainties modeled from each calibration step. Fortunately, several uncertainties with similar behavior can be combined, and thus the total JES uncertainties can be reduced to 3 independent uncertainties. All JER uncertainties are similar behavior and they can be combined. Thus the only one JER uncertainty is used for this

analysis. Figures 6.18 show the measured uncertainties on JES and JER with the breakdown of each source. The resulting uncertainties expressed as relative uncertainties on the total predicted background yield in the SRs are in the range 1.4 - 7% for JES and 1.5 - 7% for JER, respectively. In addition, the modelling of the b-tagging efficiencies and mistag rates also become one of the systematic uncertainties. The uncertainty is evaluated by varying training samples used by the MV2 algorithm, and the resultant uncertainty is typically in a range of 1.6 - 13%.

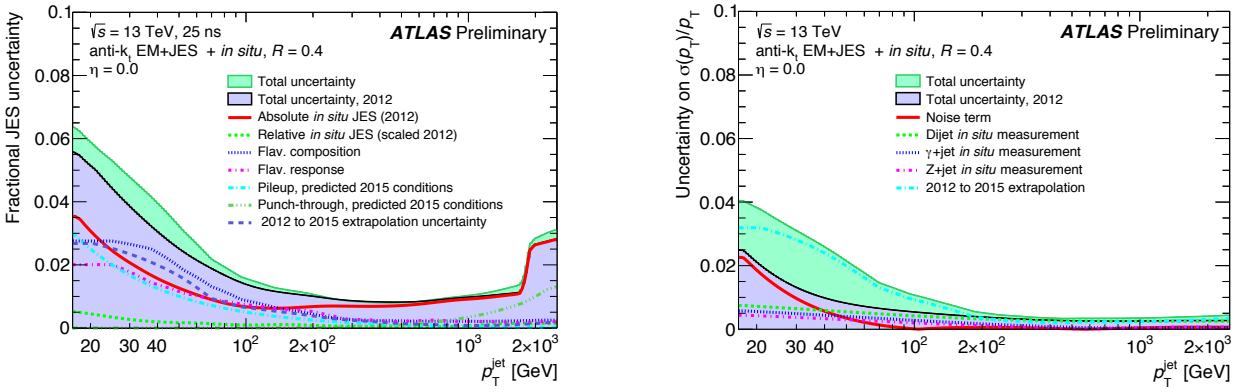

(a) (b)

Figure 6.18: Measured uncertainties in (a) JES and (b) JER with the breakdown of each source [122].

- $E_{\mathrm{T}}^{\mathrm{miss}}$ **uncertainties**
  The effects of the uncertainties for lepton/jet energy scale and resolution are propagated to the $E_{\mathrm{T}}^{\mathrm{miss}}$ calculation and so the $E_{\mathrm{T}}^{\mathrm{miss}}$ uncertainties are also taken into account in this analysis. These uncertainties correspond to the scale and resolution similar to the jets uncertainties.

- **Pile-up reweighting uncertainty**
  The uncertainty corresponding to the pile-up reweighting is also included in this analysis.

- **Liminosity uncertainty**
  The uncertainty for integrated luminosity is measured by using the LUCID detector [123]. The total uncertainty is about 3.7%.

- **Lepton uncertainties**
  All of the uncertainties for the lepton identifications and energy scales/resolutions are evaluated. In case of electrons, there are three efficiency uncertainties corresponding to the identification, energy scale, and energy resolution. They are evaluated based on the discrepancy between simulated and observed response of the EM calorimeter in Run-2. On the other hand, the muon has two type of uncertainties corresponding to the ID measurement and MS measurement. These uncertainties also include the uncertainties of the identification and energy scale/resolution.

Theoretical Uncertainties

The theoretical uncertainties mainly correspond to the calculation of MC simulation.

The source of Theoretical Uncertainties

- **Renormarisation and factorisation scales**
  The renormalization and factorisation scales ($\mu_{\text{renom.}}, \mu_{\text{fact.}}$), which are used for calculation MC simulations, are not physical theory parameters, but they impact on observables when fixed-high order calculation for the perturbation theory is implemented. Therefore, these contaminations should be considered as the theoretical uncertainties. There uncertainties are estimated by comparing different samples with the different scale values by a factor of 0.5 to 2.

- **Interference**
  This uncertainty is only for single-top background. The single-top background MC samples are calculated NLO-level, which has the $W\top \rightarrow WWbb$ process and it is overlapped with the $t\bar{t}$ background. This overlap is removed by comparing the single-top and $t\bar{t}$ background MC samples and is calculated as the interference uncertainty.

- **The other uncertainties**
  Typically, the other theoretical uncertainties corresponding to the modeling of ME generator, parton showers, fragmentation/hadronisation are calculated by using different MC samples with different modelings. These calculations are different for each background, and the details are described in Section 6.4.1.

The amounts of Theoretical Uncertainties

The uncertainties in the modelling of $t\bar{t}$ and single-top backgrounds include separately effects of hard-scattering, fragmentation, radiation and interference. The amount of ISR/FSR is also considered. The MC generator uncertainty is evaluated by comparing events produced with POWHEG-Box+Herwig++ v2.7.1 with those either MG5_aMC@NLO v2.2.3+Herwig++ v2.7.1 (NLO) or SHERPA v2.2. To estimate the effects of fragmentation and hadronisation, the events generated with POWHEG-Box are hadronised with either PYTHIA6 or Herwig++. The effect of the amount of ISR/FSR is estimated by using the POWHEG-Box+PYTHIA6 samples with defferent parton shower radiation, NLO radiation, and the fragmentation/hadronisation scales. The interference uncertainty is calculated by comparing the sum of $t\bar{t}$ and single-top backgrounds that are generated by MG5_aMC@NLO v2.2.3. The resulting uncertainties from all sources on the CR to SR extrapolation factors are 10-45% for $t\bar{t}$, and 10-47% for single-top, and the interference term dominates the latter uncertainty.

The uncertainty in the modelling of W + jets background includes the effect of the modeling. It is estimated by comparing the different ME generators: SHERPA, MG5_aMC@NLO v2.2.3+Pythia8 (NLO). In addition, the effect of varying the scales for the matching scheme for matrix element, parton shower, etc, are also estimated. The total modeling uncertainty is around 13-32%.

The diboson uncertainties are also considered and they are estimated by varying the renormarisation, factorisation, and resummation scales. The theoretical uncertainties range from 13 to 32%.

For the SUSY signal uncertainty, the cross-section uncertainty is taken into account from the envelope of the cross-section predictions using the difference PDF sets and factorisations/renormarisation scales [78]. The resulting uncertainties range from 13 to 23%.

6.5 Results

In this section, the unblinded result for the higgsino LSP scenario is presented. After introducing the likelihood fit, the result of the background-only fit is shown, which provides the estimation of backgrounds with the impact of the systematic uncertainty, and the results of the comparison between the observed data yields and the predicted SM background yields in CRs and VRs are shown. Finally, the final comparison between the observed data and the background yields in SR and this interpretation on SUSY signal models are shown.

6.5.1 Likelihood for the statistical analysis

The full likelihood function for SR and CRs in this analysis can be defined as

$$\begin{aligned} L(n|\mu, \boldsymbol{b}, \boldsymbol{\theta}) &= P_{\mathrm{SR}} \times P_{\mathrm{CR}} \times C_{\mathrm{syst}} \\ &= P(n_{SR}|E_{SR}(\mu, \boldsymbol{b}, \boldsymbol{\theta})) \times \\ &\quad P(n_{\mathrm{TCR}}|E_{\mathrm{TCR}}(\mu, \boldsymbol{b}, \boldsymbol{\theta})) \times P(n_{\mathrm{WCR}}|E_{\mathrm{WCR}}(\mu, \boldsymbol{b}, \boldsymbol{\theta})) \cdot C_{\mathrm{nuis}}(\boldsymbol{\theta}). \end{aligned} \tag{6.7}$$

Here, E_{SR}, E_{TCR}, and E_{WCR} are the expectation value for each region, and $C_{\mathrm{nuis.}}$ is the function of nuisance parameters. The probabilities P of SR and CRs are defined as the Possion distribution function. The details of the profile likelihood can be found in Appendix A.

6.5.2 The Result of the Background-only Fit

The background-only fit is performed to derive the $t\bar{t}$ and W + jets normalization factors from CRs with high purity $t\bar{t}$ or W + jets events, respectively. The both CRs are taken into account not to be contaminated by signal. Other backgrounds are included in this fit within their respective uncertainties. The $t\bar{t}$ and W + jets normalization factors are free parameters and are determined as:

$$\mu_{t\bar{t}} = 0.73 \pm 0.11, \text{and} \tag{6.8}$$

$$\mu_{W+\mathrm{jets}} = 1.12 \pm 0.25. \tag{6.9}$$

Table 6.9 shows the background yields before and after the fit and the number of observed events in all CRs and VRs. Here, the "MC exp." labels describe the nominal MC prediction before the fit, and the "Fitted" labels describe the number of MC prediction after the fit. Other minor backgrounds are fixed with the input values from these MC predictions for the fit, and they are not normalized in each CR and VR. The effect of the fit for these minor backgrounds is considered to be negligible. The observed data yield and the total number of fitted background events in each CR and VR are consistent.

Figures 6.19, 6.20, 6.21, and 6.22 show distributions of selected variables in each CR and VR. The shapes of all distributions in each CR are consistent between the data and the fitted MC predictions. In addition, the statistical fluctuation in each VR tends to become large because VRs have the tighter selections than CRs, but fortunately the shapes of the data and the fitted total MC prediction are consistent. Therefore, the $t\bar{t}$ and W + jets normalization factors are reliably validated, and they can be used for the background estimation in SR.

Table 6.10 shows systematic uncertainties in each CR and VR. These tables include only some dominant uncertainties. The most dominant uncertainty in TCR is the uncertainty coming from the $t\bar{t}$ normalization factor and it has about 11%. In case of WCR, the most dominant uncertainty is the uncertainty coming from the W + jets normalization factor and it has about 16%. In the VRs, the most dominant uncertainty in TVR is the modeling of the hard scatter for $t\bar{t}$, which is about 22%, and the most dominant uncertainty in WVR is

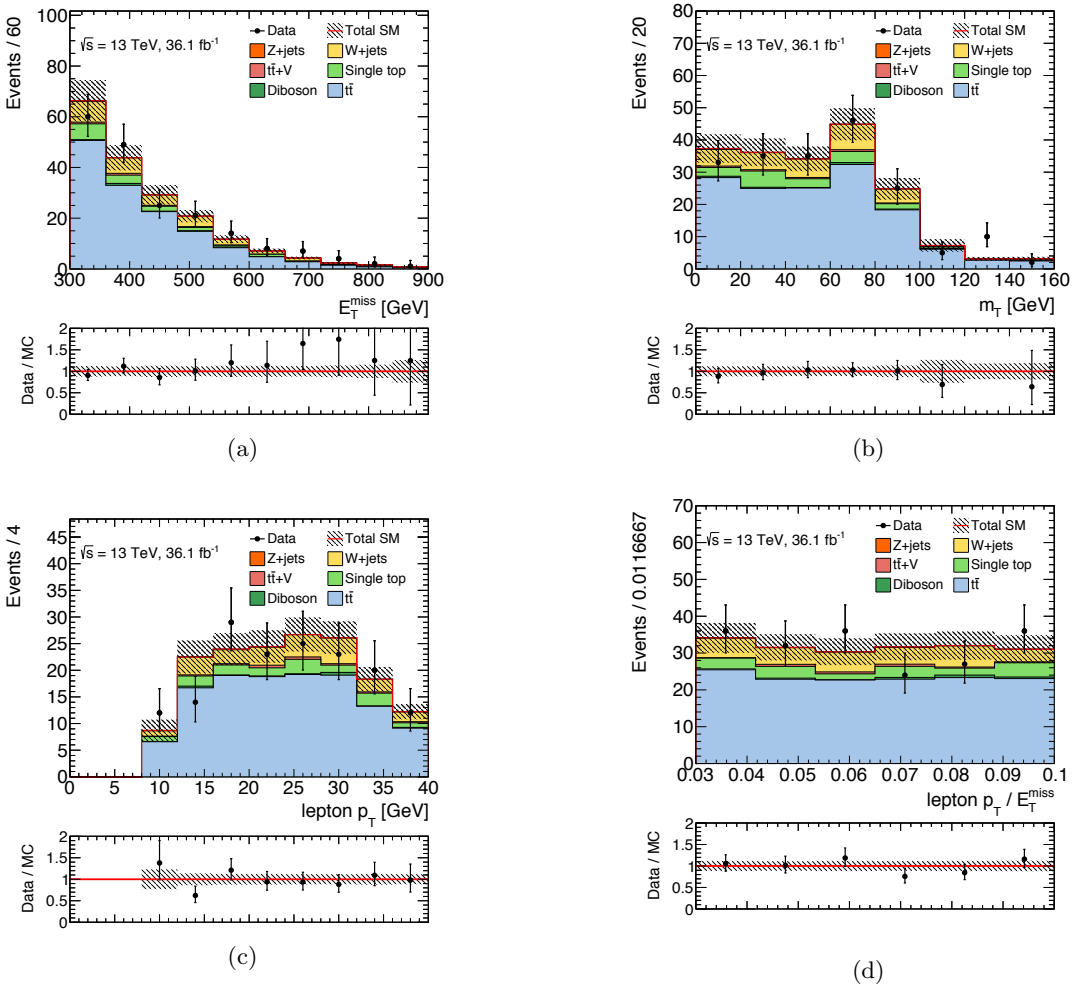

Figure 6.19: Observed distributions of selected variables in TCR: (a) $E_{\mathrm{T}}^{\mathrm{miss}}$, (b) m_{T}, (c) p_{T}^{ℓ}, and (d) $p_{\mathrm{T}}^{\ell}/E_{\mathrm{T}}^{\mathrm{miss}}$. The histograms show the MC background predictions, normalised to cross-section times integrated luminosity and the dominant process in each CR is normalised to data. The hatched red error bands indicate the combined uncertainties.

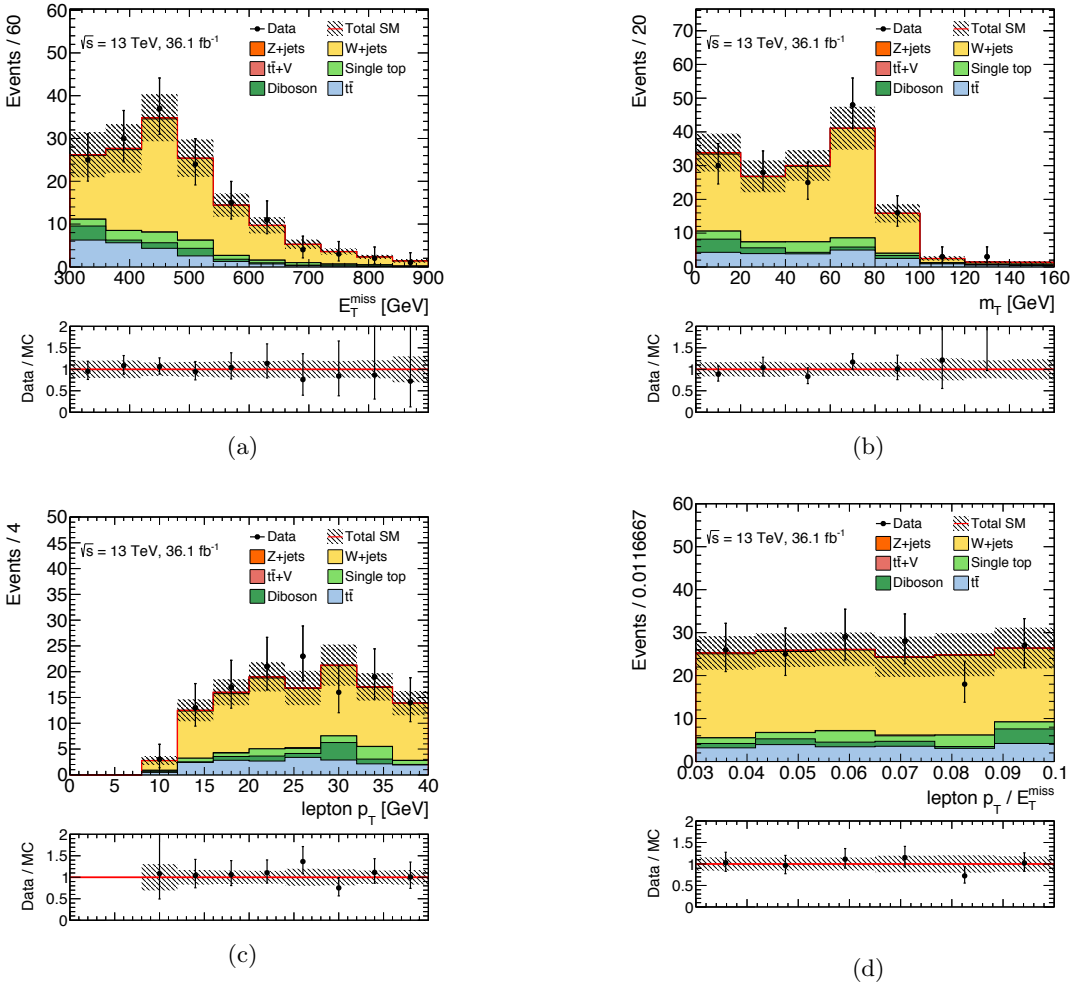

Figure 6.20: Observed distributions of selected variables in WCR: (a) $E_{\mathrm{T}}^{\mathrm{miss}}$, (b) m_{T}, (c) p_{T}^{ℓ}, (d) $p_{\mathrm{T}}^{\ell}/E_{\mathrm{T}}^{\mathrm{miss}}$. The histograms show the MC background predictions, normalised to cross-section times integrated luminosity and the dominant process in each CR is normalised to data. The hatched red error bands indicate the combined uncertainties.

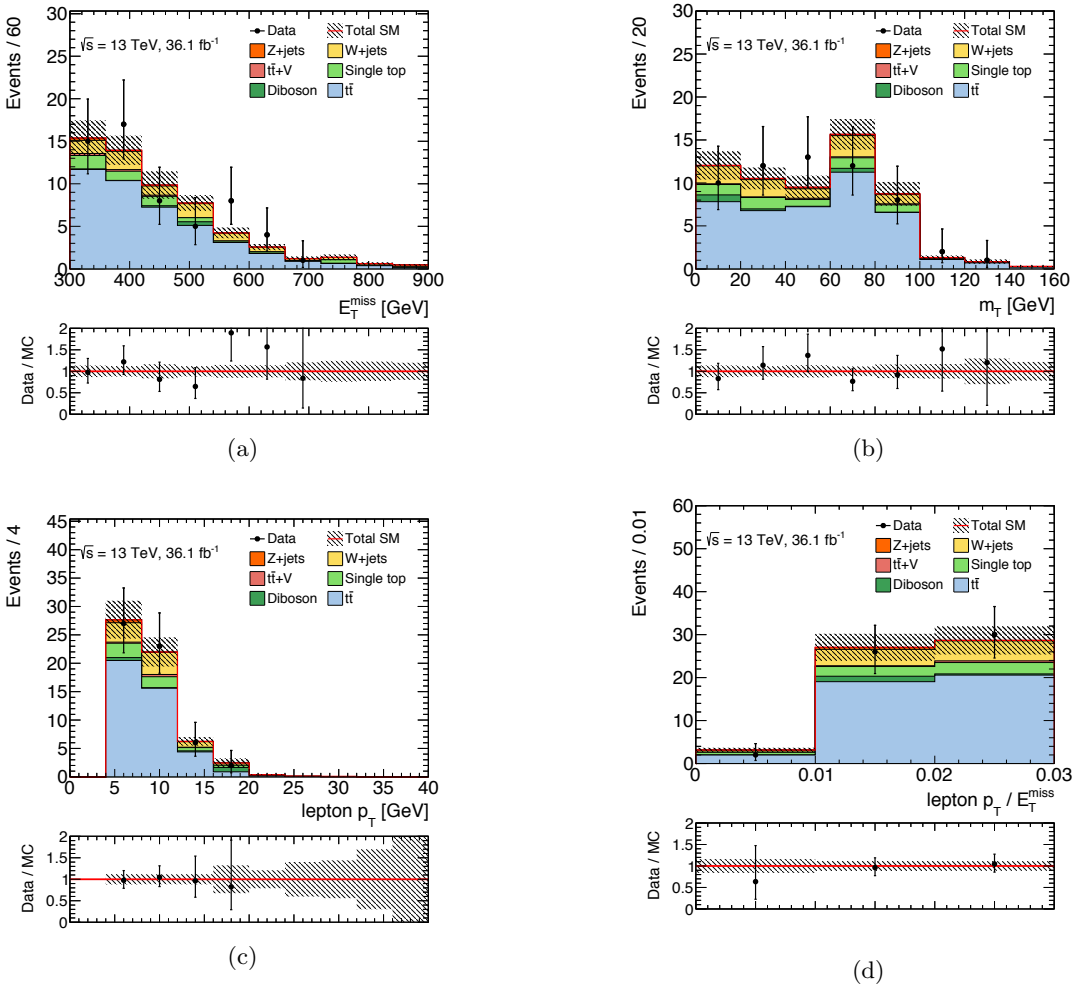

Figure 6.21: Observed distributions of selected variables in TVR: (a) $E_{\mathrm{T}}^{\mathrm{miss}}$, (b) m_{T}, (c) p_{T}^{ℓ}, (d) $p_{\mathrm{T}}^{\ell}/E_{\mathrm{T}}^{\mathrm{miss}}$. The histograms show the MC background predictions, normalised to cross-section times integrated luminosity and the dominant process in each CR is normalised to data. The hatched red error bands indicate the combined uncertainties.

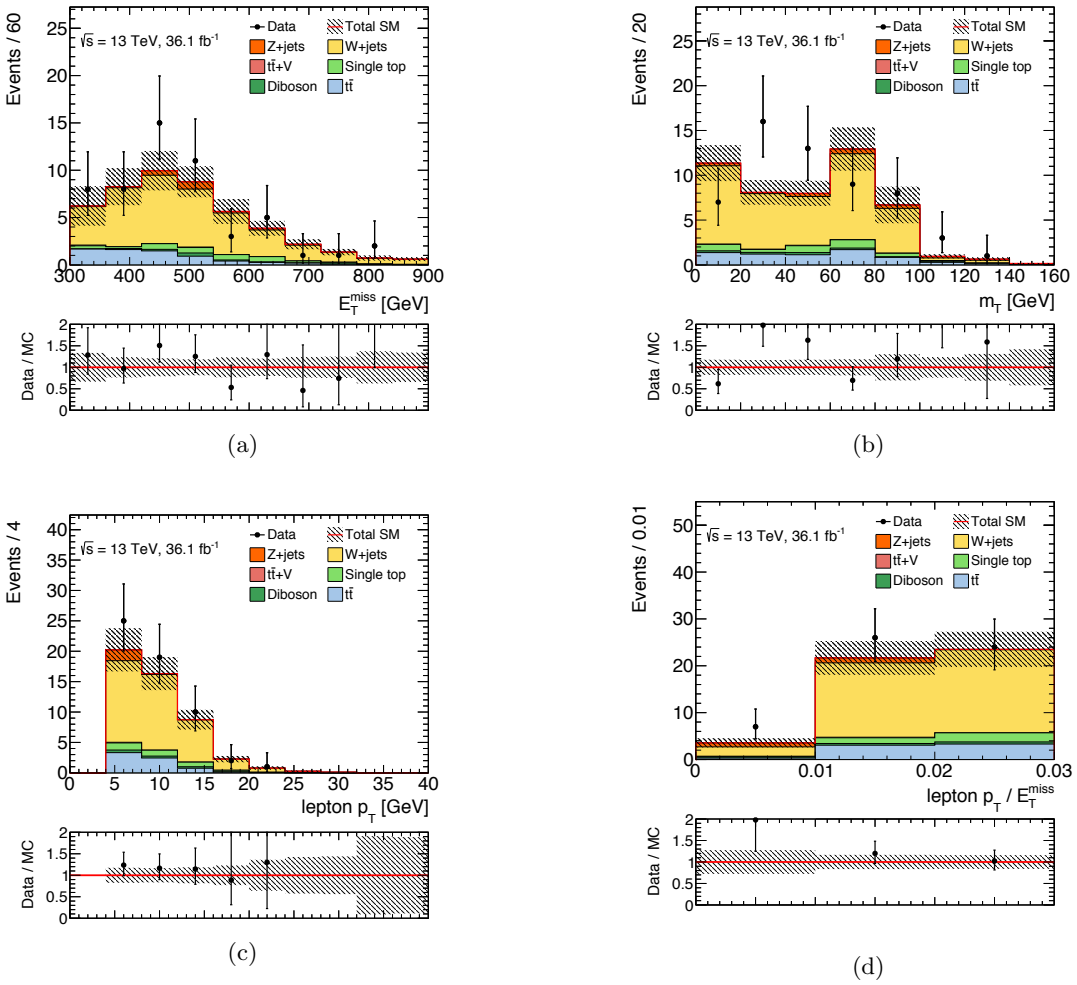

Figure 6.22: Observed distributions of selected variables in WVR: (a) $E_{\mathrm{T}}^{\mathrm{miss}}$, (b) m_{T}, (c) p_{T}^{ℓ}, (d) $p_{\mathrm{T}}^{\ell}/E_{\mathrm{T}}^{\mathrm{miss}}$. The histograms show the MC background predictions, normalised to cross-section times integrated luminosity and the dominant process in each CR is normalised to data. The hatched red error bands indicate the combined uncertainties.

Table 6.9: Background-only fit results for the TCR, WCR, TVR, and WVR. The lower part of this table shows the nominal MC expectations before the fit, and the upper part of this table shows the background expectations after the fit.

higgsino SR channel	TCR	WCR	TVR	WVR
Observed events	191	153	58	57
Fitted bkg events	190.80 ± 13.86	153.10 ± 12.37	59.05 ± 14.70	48.79 ± 6.02
Fitted powheg_ttbar events	140.32 ± 20.62	21.55 ± 14.06	41.80 ± 16.19	6.73 ± 4.92
Fitted powheg_singletop events	16.52 ± 12.91	10.97 ± 7.66	5.52 ± 4.44	3.30 ± 1.05
Fitted amcnlo_ttV events	2.35 ± 0.39	0.47 ± 0.13	0.63 ± 0.12	0.15 ± 0.05
Fitted sherpa22_Wjets events	28.93 ± 7.90	110.74 ± 20.59	8.88 ± 2.48	35.59 ± 7.41
Fitted sherpa221_diboson events	2.25 ± 0.79	8.40 ± 3.01	1.59 ± 0.53	1.05 ± 0.41
Fitted sherpa22_Zjets events	0.45 ± 0.42	0.96 ± 0.89	0.63 ± 0.58	1.97 ± 1.76
MC exp. SM events	239.61 ± 15.39	148.72 ± 22.89	73.31 ± 19.83	47.29 ± 8.08
MC exp. powheg_ttbar events	192.39 ± 5.62	29.29 ± 17.95	57.06 ± 19.16	9.14 ± 6.36
MC exp. powheg_singletop events	16.44 ± 12.96	10.96 ± 7.72	5.49 ± 4.46	3.29 ± 1.05
MC exp. amcnlo_ttV events	2.35 ± 0.40	0.47 ± 0.13	0.63 ± 0.12	0.15 ± 0.05
MC exp. sherpa22_Wjets events	25.74 ± 5.44	98.63 ± 10.85	7.90 ± 1.81	31.69 ± 4.28
MC exp. sherpa221_diboson events	2.24 ± 0.79	8.41 ± 3.03	1.59 ± 0.53	1.05 ± 0.41
MC exp. sherpa22_Zjets events	0.45 ± 0.42	0.96 ± 0.89	0.63 ± 0.58	1.96 ± 1.78

also same as TVR and it is about 9%. The amount of individual uncertainties is derived by setting all other nuisance parameters to constant without the parameter of interest and then propagating the uncertainty due to this parameter only.

Table 6.10: Breakdown of the dominant systematic uncertainties on background yield estimates in the various control regions. Note that the individual uncertainties can be correlated, and do not necessarily add up quadratically to the total background uncertainty. The percentages show the size of the uncertainty relative to the total expected background.

Uncertainty of channel	TCR	WCR
Total background expectation	190.80	153.10
Total statistical ($\sqrt{N_{\text{exp}}}$)	±13.81	±12.37
Total background systematic	±13.86 [7.26%]	±12.37 [8.08%]
$\mu_{t\bar{t}}$ normalization unc.	±21.37 [11.2%]	±3.28 [2.1%]
theory unc. on single Top	±12.47 [6.5%]	±7.52 [4.9%]
$\mu_{W+\text{jets}}$ normalization unc.	±6.39 [3.3%]	±24.46 [16.0%]
theory unc. on W+jets	±4.88 [2.6%]	±0.00 [0.00%]
jet and met	±4.18 [2.2%]	±1.90 [1.2%]
b-jet tagging	±3.44 [1.8%]	±0.79 [0.51%]
MC statistics	±2.77 [1.5%]	±4.60 [3.0%]
c- or light-jet tagging	±2.62 [1.4%]	±12.11 [7.9%]
pile-up	±1.37 [0.72%]	±1.56 [1.0%]
theory unc. on dibosons	±0.63 [0.33%]	±2.25 [1.5%]
theory unc. on Z+jets	±0.40 [0.21%]	±0.86 [0.56%]
theory unc. on $t\bar{t}$V	±0.29 [0.15%]	±0.06 [0.04%]
theory unc. on $t\bar{t}$	±0.00 [0.00%]	±12.99 [8.5%]
Uncertainty of channel	TVR	WVR
Total background expectation	59.05	48.79
Total statistical ($\sqrt{N_{\text{exp}}}$)	±7.68	±6.98
Total background systematic	±14.70 [24.89%]	±6.02 [12.34%]
theory unc. on $t\bar{t}$	±13.85 [23.4%]	±4.62 [9.5%]
$\mu_{t\bar{t}}$ normalization unc.	±6.37 [10.8%]	±1.03 [2.1%]
theory unc. on single Top	±4.41 [7.5%]	±1.01 [2.1%]
$\mu_{W+\text{jets}}$ normalization unc.	±1.96 [3.3%]	±7.86 [16.1%]
theory unc. on W+jets	±1.59 [2.7%]	±1.77 [3.6%]
MC statistics	±1.46 [2.5%]	±2.05 [4.2%]
jet and met	±1.40 [2.4%]	±1.72 [3.5%]
c- or light-jet tagging	±0.99 [1.7%]	±3.89 [8.0%]
b-jet tagging	±0.96 [1.6%]	±0.31 [0.64%]
pile-up	±0.63 [1.1%]	±0.27 [0.55%]
theory unc. on Z+jets	±0.56 [0.95%]	±1.76 [3.6%]
theory unc. on dibosons	±0.45 [0.76%]	±0.30 [0.62%]
theory unc. on $t\bar{t}$V	±0.08 [0.13%]	±0.02 [0.04%]

6.5.3 Unblinded SR

After validation, the background yields in SR are extracted by the extrapolation from CRs to SR with the $t\bar{t}$ and W + jets normalization factors. Table 6.11 shows the unblinded results of the predicted background yields and the observed event yields in SR, and only systematic uncertainties are included in this table. The total number of observed events is 33 events and the total number of the fitted background predictions is 24.59 ± 3.53. The total number of background predictions tends to be a bit smaller than the total number of observed events due to large statistical fluctuations in SR with tight selections. Table 6.12 shows the total systematic uncertainty and the breakdown. Figure 6.23 shows $E_{\mathrm{T}}^{\mathrm{miss}}$, m_{T}, lepton p_{T}, and $p_{\mathrm{T}}^{\ell}/E_{\mathrm{T}}^{\mathrm{miss}}$ distributions in SR, and the benchmark signal distributions are also included in these figures. The shapes of observed events in all distributions are basically the same as the shapes of the total background predictions. In addition, these shapes and the ones including the signal plus backgrounds are consistent. Therefore, no significant excess above the SM prediction is found from this unblinded result.

Table 6.11: Unblinded results of the predicted SM backgrounds yields and the observed events in SR. Only systematic uncertainties are included in this table.

SR	higgsino SR
Observed events	33
Fitted bkg events	24.59 ± 3.53
Fitted powheg_ttbar events	10.32 ± 2.56
Fitted powheg_singletop events	3.55 ± 1.29
Fitted amcnlo_ttV events	0.14 ± 0.06
Fitted sherpa22_Wjets events	7.77 ± 2.66
Fitted sherpa221_diboson events	2.23 ± 1.00
Fitted sherpa22_Zjets events	0.60 ± 0.55
MC exp. SM events	27.50 ± 4.28
MC exp. powheg_ttbar events	14.12 ± 2.52
MC exp. powheg_singletop events	3.54 ± 1.29
MC exp. amcnlo_ttV events	0.14 ± 0.06
MC exp. sherpa22_Wjets events	6.90 ± 2.12
MC exp. sherpa221_diboson events	2.21 ± 1.00
MC exp. sherpa22_Zjets events	0.60 ± 0.55

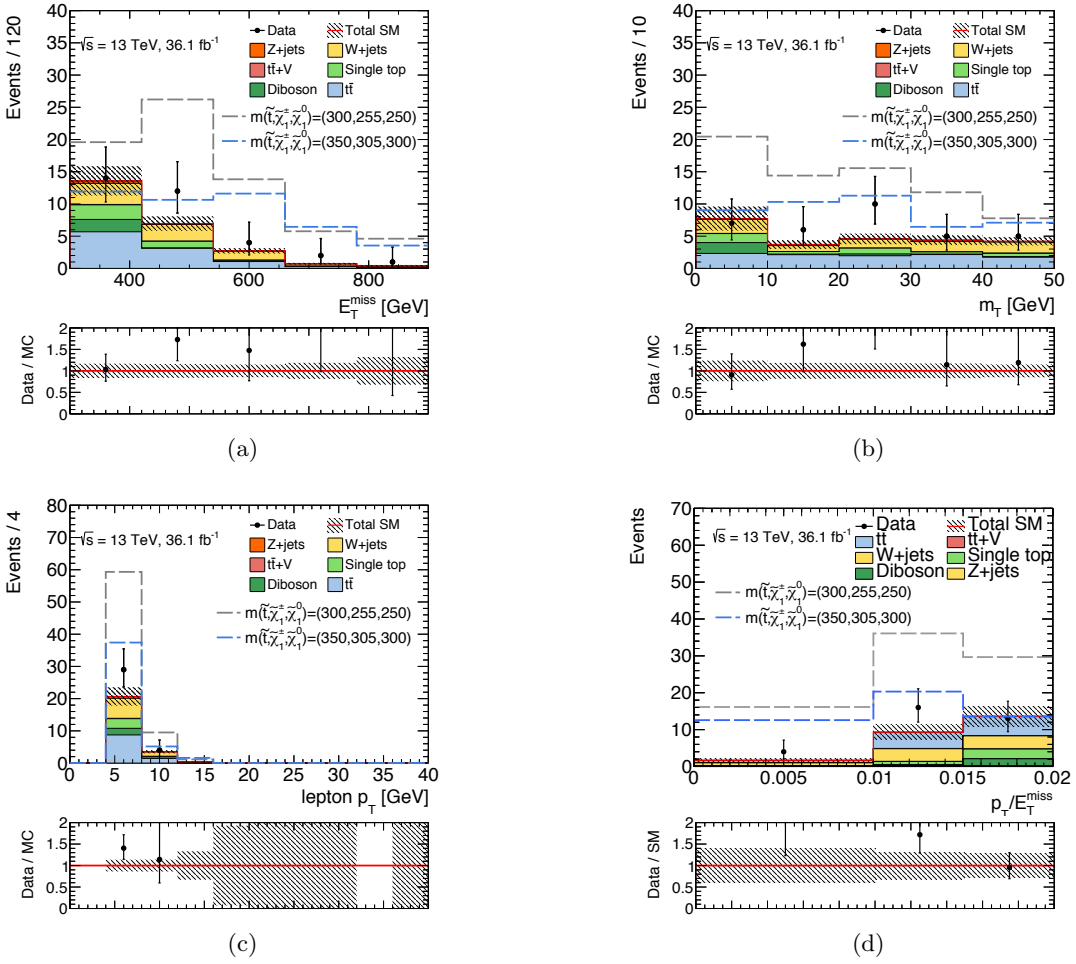

Figure 6.23: Unblinded variable's distributions including the benchmark signal distributions: (a) $E_{\mathrm{T}}^{\mathrm{miss}}$, (b) m_{T}, (c) p_{T}^{ℓ}, (d) $p_{\mathrm{T}}^{\ell}/E_{\mathrm{T}}^{\mathrm{miss}}$.

Table 6.12: Breakdown of the dominant systematic uncertainties on background estimates in the SR. Note that the individual uncertainties can be correlated, and do not necessarily add up quadratically to the total background uncertainty. The percentages show the size of the uncertainty relative to the total expected background.

Uncertainty of channel	higgsino SR
Total background expectation	24.59
Total statistical ($\sqrt{N_{\text{exp}}}$)	±4.96
Total background systematic	±3.53 [14.37%]
theory unc. on W+jets	±2.00 [8.1%]
MC statistics	±1.79 [7.3%]
$\mu_{W+\text{jets}}$ normalization unc.	±1.72 [7.0%]
$\mu_{t\bar{t}}$ normalization unc.	±1.57 [6.4%]
theory unc. on $t\bar{t}$	±1.55 [6.3%]
c- or light-jet tagging	±1.34 [5.5%]
theory unc. on single Top	±1.22 [5.0%]
pile-up	±1.12 [4.5%]
jet and met	±0.91 [3.7%]
theory unc. on dibosons	±0.66 [2.7%]
theory unc. on Z+jets	±0.53 [2.2%]
b-jet tagging	±0.46 [1.9%]
theory unc. on $t\bar{t}$V	±0.02 [0.07%]

6.6 Interpretation on the Higgsino LSP Scenario

In the absence of a statistically significant excess, the result is interpreted as the exclusion limits on the higgsino LSP scenario. To enhance the exclusion limit reach, the "**shape fit**" method is used for setting the limit.

6.6.1 Shape Fit

The shape fit method is the one of statistical combination techniques to consider signal and background separations along certain variables in SR and CR. The shape information is introduced by separating the SR corresponding to the each bin of a histogram of one variable. $p_{\text{T}}^{\ell}/E_{\text{T}}^{\text{miss}}$ variable, which powerful to separate between the signal and backgrounds, is used, and it is separated to three bins corresponding to the ranges: 0-0.01, 0.01-0.015, 0.015-0.02. Each likelihood function corresponding to the each bin is calculated with same signal strength in all bins. Thus, the full likelihood function is defined as

$$\begin{aligned} L(n,|\mu,\boldsymbol{b},\boldsymbol{\theta}) &= \prod_{i}^{3} P_i(n_{SR_i}|E_{SR_i}(\mu,\boldsymbol{b},\boldsymbol{\theta}))\times \\ &\quad P(n_{\text{TCR}}|E_{\text{TCR}}(\mu,\boldsymbol{b},\boldsymbol{\theta}))\times P(n_{\text{WCR}}|E_{\text{WCR}}(\mu,\boldsymbol{b},\boldsymbol{\theta}))\cdot C_{\text{nuis}}(\boldsymbol{\theta}). \end{aligned} \tag{6.10}$$

6.6.2 Exclusion Limit

The exclusion limit is calculated for the stop and neutralino masses of the higgsino LSP scenario with BR($\tilde{t}_1 \to b\tilde{\chi}_1^{\pm}$) = 100%. All of uncertainties except those on the theoretical signal cross-section are included in the fit. Exclusion limit at 95% confidence level (CL) is obtained with signal strength $\mu = 1$. Figure 6.24 shows the

observed and expected exclusion contours as a function of stop and neutralino masses for the higgsino LSP scenario. The "expected" label indicates that the N_{obs} is assumed the expectation value of the background-only hypothesis ($N_{\text{obs}} = N_{\text{bkg}}$) estimated by the MC prediction in the SR yield. The "observed" label indicates that the N_{obs} is the number of observed events in the SR yield. The $\pm\sigma_{\text{exp}}$ uncertainty band indicates the impact on the expected limit of the systematic and statistical uncertainties included in the fit. Thus, the higgsino SR excludes stop mass up to 415 GeV and this is the first result for the boundary region of the higgsino LSP scenario.

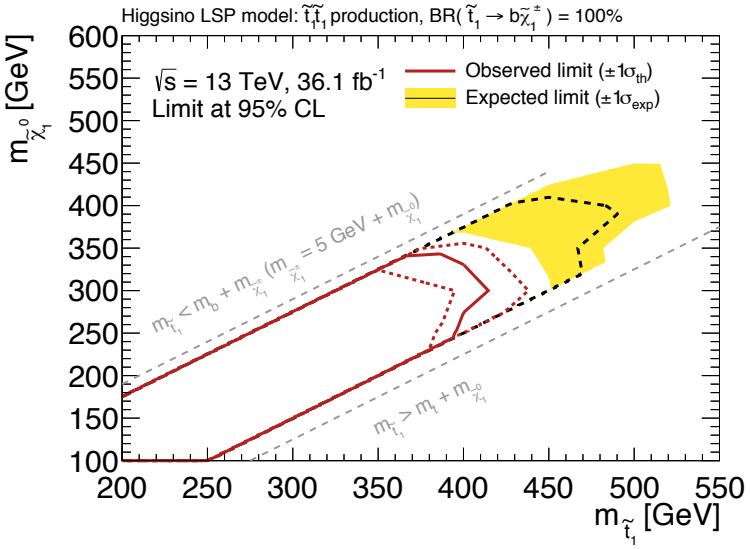

Figure 6.24: Exclusion contour as a function of stop and neutralino mass for the higgsino LSP scenario with BR($\tilde{t}_1 \to b\tilde{\chi}_1^{\pm}$) = 100%. This exclusion limit is provided at 95% CL. The black dashed lines shows expected limits at 95% CL, with the light (yellow) bands indicating the 1σ excursions due to experimental and background-only theoretical uncertainties. Observed limits are indicated by medium red curves where solid contour represents the nominal limit, and the dotted lines are obtained by varying the signal cross-section by considered theoretical uncertainties.

Chapter 7

Analysis for the Wino NLSP Scenario

In this chapter, I explain the analysis of the stop search in the wino NLSP scenario. First of all the typical topology of the stop production and decay in this scenario are introduced. Second, the analysis procedure including the event selection, the estimation of the remained backgrounds are shown. Finally, I show the number of data and estimated backgrounds in the signal region and the physics interpretation of its result.

7.1 Event Topology

Figure 7.1 shows the event topology of the stop-pair production and their decays in the wino NLSP scenario. As described in section 2.3, the wino NLSP scenario assumes that the difference of the mass between the stop and the chagino is as small as 10 GeV. The mass of chargino is larger than the one of the neutralino and difference of them are assumed to be less than 1 TeV in this scenario.

Because of the degeneracy of the stop mass and the chagino mass, the momentum of a b-jet from the $\tilde{t}_1 \to b\tilde{\chi}_1^{\pm}$ decay tends to be too low to detect in the ATLAS detector. A lepton, jets from $\tilde{\chi}_1^{\pm} \to \ell\nu\tilde{\chi}_1^0$ and $\tilde{\chi}_1^{\pm} \to qq\tilde{\chi}_1^0$ decays tend to have high momentum. The large $E_{\mathrm{T}}^{\mathrm{miss}}$ needs to be required to tell the signal event from the background events. As a result of the requirement of the high $E_{\mathrm{T}}^{\mathrm{miss}}$, the single event where two neutralinos are emitted to the same directions tends to be selected. Taken into account these signature, the requirement of the b-jets veto, a high-p_{T} lepton, high-p_{T} jets, high $E_{\mathrm{T}}^{\mathrm{miss}}$ is effective to select the event topology of this specific stop decay.

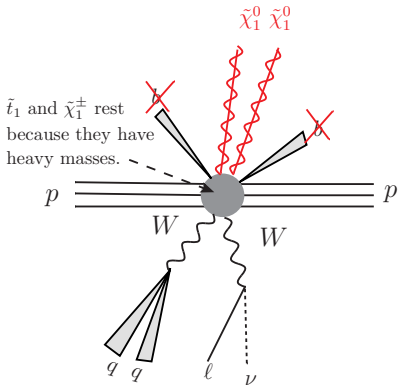

Figure 7.1: Illustration of the target event topology with requirements of high $E_{\mathrm{T}}^{\mathrm{miss}}$ and b-jet veto.

The backgrounds to be considered in this analysis are the $t\bar{t}$, single top, $t\bar{t}+V$, $W+$jets, and diboson ($WW/WZ/ZZ, etc$) events (Feynman diagrams of these backgrounds are described in Section 4.2.2). The dominant background in this analysis is the $W+$jets event, where W decays into a electron or a muon and a neutrino. Because of the requirement of the high $E_{\mathrm{T}}^{\mathrm{miss}}$, $W+$jets event where the W is boosted tends to be selected. Therefore a lepton is emitted to the same direction of the $E_{\mathrm{T}}^{\mathrm{miss}}$, as shown in Figure 7.2(b). The $t\bar{t}$, single top, and $t\bar{t}+V$ backgrounds can be eliminated effectively by the requirement of the b-jet veto. The number of the remaining $t\bar{t}$ events after all event selections is estimated by data and simulation as described in Section 7.4.2. The numbers of remaining single top and $t\bar{t}+V$ events after the event selections are estimated by simulation. The diboson background is estimated by the simulation.

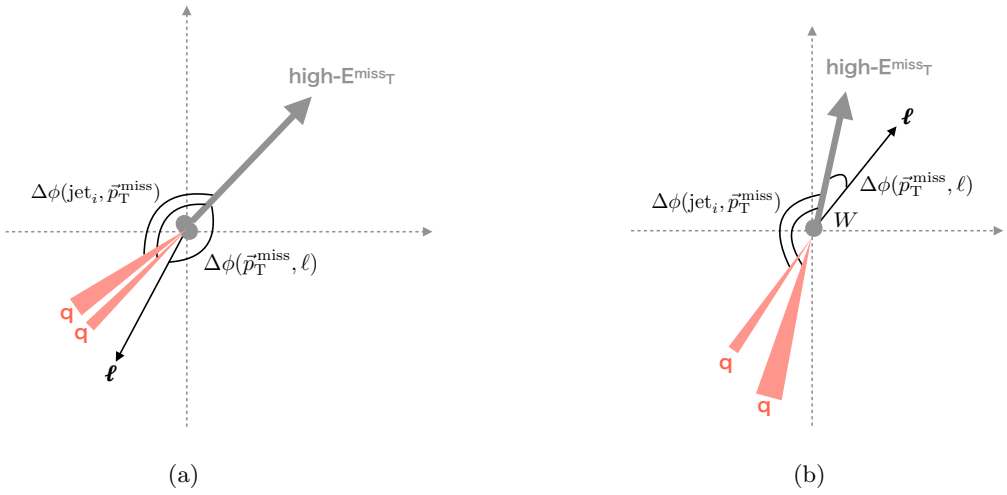

Figure 7.2: Event topologies for (a) signal and main backgrounds (b) $W+$jets.

7.2 Event Selection for Signal Region

The criteria of the event selection is determined using simulation samples for both signal and background events. For the optimization of event selection, two benchmarks of the signal simulation and the background simulation listed in Section 4.3 are used. Two benchmarks of the signal simulation vary in the masses of stop, chargeno, and neutralino. In this analysis $(m_{\tilde{t}_1}, m_{\tilde{\chi}_1^\pm}, m_{\tilde{\chi}_1^0})$ = (550 GeV, 540 GeV, 1 GeV) and (650 GeV, 640 GeV, 1 GeV) are adopted. First, the preselection based on the event topology described in Section 7.1 is applied. In order to improve the sensitivity of the signal events over the background events, further selections are determined by the optimization of the event selection.

7.2.1 Preselection

Event selections are applied in the samples collected by the $E_{\mathrm{T}}^{\mathrm{miss}}$ trigger with the threshold of $E_{\mathrm{T}}^{\mathrm{miss}} > 230$ GeV. After applying that the event has no cosmic-ray muon candidates and a good primary vertex candidate, following pre-selections are applied:

- exactly one hard electron described in section 5.2.2 or muon described in Section 5.3.2,
- lepton $p_{\mathrm{T}} \geq 40$ GeV,

- no additional baseline electron and muon in the event,
- $N_{\text{b-jets}} = 0$,
- leading jet $p_{\mathrm{T}} > 120$ GeV,
- second leading jet $p_{\mathrm{T}} > 40$ GeV,
- $E_{\mathrm{T}}^{\mathrm{miss}} > 230$ GeV,
- $m_{\mathrm{T}} > 200$ GeV,
- $|\Delta\phi(\vec{p}_{\mathrm{T}}^{\mathrm{miss}}, \ell)| > 0.4$,
- $|\Delta\phi(\mathrm{jet}_1, \vec{p}_{\mathrm{T}}^{\mathrm{miss}})| > 2.0$, and
- $|\Delta\phi(\mathrm{jet}_2, \vec{p}_{\mathrm{T}}^{\mathrm{miss}})| > 0.8$,

where m_{T} is the transverse mass reconstructed by the lepton p_{T} and $E_{\mathrm{T}}^{\mathrm{miss}}$, $|\Delta\phi(\vec{p}_{\mathrm{T}}^{\mathrm{miss}}, \ell)|$is the opening azimuthal angle between $\vec{p}_{\mathrm{T}}^{\mathrm{miss}}$ and p_{T}^{ℓ}, and $|\Delta\phi(\mathrm{jet}_1, \vec{p}_{\mathrm{T}}^{\mathrm{miss}})|$ and $|\Delta\phi(\mathrm{jet}_2, \vec{p}_{\mathrm{T}}^{\mathrm{miss}})|$ are opening azimuthal angles between $p_{\mathrm{T}}^{\mathrm{jet}_1}$ and $p_{\mathrm{T}}^{\mathrm{jet}_2}$ and p_{T}^{ℓ}, respectively. Figure 7.3 shows the distribution of $E_{\mathrm{T}}^{\mathrm{miss}}$, leading jet p_{T}, lepton p_{T} and the number of jets for the two benchmarks of signal simulation and simulated backgrounds.

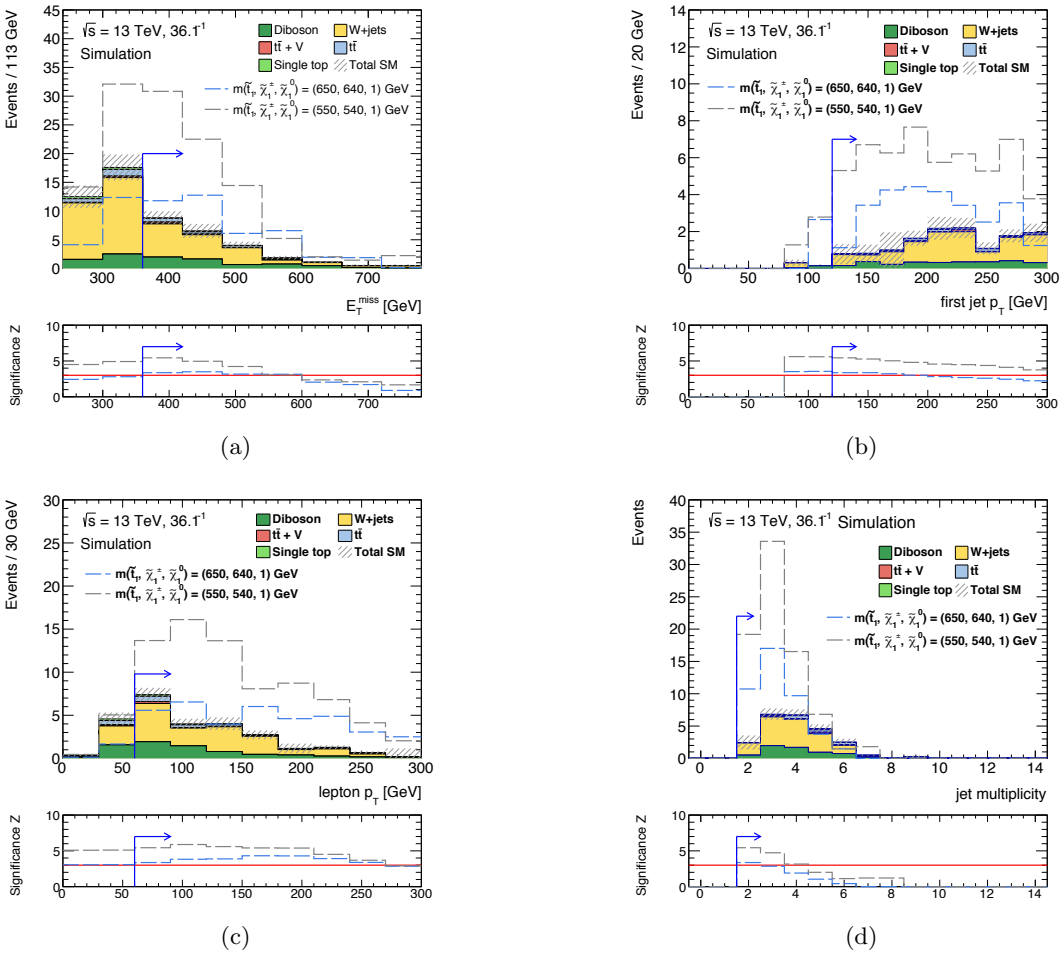

Figure 7.3: Distributions of the variables used for preselection for the wino NLSP scenario: (a) $E_{\mathrm{T}}^{\mathrm{miss}}$, (b) $p_{\mathrm{T}}^{\mathrm{jet}_1}$, (c) p_{T}^{ℓ}, (d) jet multiplicity.

7.2.2 SR Optimization

Further criteria of the event selection are determined by the selection optimization, so that the significance of the signal extraction over the background events (Z), defined in Appendix A, is improved. The selection criteria for the $E_{\mathrm{T}}^{\mathrm{miss}}$, p_{T}^{ℓ}, $p_{\mathrm{T}}^{\mathrm{jet_2}}$, $|\Delta\phi(\vec{p}_{\mathrm{T}}^{\mathrm{miss}}, \ell)|$, $m_W^{\mathrm{reclustered}}$, and $H_{\mathrm{T}}^{\mathrm{sig}}$ [27] are varied as shown in Table 7.1, where $m_W^{\mathrm{reclustered}}$ is the W boson mass reconstructed by two small-radius jets clustered by the large-radius jets, $H_{\mathrm{T}}^{\mathrm{sig}}$ is defined as:

$$H_{\mathrm{T}}^{\mathrm{sig}} = \frac{|\vec{H}_T^{\mathrm{miss}}| - M}{\sigma_{|\vec{H}_T^{\mathrm{miss}}|}}. \tag{7.1}$$

$H_{\mathrm{T}}^{\mathrm{sig}}$ is the negative of the scalar sum of jet and lepton p_{T}. The $|\vec{H}_{\mathrm{T}}^{\mathrm{miss}}|$ and resolution ($\sigma_{|\vec{H}_T^{\mathrm{miss}}|}$) are computed from the psudo-events with $N = 1000$ events. An i^{th} psudo-event calculates following items:

1. For all n jets in an event, a p_{T} distribution of each jet, which follows the Gaussian distribution considering the JER of each jet (mean value: $p_{\mathrm{T}}^{\mathrm{jet_j}}$, standard deviation: $p_{\mathrm{T}}^{\mathrm{jet_j}} \times \mathrm{JER}_j$), is generated. After that, the random value of $p_{\mathrm{T}}^{\mathrm{jet_i}}$ is extracted from this distribution;
2. The value "$E_{\mathrm{T,i}}^{\mathrm{miss}^*} = -\sum_j^n p_{\mathrm{T}}^{\mathrm{jet_j}} \sum_\ell p_{\mathrm{T}}^{\ell}$" is calculated by the extracted $p_{\mathrm{T}}^{\mathrm{jet_j}}$ and total sum of lepton p_{T} $\sum_\ell p_{\mathrm{T}}^{\ell}$.

This calculation is iterated until $i = 1000$. In fact, when this calculation finishes ($i = 1000$), the total value $\sum_i^{N=1000} E_{\mathrm{T,i}}^{\mathrm{miss}^*}$ represents the sum of psudo $E_{\mathrm{T}}^{\mathrm{miss}}$ distributions corresponding to the JER of each jet. The value $|\vec{H}_{\mathrm{T}}^{\mathrm{miss}}|$ is mean value of $\sum_i^{N=1000} E_{\mathrm{T,i}}^{\mathrm{miss}^*}$ and $|\vec{H}_{\mathrm{T}}^{\mathrm{miss}}| = (\sum_i^{N=1000} E_{\mathrm{T,i}}^{\mathrm{miss}^*})/1000$. The resolution $\sigma_{|\vec{H}_T^{\mathrm{miss}}|}$ is a standard deviation of this psudo-distribution and $\sigma_{|\vec{H}_T^{\mathrm{miss}}|} = \sqrt{\frac{(\sum_i^{N=1000} E_{\mathrm{T,i}}^{\mathrm{miss}^*})^2}{1000} - (\frac{\sum_i^{N=1000} E_{\mathrm{T,i}}^{\mathrm{miss}^*}}{1000})^2}$. M in Equation 7.1 is set as 100 GeV in this analysis, which is optimized by the previous study [27, 124]. Figure 7.4

Table 7.1: The list of scanned cut values of several kinematic variables.

Cut variables	Scanned cut values
$E_{\mathrm{T}}^{\mathrm{miss}}$ [GeV]	> 230, > 300, > 360, > 420, > 480
p_{T}^{ℓ}	> 40, > 60, > 80, > 100
$p_{\mathrm{T}}^{\mathrm{jet_2}}$	> 40, > 60, > 80, > 100
$\lvert\Delta\phi(\vec{p}_{\mathrm{T}}^{\mathrm{miss}}, \ell)\rvert$	> 0.4, > 1.2, > 2.0, > 2.8
$m_W^{\mathrm{reclustered}}$ [GeV]	$0 < m_W^{\mathrm{reclustered}} < 160$, $40 < m_W^{\mathrm{reclustered}} < 130$, $70 < m_W^{\mathrm{reclustered}} < 100$
$H_{\mathrm{T}}^{\mathrm{sig}}$	> 12, > 16, > 20, > 24

shows the distribution of $p_{\mathrm{T}}^{\mathrm{jet_2}}$, $|\Delta\phi(\vec{p}_{\mathrm{T}}^{\mathrm{miss}}, \ell)|$, $m_t^{\mathrm{reclustered}}$, and $H_{\mathrm{T}}^{\mathrm{sig}}$. The $E_{\mathrm{T}}^{\mathrm{miss}}$ described in Figure 7.3(a) is defined as more than 360 GeV, this cut value can obtain the highest significance Z value for the benchmark points. The cut value of the p_{T}^{ℓ} described in Figure 7.3(c) is defined as 60 GeV, and the significance Z value can be obtained more than 3. Figure 7.4(a) shows the $p_{\mathrm{T}}^{\mathrm{jet_2}}$ distribution and the cut value is defined as more than 80 GeV to obtain the highest significance Z value around 3. Figure 7.4(b) shows the $|\Delta\phi(\vec{p}_{\mathrm{T}}^{\mathrm{miss}}, \ell)|$distribution. This variable can have a good separation power between the signal and $W+$jets background due to the topology difference. The cut value is defined as more than 1.2. Figure 7.4(c) shows the $m_W^{\mathrm{reclustered}}$ distribution. Two jets of signal are originated from the W boson, however two jets of the $W+$ jets background are originated from additional jets. If the $m_W^{\mathrm{reclustered}}$ calculated by using the momenta of two jets, the signal has the peak around W boson mass in the $m_W^{\mathrm{reclustered}}$ distribution and the $m_W^{\mathrm{reclustered}}$ distribution of $W+$jets background tends to be flat. Thus, it can have a good separation power and it is defined as $70 < m_W^{\mathrm{reclustered}} < 100$ GeV. Figure 7.4(d) shows the $H_{\mathrm{T}}^{\mathrm{sig}}$ distribution. If the final state particles have high momenta, this variable tend to

be obtained higher value. It is defined as more than 16 for getting the significance Z value to be more than 3 taken into account the statistics.

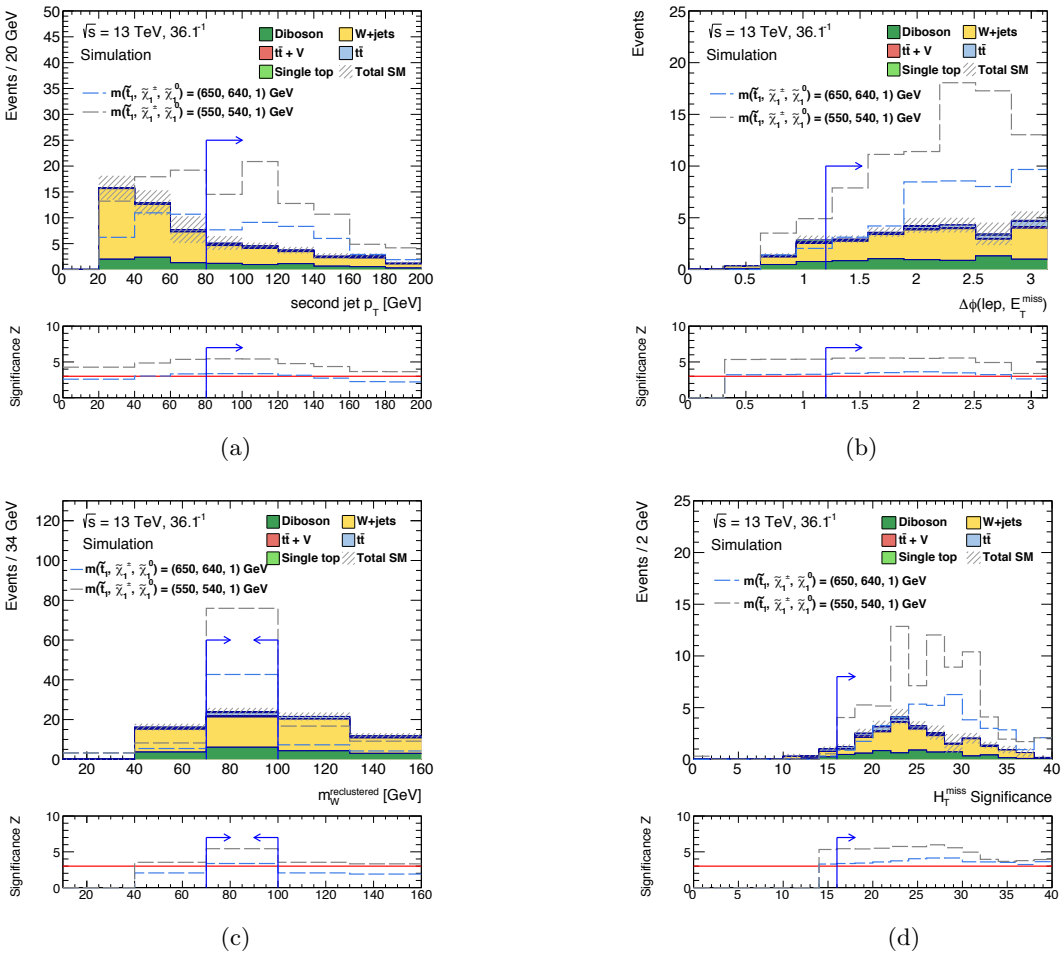

Figure 7.4: Distributions of kinematic variables after the event selection except for the requirements on the variable for which the distribution is shown for the wino SR optimization: (a) $p_{\mathrm{T}}^{\mathrm{jet}_2}$, (b) $|\Delta\phi(\vec{p}_{\mathrm{T}}^{\mathrm{miss}}, \ell)|$, (c) $m_t^{\mathrm{reclustered}}$, and (d) $H_{\mathrm{T}}^{\mathrm{sig}}$.

7.3 Background Estimations

The numbers of the $t\bar{t}$ and W + jets and background events after the all event selections are estimated by the semi-data driven method. In this method, dedicated control regions, TCR and WCR are defined to normalize the simulated events to data with a simultaneous fit. TCR and WCR are defined with event selections which are kinematically close to the SR but a few selection criteria inverted to reduce the signal contribution and to enhance the $t\bar{t}$ and W + jets events, respectively. Minor backgrounds such as the single-top, and $t\bar{t} + V$ are estimated by using purely simulation. The definitions of the CR for the TCR and the WCR are summarized in Table 7.2. For validations of the estimation, the VR is defined as shown in Table 7.2. The event selection for TCR is defined with the same event selection for the signal region but the selections of the number of b-tagged jets, m_{T}, and $|\Delta\phi(\vec{p}_{\mathrm{T}}^{\mathrm{miss}}, \ell)|$. The TCR is defined as 30 GeV $< m_{\mathrm{T}} <$ 90 GeV and no $|\Delta\phi(\vec{p}_{\mathrm{T}}^{\mathrm{miss}}, \ell)|$ selection, and the TVR is defined as 90 GeV $< m_{\mathrm{T}} <$ 120 GeV. WCR is defined as b-jet multiplicity=0, 30 GeV $< m_{\mathrm{T}} <$ 90 GeV and no $|\Delta\phi(\vec{p}_{\mathrm{T}}^{\mathrm{miss}}, \ell)|$ selection, and WVR is defined as 90 GeV $< m_{\mathrm{T}} <$ 120 GeV.

Table 7.2: Overview of the event selections for SR, CRs, and VRs. Square brackets are used to show a range of the requirement.

Cut Variables	SR	TCR	TVR	WCR	WVR
Number of b-tagged jets	$= 0$	≥ 1	≥ 1	$= 0$	$= 0$
m_{T} [GeV]	> 200	[30, 90]	[90, 120]	[30, 90]	[90, 120]
$\lvert\Delta\phi(\vec{p}_{\mathrm{T}}^{\,\mathrm{miss}}, \ell)\rvert$	> 1.2	-	-	-	-

7.4 Results

In this section, the final results for the wino NLSP scenario is presented. First, the result of the background-only fit is shown, which provides the estimation of backgrounds with the impact of the systematic uncertainty, and so the results of the comparison between the observed data and the backgrounds in CRs and VRs are shown. Finally, the final comparison between the observed data and the backgrounds in SR and this interpretation are shown.

7.4.1 The Result of the Background-only Fit

The background-only fit is performed to derive the $t\bar{t}$ and W + jets normalization factors from CRs with high purity $t\bar{t}$ or W + jets events. The both CRs are taken into account not to be contaminated by signal. Other backgrounds are included in this fit within their respective uncertainties. The $t\bar{t}$ and W + jets normalization factors are free parameters and are fitted to

$$\mu_{t\bar{t}} = 0.79 \pm 0.28, \tag{7.2}$$

$$\mu_{W+\mathrm{jets}} = 1.09 \pm 0.09. \tag{7.3}$$

Table 7.3: Background-only fit results for the TCR, WCR, TVR, and WVR. The lower part of this table shows the nominal MC expectations before the fit, and the upper part of this table shows the background expectations after the fit.

wino SR	TCR	WCR	TVR	WVR
Observed events	271	436	30	24
Fitted bkg events	270.80 ± 16.51	436.01 ± 20.88	27.95 ± 6.30	27.19 ± 4.24
Fitted powheg_ttbar events	145.69 ± 50.39	12.83 ± 6.37	15.60 ± 7.56	0.93 ± 0.49
Fitted powheg_singletop events	50.97 ± 44.44	8.85 ± 7.76	4.72 ± 3.55	0.53 ± 0.40
Fitted amcnlo_ttV events	2.96 ± 0.32	0.23 ± 0.08	0.32 ± 0.15	0.03 ± 0.01
Fitted sherpa22_Wjets events	64.89 ± 11.97	379.71 ± 24.44	6.74 ± 1.75	24.05 ± 3.65
Fitted sherpa221_diboson events	6.30 ± 2.13	34.40 ± 9.94	0.58 ± 0.23	1.65 ± 1.00
MC exp. SM events	304.19 ± 47.77	409.76 ± 23.86	31.57 ± 8.14	25.56 ± 4.19
MC exp. powheg_ttbar events	184.00 ± 9.58	16.22 ± 5.40	19.73 ± 6.73	1.17 ± 0.45
MC exp. powheg_singletop events	51.08 ± 44.50	8.86 ± 7.77	4.73 ± 3.56	0.53 ± 0.40
MC exp. amcnlo_ttV events	2.96 ± 0.33	0.23 ± 0.08	0.32 ± 0.15	0.03 ± 0.01
MC exp. sherpa22_Wjets events	59.83 ± 9.48	349.94 ± 15.84	6.21 ± 1.44	22.17 ± 3.28
MC exp. sherpa221_diboson events	6.32 ± 2.14	34.51 ± 10.02	0.58 ± 0.24	1.65 ± 1.01

Table 7.3 shows the background yields before and after the fit and the number of observed events in all CRs and VRs. The observed events and the total number of fitted background events in each CRs and VRs are consistent. Figures 7.5, 7.6, 7.7, 7.8 show some variable's distributions in each CR and VR. The shapes of All distributions in each CR are consistent between the data and the fitted MC predictions. Therefore, the $t\bar{t}$ and W + jets normalization factors are good agreements, and they can be used for the background estimation in SR.

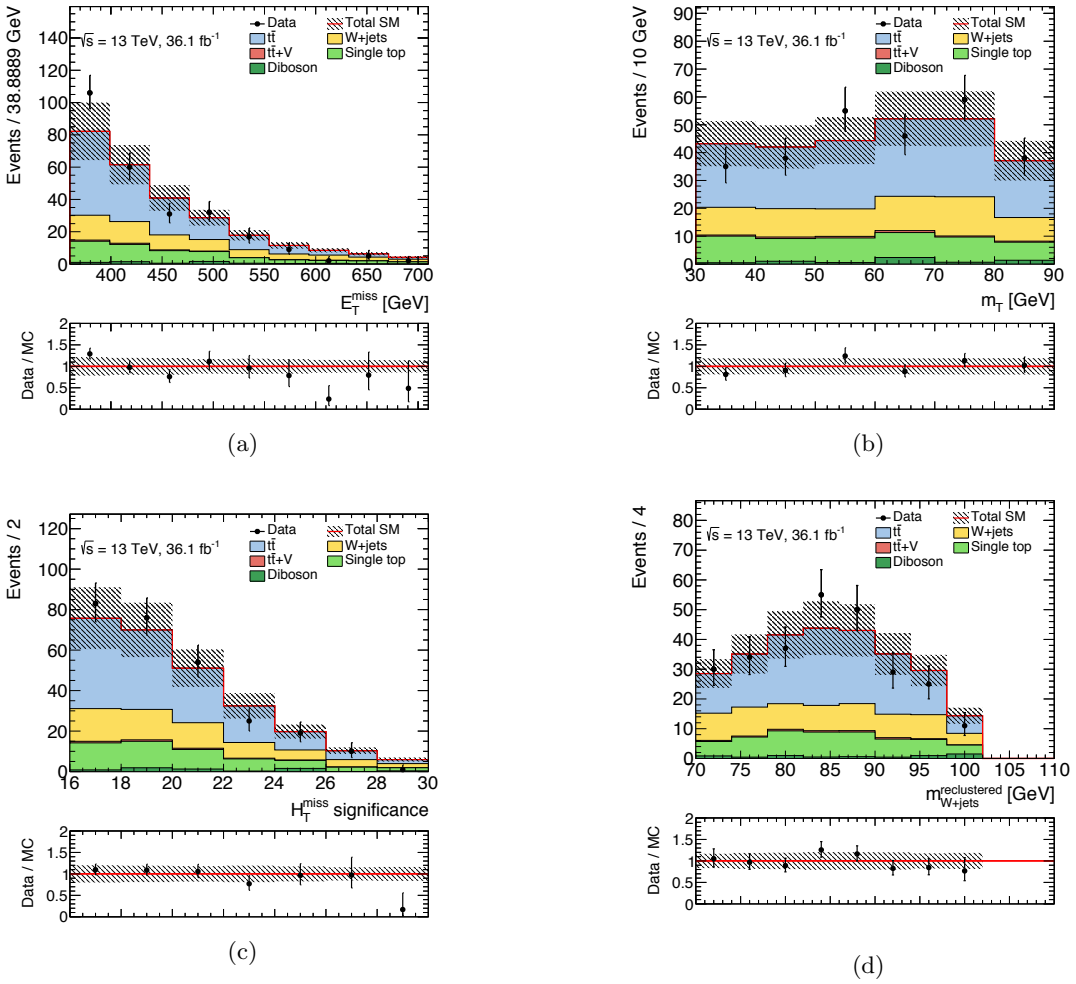

Figure 7.5: Observed distributions of selected variables in TCR: (a) $E_{\mathrm{T}}^{\mathrm{miss}}$, (b) m_{T}, (c) $H_{\mathrm{T}}^{\mathrm{sig}}$, (d) $m_{W}^{\mathrm{reclustered}}$. The histograms show the MC background predictions, normalised to cross-section times integrated luminosity and the dominant process in each CR is normalised to data. The hatched red error bands indicate the combined uncertainties.

Table 7.4 shows systematic uncertainties in each CR and VR. These tables include only some dominantly uncertainties. The 1st dominant uncertainty in TCR is the uncertainty coming from the $t\bar{t}$ normalization factor and it has about 19%. In case of WCR, the 1st dominant uncertainty is the uncertainty coming from the W + jets normalization factor and it has about 7%. In the VRs, the 1st dominant uncertainty in TVR is also same as TCR which is about 20%, and the 1st dominant uncertainty in WVR is the JER and it is about 9%. The amount of individual uncertainties are derived by setting all other nuisance parameters to constant without the parameter of interest and then propagating the uncertainty due to this parameter only.

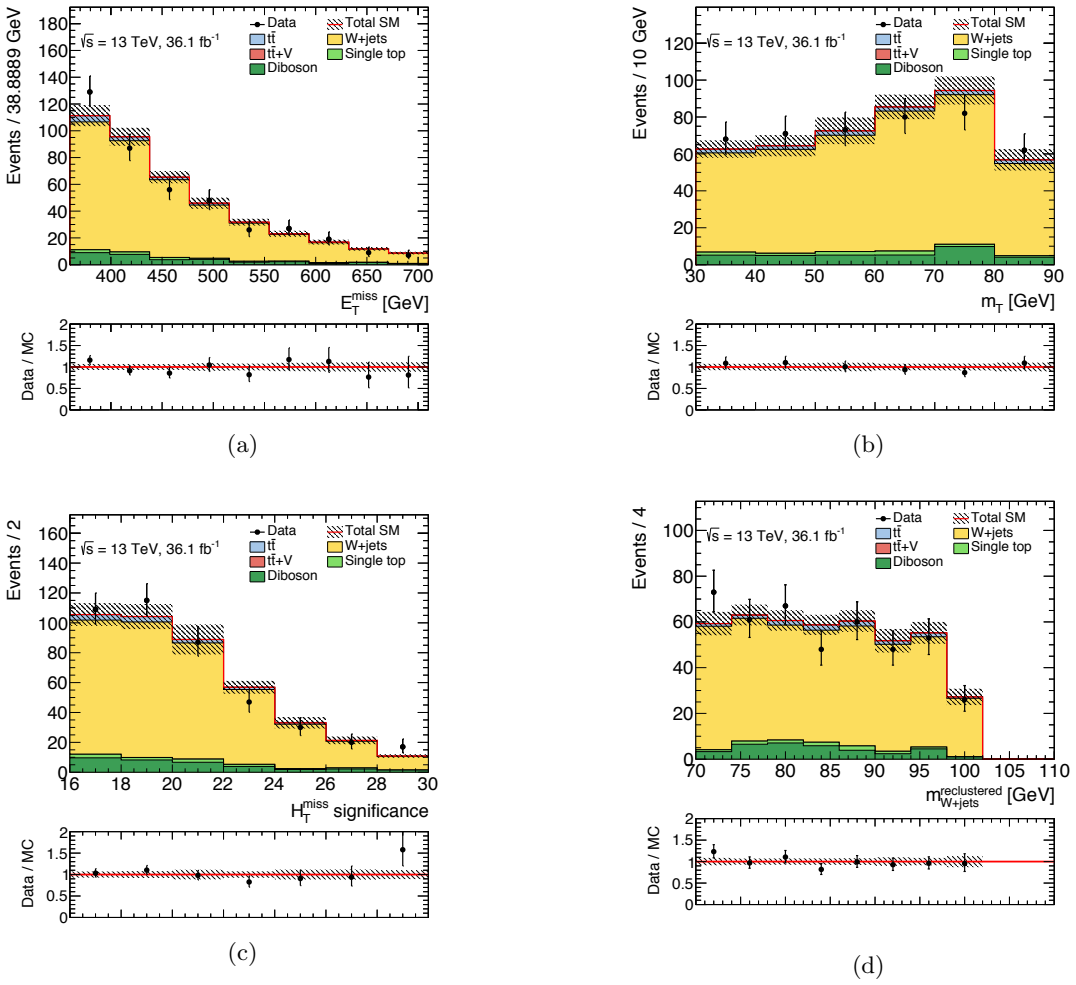

Figure 7.6: Observed distributions of selected variables in WCR: (a) $E_{\mathrm{T}}^{\mathrm{miss}}$, (b) m_{T}, (c) $H_{\mathrm{T}}^{\mathrm{sig}}$, (d) $m_{W}^{\mathrm{reclustered}}$. The histograms show the MC background predictions, normalised to cross-section times integrated luminosity and the dominant process in each CR is normalised to data. The hatched red error bands indicate the combined uncertainties.

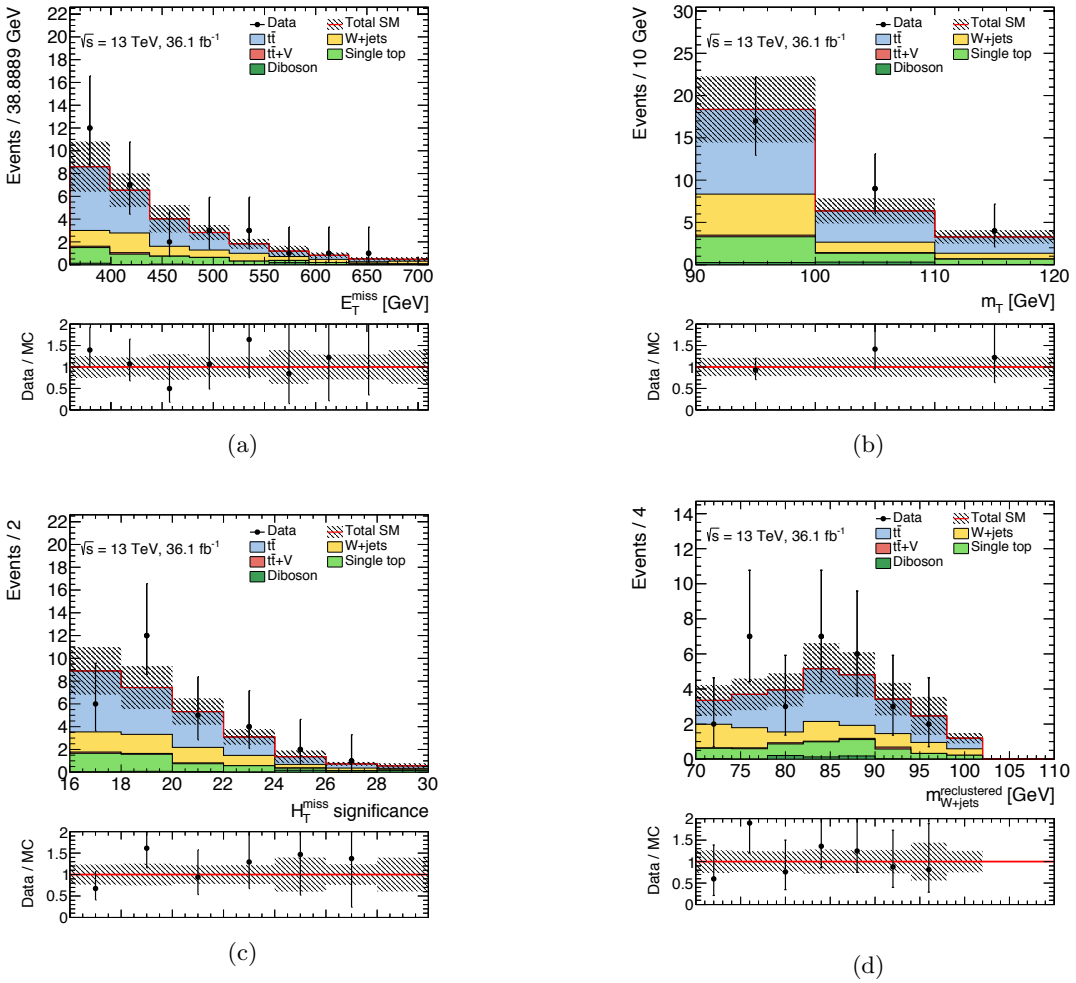

Figure 7.7: Observed distributions of selected variables in TVR: (a) $E_{\mathrm{T}}^{\mathrm{miss}}$, (b) m_{T}, (c) $H_{\mathrm{T}}^{\mathrm{sig}}$, (d) $m_{W}^{\mathrm{reclustered}}$. The histograms show the MC background predictions, normalised to cross-section times integrated luminosity and the dominant process in each CR is normalised to data. The hatched red error bands indicate the combined uncertainties.

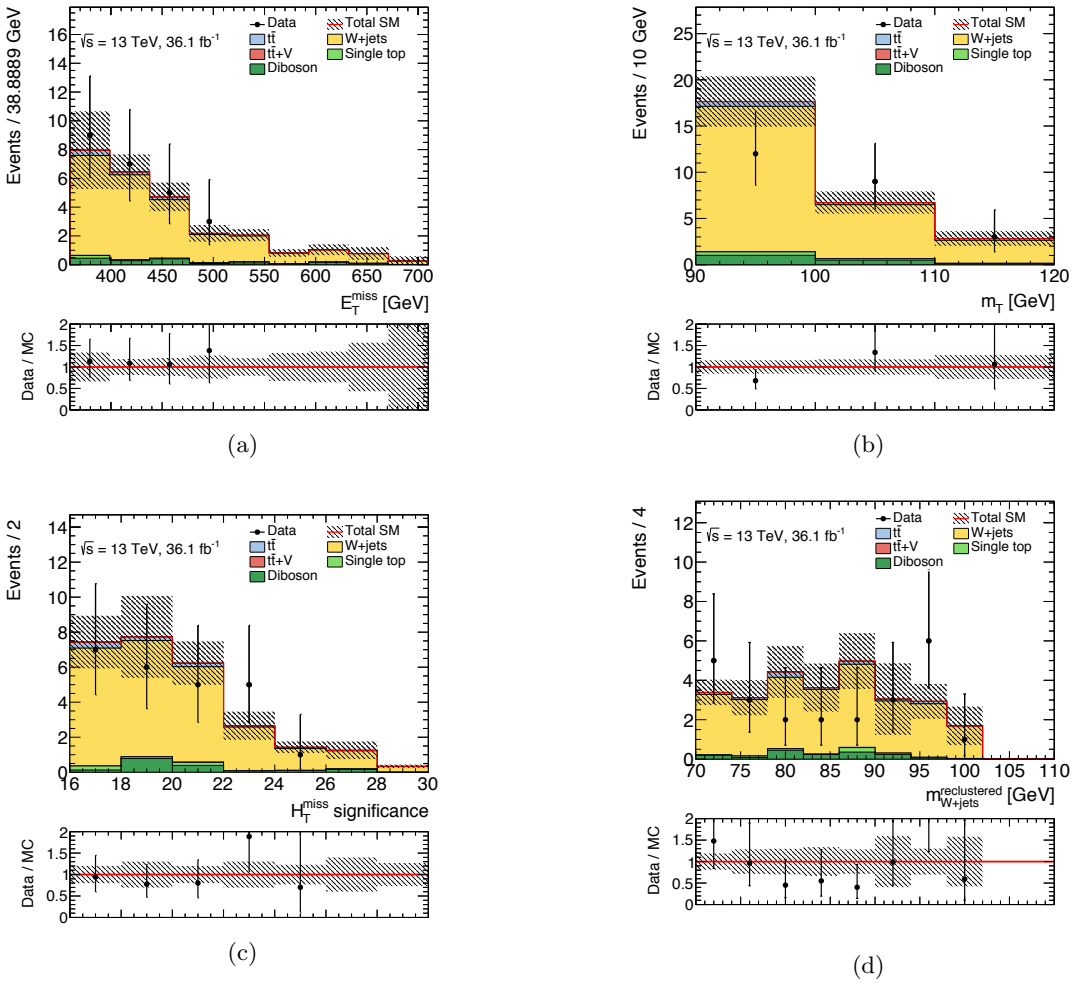

Figure 7.8: Observed distributions of selected variables in WVR: (a) $E_{\mathrm{T}}^{\mathrm{miss}}$, (b) m_{T}, (c) $H_{\mathrm{T}}^{\mathrm{sig}}$, (d) $m_{W}^{\mathrm{reclustered}}$. The histograms show the MC background predictions, normalised to cross-section times integrated luminosity and the dominant process in each CR is normalised to data. The hatched red error bands indicate the combined uncertainties.

Table 7.4: Breakdown of the dominant systematic uncertainties on background yield estimates in the various control regions. Note that the individual uncertainties can be correlated, and do not necessarily add up quadratically to the total background uncertainty. The percentages show the size of the uncertainty relative to the total expected background.

Uncertainty of channel	TCR	WCR
Total background expectation	270.80	436.01
Total statistical ($\sqrt{N_{\text{exp}}}$)	±16.46	±20.88
Total background systematic	±16.51 [6.10%]	±20.88 [4.79%]
$\mu_{t\bar{t}}$ normalization unc.	±51.22 [18.9%]	±4.51 [1.0%]
theory unc. on single Top	±44.18 [16.3%]	±7.67 [1.8%]
pile-up	±11.77 [4.3%]	±17.06 [3.9%]
jet and met	±6.86 [2.5%]	±1.81 [0.41%]
c- or light-jet tagging	±6.42 [2.4%]	±9.98 [2.3%]
b-jet tagging	±5.54 [2.0%]	±3.38 [0.77%]
$\mu_{W+\text{jets}}$ normalization unc.	±5.45 [2.0%]	±31.87 [7.3%]
theory unc. on W+jets	±4.90 [1.8%]	±0.00 [0.00%]
MC statistics	±2.77 [1.0%]	±6.38 [1.5%]
theory unc. on dibosons	±1.57 [0.58%]	±8.93 [2.0%]
theory unc. on $t\bar{t}$V	±0.00 [0.00%]	±0.00 [0.00%]
theory unc. on $t\bar{t}$	±0.00 [0.00%]	±3.90 [0.89%]
theory unc. on Z+jets	±0.00 [0.00%]	±0.00 [0.00%]

Uncertainty of channel	TVR	WVR
Total background expectation	27.95	27.19
Total statistical ($\sqrt{N_{\text{exp}}}$)	±5.29	±5.21
Total background systematic	±6.30 [22.52%]	±4.24 [15.61%]
$\mu_{t\bar{t}}$ normalization unc.	±5.49 [19.6%]	±0.33 [1.2%]
theory unc. on $t\bar{t}$	±5.00 [17.9%]	±0.30 [1.1%]
theory unc. on single Top	±3.49 [12.5%]	±0.39 [1.4%]
jet and met	±2.95 [10.6%]	±3.41 [12.5%]
MC statistics	±0.80 [2.9%]	±1.49 [5.5%]
pile-up	±0.80 [2.9%]	±1.48 [5.4%]
c- or light-jet tagging	±0.66 [2.4%]	±0.52 [1.9%]
theory unc. on W+jets	±0.66 [2.3%]	±1.58 [5.8%]
b-jet tagging	±0.59 [2.1%]	±0.21 [0.77%]
$\mu_{W+\text{jets}}$ normalization unc.	±0.57 [2.0%]	±2.02 [7.4%]
theory unc. on dibosons	±0.15 [0.54%]	±0.43 [1.6%]
theory unc. on $t\bar{t}$V	±0.00 [0.00%]	±0.00 [0.00%]
theory unc. on Z+jets	±0.00 [0.00%]	±0.00 [0.00%]

7.4.2 Unblinded SR

After validation, the background yields in SR are extracted by the extrapolation from CRs to SR with the $t\bar{t}$ and W + jets normalization factors. Table 7.5 shows the unblinded results of the predicted backgrounds yields and the observed events yields in SR, and only systematic uncertainties are included in this table. The total number of observed events is 25 events and the total number of the fitted background predictions is $25.00 \pm 5.00 \pm 3.81$. Table 7.6 shows the total systematic uncertainty and the breakdown. Figures 7.9 show $E_{\mathrm{T}}^{\mathrm{miss}}$, m_{T}, $H_{\mathrm{T}}^{\mathrm{sig}}$, and $m_W^{\mathrm{reclustered}}$ distributions in SR, and the benchmark signal distributions are also included in these figures. The number of observed events and the total number of fitted background predictions are consistent, in addition the shapes of observed events in all distributions are basically same as the shapes of the total background predictions. Therefore, no significant excess above the SM prediction found from this result.

Table 7.5: Unblinded results of the predicted SM backgrounds yields and the observed events in SR. Only systematic uncertainties are included in this table.

SR	wino SR
Observed events	25
Fitted bkg events	25.00 ± 3.81
Fitted powheg_ttbar events	1.26 ± 0.65
Fitted powheg_singletop events	0.60 ± 0.53
Fitted amcnlo_ttV events	0.57 ± 0.15
Fitted sherpa22_Wjets events	16.53 ± 3.08
Fitted sherpa221_diboson events	6.04 ± 1.93
MC exp. SM events	24.06 ± 4.08
MC exp. powheg_ttbar events	1.59 ± 0.59
MC exp. powheg_singletop events	0.60 ± 0.53
MC exp. amcnlo_ttV events	0.58 ± 0.15
MC exp. sherpa22_Wjets events	15.24 ± 2.87
MC exp. sherpa221_diboson events	6.06 ± 1.95

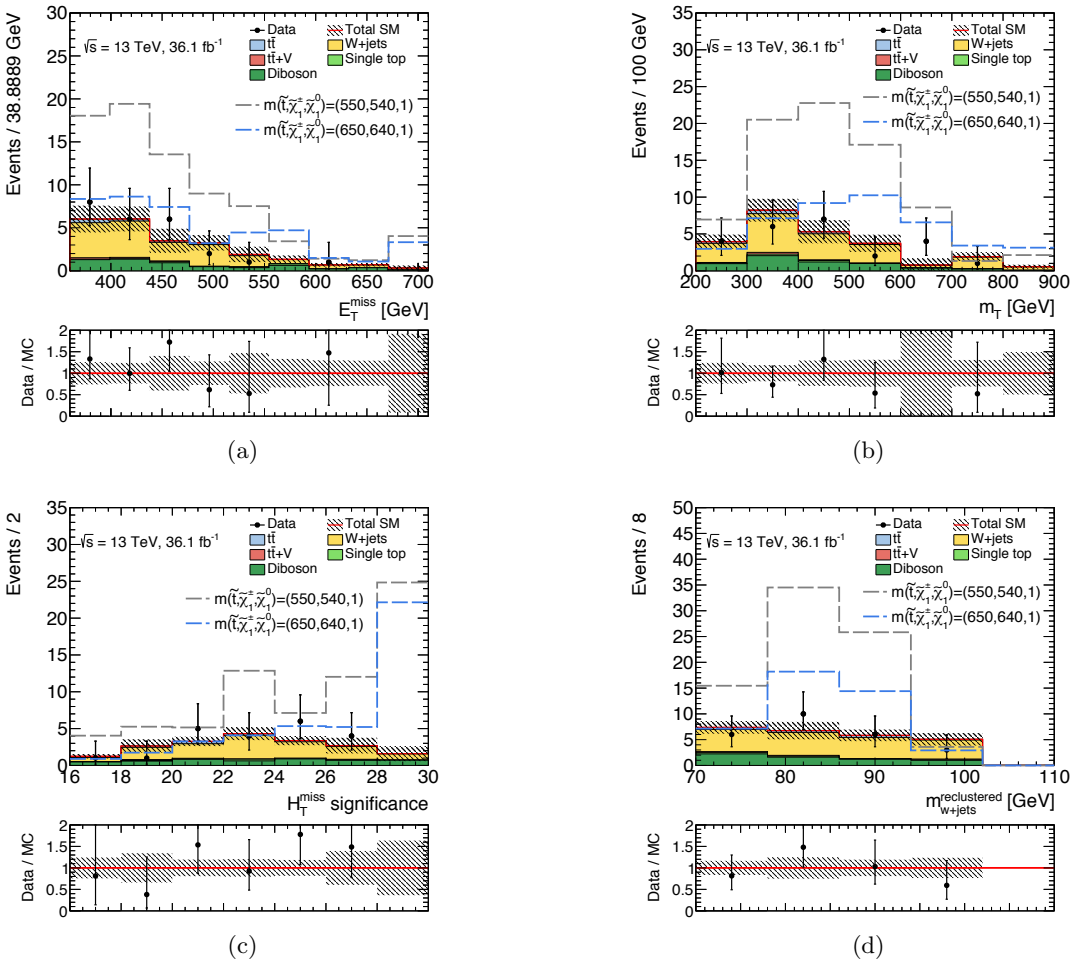

Figure 7.9: Unblinded variable's distributions including the benchmark signal distributions: (a) $E_{\mathrm{T}}^{\mathrm{miss}}$, (b) m_{T}, (c) $H_{\mathrm{T}}^{\mathrm{sig}}$, (d) $m_{W}^{\mathrm{reclustered}}$.

Table 7.6: Breakdown of the dominant systematic uncertainties on background estimates in the SR. Note that the individual uncertainties can be correlated, and do not necessarily add up quadratically to the total background uncertainty. The percentages show the size of the uncertainty relative to the total expected background.

Uncertainty of channel	wino SR
Total background expectation	25.00
Total statistical ($\sqrt{N_{\text{exp}}}$)	±5.00
Total background systematic	±3.81 [15.25%]
theory unc. on W+jets	±2.04 [8.1%]
MC statistics	±1.90 [7.6%]
pile-up	±1.77 [7.1%]
theory unc. on dibosons	±1.72 [6.9%]
jet and met	±1.71 [6.8%]
$\mu_{W+\text{jets}}$ normalization unc.	±1.39 [5.6%]
c- or light-jet tagging	±0.60 [2.4%]
theory unc. on single Top	±0.52 [2.1%]
$\mu_{t\bar{t}}$ normalization unc.	±0.44 [1.8%]
theory unc. on $t\bar{t}$	±0.40 [1.6%]
b-jet tagging	±0.38 [1.5%]
theory unc. on $t\bar{t}$V	±0.00 [0.00%]
theory unc. on Z+jets	±0.00 [0.00%]

7.5 Interpretation of Wino NLSP Scenario

7.5.1 Exclusion Limit

The exclusion limit is calculated for the stop and neutralino masses of the wino NLSP scenario with BR($\tilde{t}_1 \to b\tilde{\chi}_1^{\pm}$) = 100%. In this scenario, the exclusion limit is calculated with only total numbers of observed and expected events. All of uncertainties except those on the theoretical signal cross-section are included in the fit. Exclusion limit at 95% CL is obtained with signal strength $\mu = 1$. Figure 7.10 shows the observed and expected exclusion contours as a function of stop and neutralino masses for the wino NLSP scenario. Thus, the wino SR excludes stop mass up to 850 GeV and this is updated very widely from stop 500 GeV maximum limit for Run-1 analysis.

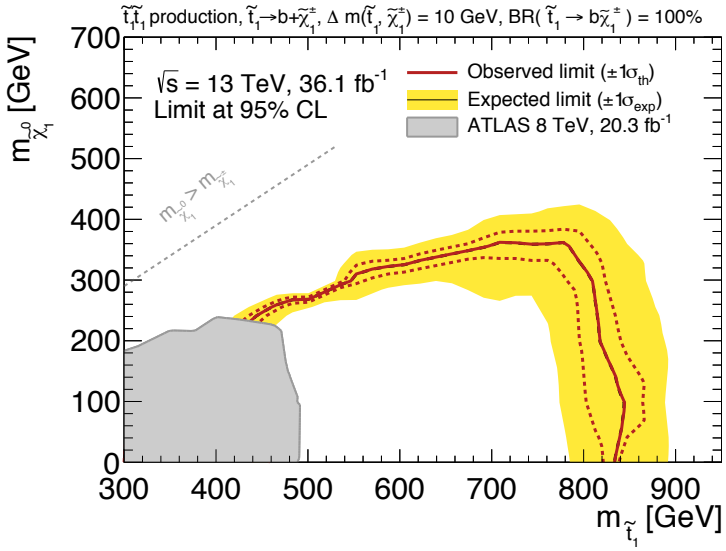

Figure 7.10: Exclusion contour as a function of stop and neutralino mass for the wino NLSP scenario with BR($\tilde{t}_1 \to b\tilde{\chi}_1^{\pm}$) = 100%. This exclusion limit is provided at 95% CL. The black dashed lines shows expected limits at 95% CL, with the light (yellow) bands indicating the 1σ excursions due to experimental and background-only theoretical uncertainties. Observed limits are indicated by medium red curves where solid contour represents the nominal limit, and the dotted lines are obtained by varying the signal cross-section by considered theoretical uncertainties.

Chapter 8

Discussion

8.1 Combination of the Higgsino LSP Scenario

Previously, a search for the stop pair production assuming the higgsino LSP scenario was performed, assuming stop can be decays in to all of $t\tilde{\chi}_2^0$, $t\tilde{\chi}_1^0$, and $b\tilde{\chi}_1^\pm$ and $_{\tilde{\chi}_1^\pm} = \mathrm{m}_{\tilde{\chi}_1^0} + 5$ GeV. In Run-1, using the decays of $\tilde{t}_1 \to b\tilde{\chi}_1^\pm$ and $\tilde{\chi}_1^\pm \to W\tilde{\chi}_1^0$ where the BR of these decays assumed to be 100%, the mass of the stop and the neutralino were excluded smaller than 600 GeV and 200 GeV at 95% CL, respectively, as shown in Figure 8.1(b). Using Run-2 data, a search for the stop pair production, where stop is assumed to decay into $t\tilde{\chi}_2^0$, $t\tilde{\chi}_1^0$, and $b\tilde{\chi}_1^\pm$ with BR($t\tilde{\chi}_2^0$, $t\tilde{\chi}_1^0$, $b\tilde{\chi}_1^\pm$) $\sim$ (45, 45, 10)% for $\tilde{t}_\mathrm{L}$ with small $\tan\beta$, (33, 33, 33)% for $\tilde{t}_\mathrm{L}$ with large $\tan\beta$, and (25, 25, 50)% for $\tilde{t}_\mathrm{R}$, was newly performed. The exclusion limit at 95% CL was almost same level as the Run-1 analysis (Figure 2.9 described in Section 2.2.4). On the other hand, the analysis described in this thesis is specifically designed to cover the parameter space where the stop can decay into only $b\tilde{\chi}_1^\pm$, and the difference of the mass between chargino and neutralino is small. The event selection based on a soft lepton, a high p_T ISR-jet, and large $E_\mathrm{T}^\mathrm{miss}$ is optimized to enhance the signal sensitivity of the higgsino LSP scenario. As a result, this analysis excludes 415 GeV of the stop mass at the $\mathrm{m}_{\tilde{\chi}_1^0} = 300$ GeV as shown in Figure 8.1(a). By combining this result with the previous results, the naturalness considered in the higgsino LSP scenario is restricted widely.

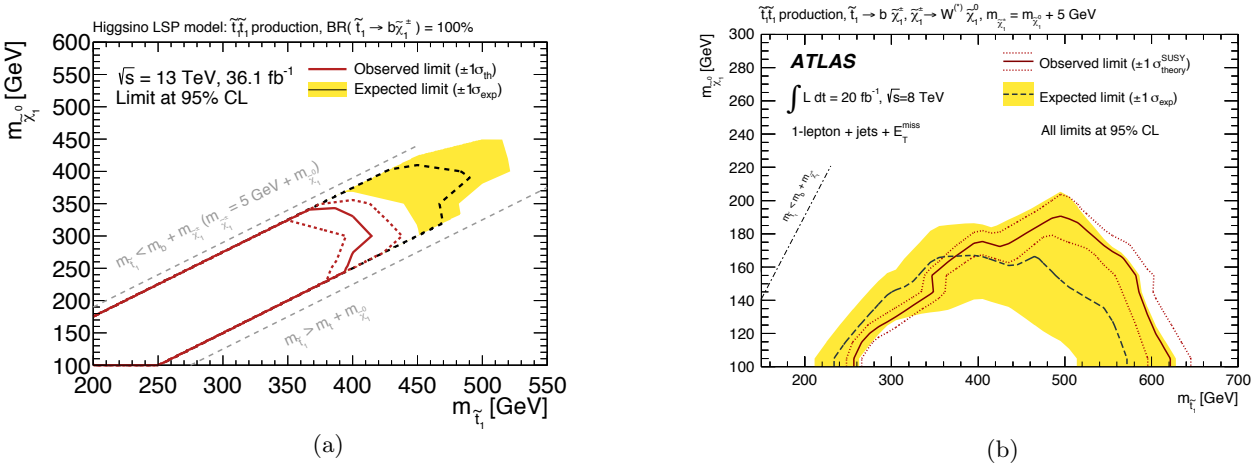

(a) (b)

Figure 8.1: (a) Exclusion contour as a function of stop and neutralino mass for the higgsino LSP scenario with BR($\tilde{t}_1 \to b\tilde{\chi}_1^\pm$) = 100% and (b) the exclusion limits of the direct stop pair production decayed to $t\tilde{\chi}_1^0$ or $b\tilde{\chi}_1^\pm$ with $\Delta m(\tilde{\chi}_1^\pm, \tilde{\chi}_1^0) = 5$ GeV at $\sqrt{s} = 8$ TeV pp collisions in the ATLAS experiment [27].

8.2 Combination of the Wino NLSP Scenario

In the wino NLSP scenario, stop decays into several processes corresponding to the mass. The analysis, assuming the mass difference of the chargino and the neutralino to be $m_{\tilde{\chi}_1^\pm} = 2 \times m_{\tilde{\chi}_1^0}$, excluded the stop mass up to 900 GeV at 95% CL as shown in Figure 8.2(a). On the other hand, the analysis described in this thesis specifically covers the parameter spacce where the mass difference of the stop and the chargino is 10 GeV. The signal region dedicated to this analysis is newly defined and the stop mass up to 850 GeV was excluded at 95% CL as shown in Figure 8.2(b). The blue dashed line of Figure 8.2(b) represents the parameter region where the chargino mass is $m_{\tilde{\chi}_1^\pm} = 2 \times m_{\tilde{\chi}_1^0}$. This means that the result described in this thesis cover unique phase space. The neutralino, which is the candidate of the dark matter was restricted widely by combining these results.

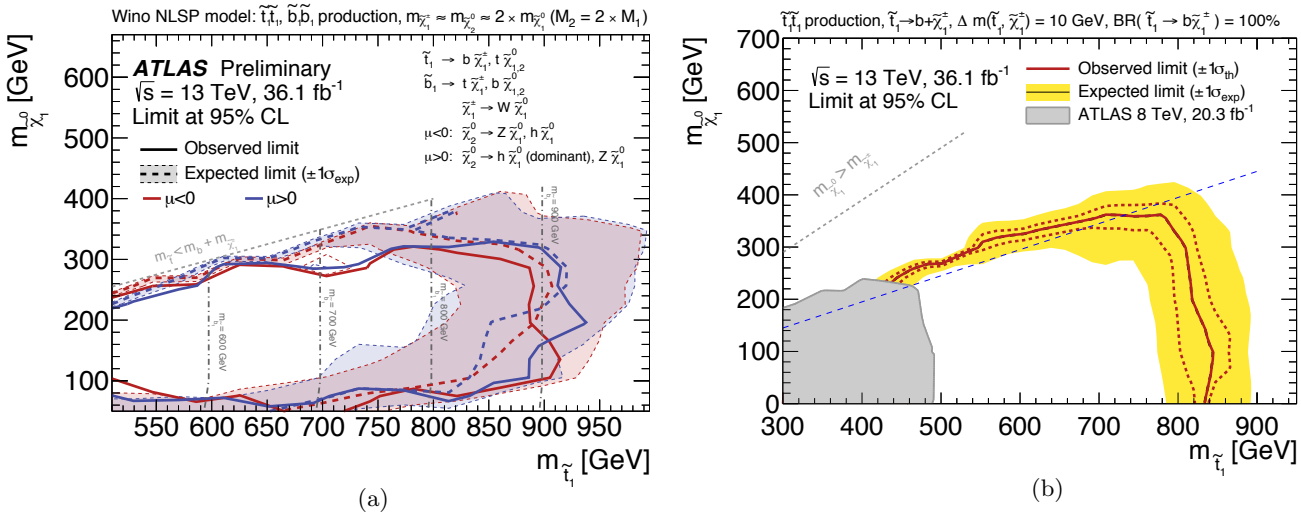

(a) (b)

Figure 8.2: (a) Exclusion limit of the direct stop pair production decayed to $b\tilde{\chi}_1^\pm$ with $m_{\tilde{\chi}_1^\pm} = 2m_{\tilde{\chi}_1^0}$ GeV [27] and (b) exclusion contour of as a function of stop and neutralino mass for the wino NLSP scenario with $\Delta m(\tilde{t}_1, \tilde{\chi}_1^\pm) = 10$ GeV.

Chapter 9

Conclusion

This thesis presents two searches for stop pair production of compressed SUSY scenarios in the final state involving one lepton, jets and $E_{\mathrm{T}}^{\mathrm{miss}}$ in pp collisions at $\sqrt{s} = 13$ TeV with the ATLAS detector. The full dataset 36.1 fb^{-1} collected in 2015 and 2016.

The first search focuses on the higgsino LSP scenario with small mass difference between the chargino and the neutralino. The SR based on a soft lepton, large $E_{\mathrm{T}}^{\mathrm{miss}}$ and high p_{T} ISR-jet is optimized to enhance the signal sensitivity of this scenario. The dominant backgrounds ($t\bar{t}$ and W + jets) remaining after the event selection is estimated by using a semi-data driven method to reduce the systematic uncertainties. The QCD/multi-jets background including a fake leptons is measured to be negligible. No significant excess above SM expectation is observed in the SR. The result is reinterpreted to determinate the exclusion limit. The parameter space in the higgsino LSP scenario is widely excluded. In particular, the stop mass $\mathrm{m}_{\tilde{t}_1} = 415$ GeV at the $\mathrm{m}_{\tilde{\chi}_1^0} = 300$ GeV is excluded at 95% CL.

The second search focuses on the wino NLSP scenario with small mass difference between the stop and the chargino. The event selection based on the b-jets veto, a high-p_{T} lepton, high-p_{T} jets, high $E_{\mathrm{T}}^{\mathrm{miss}}$ is opptimized to enhance the signal sensitivity of the wino NLSP scenario. The dominant background (W + jets) is estimated by using a semi-data driven method. No significant excess above the SM expectation is observed in the SR. The parameter space of the wino NLSP scenario is widely excluded. In particular, the stop mass up to 850 GeV is excluded at 95% CL.

Two results described in this thesis provide the stringent constraints on the stop pair production where the mass of the stop, chargino and neutralino are compressed. The results impact on the SUSY model to solve the problem of the naturalness and the DM.

Appendix A

Statistical analysis

If the new physics such as the SUSY is real, the decay event rate is very rare and the total number of events is very few. On the other hand, SM events occur very high rate, and so the total number of events in data are almost the SM events. Therefore, this analysis introduces the hypothesis testing that is the one of the statistical analysis methods.

A.1 Hypothesis Testing

This method tests a hypothesis which is true whether false by calculating the observed probability of this hypothesis from the population on assuming that the hypothesis is true. Hypothesis testing defines two hypotheses: **Null hypothesis (H_0)**, **Alternative hypothesis (H_1)**.

Null hypothesis (H_0)
H_0 is defined as 'the plain boring stuff that, by default, we expect to be true'. In other word, H_0 is the real events and the events are often occurred. In case of searches for new physics, null hypothesis is defined as the only SM event. It is often referred to as the background-only (B) hypothesis.

Alternative hypothesis (H_1)
H_1 is defined as the paradox events for null hypothesis that the paradox can not be explained by null hypothesis. In case of searches for new physics, H_1 can be defined as the new physics event including the SM event. Thus, it is often referred to as the signal-plus-background (S+B) hypothesis.

In this analysis, the nominal SM event is considered the background-only hypothesis, while the signal-plus-background hypothesis includes the higgsino LSP events or the wino NLSP events as signal. The important point of hypothesis testing is to clearly separate the distribution of the number of events for null and alternative hypothesis.

A.2 Test Statistics

When we would like to claim a discovery or exclusion of a new physics, test statistics, which can quantify the hypotheses for observed data, are used. In this analysis, several test statistics are used and are described in below items:

- **p-value:**
  A p-value (p_μ) presents a quantity of a probability of a hypothesis and it is one of simple and useful test

statistics. The p-value can be computed from the observed data and it is defined as

$$p_\mu = \int_{t_{\rm obs}}^{+\infty} f(t_\mu|\mu)dt \tag{A.1}$$

where the $f(t_\mu|\mu)$ is a probability density function of the test statistic such as profile log likelihood ratio described in a below item, and μ is the strength of signal. The quantity of t_μ is typically presented as the number of events. The μ for background-only hypothesis is defined as 0 and it for signal-plus-background hypothesis is defined as 1. The p_0 quantifies the agreement of the data with the background-only hypothesis and p_1 quantifies the agreement of the data with the signal-plus-background hypothesis. In this analysis, when a probability p_μ of a hypothesis become less than 5%, this hypothesis is excluded. On the other hand, when a probability p_μ of a hypothesis become more than 5%, this hypothesis is not excluded. The level of this boundary is called the 95% CL. In case of the discovery of the new physics, the background-only hypothesis have to be excluded. If the p_0 is less 1.3×10^{-3}, an evidence of the new physics can be announced. If the discovery of new physics is claimed, p_0 have to be less than 2.9×10^{-7}.

- **Gaussian significance (Significance Z):**

This p-value can be convert other representation called "Significance Z". Significance Z is defined as the standard deviation of the probability density function with Gaussian distribution from the center value to the observed value. It is defined as

$$Z = \Phi^{-1}(1-p) \tag{A.2}$$

where the Φ^{-1} is the cumulative distribution function of the unit Gaussian. The relation between significance Z and p-value is nonlinear and monotonic relation. Therefore, significance Z always to refer to the median. If $Z = 3(5)$, it is equivalent to a $p = 1.3 \times 10^{-3}(p_0 = 2.9 \times 10^{-7})$. Figures A.1 show the illustrations of the relation between the p-value and the test statistic (a) and the relation between the significance Z and p-value (b).

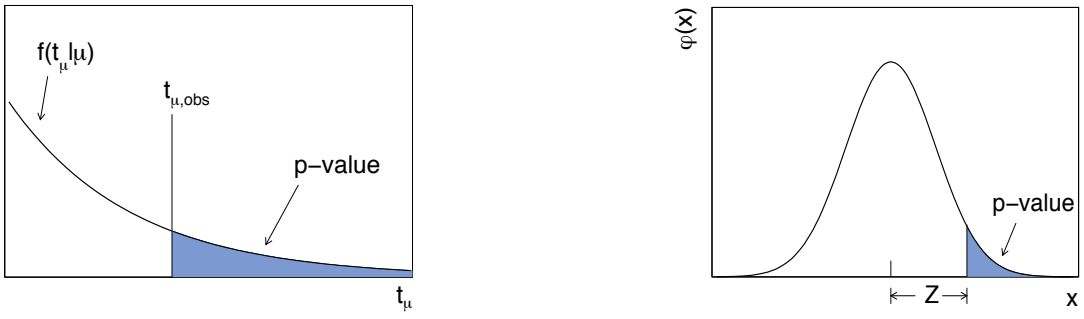

(a) (b)

Figure A.1: Illustrations of (a) the relation between the p-value and the test statistic and (b) the relation between the significance Z and p-value with the standard normal distribution.

- **Profile likelihood ratio:**

One of the simple and useful quantities for using the test statistic is the likelihood ratio by "Neyman-Pearson lemma". The likelihood function ($L(\mu, \boldsymbol{\theta})$) presents the probability density to be "X" of a function

$f(x,\theta)$ in the model parameters $\boldsymbol{\theta}$. In this analysis, all numbers of expected events of background models and signal models are generated with the likelihood fit function in SRs and CRs. These predictions of the model are affected by systematic and statistical uncertainties and a likelihood function should be taken into account these uncertainties. The model parameter called nuisance parameters, which include the rate of signal process and the normalization factors for background processes in each SR and CR, parametrize the impact of systematic uncertainties. The likelihood function is defined as

$$E_i = \mu s_i + b_i, \tag{A.3}$$

$$L(\mu,\boldsymbol{\theta}) = \prod_{j=1}^{N} \frac{E_j}{n_j!} e^{-(E_j)} \prod_{k=1}^{M} \rho(\theta_k), \tag{A.4}$$

where E_i is the expectation value of the number of signal or background in the ith bin of a histogram and $\rho(\theta_k)$ is the probability density function of each nuisance parameter. The likelihood function is the product of Poisson probabilities for all bins of SR and CRs.

The value of a likelihood function is estimated by the fitting with some free parameters such as μ or $\boldsymbol{\theta}$. A change in the expected number of events such as s_i and b_i is produced by the variation in the nuisance parameters. Since the maximization of the likelihood function called maximum-likelihood function can improve the agreement of the expectation with the observed data, the nuisance parameters is adjusted by the fitting. Each nuisance parameter corresponding to each systematic uncertainty is characterized by the probability density function ρ that are determined by auxiliary measurement corresponding to this uncertainty. Three different probability density functions are used in this analysis. One is a Gaussian probability density function, and it is used for most systematic uncertainties that change the shape of the final discriminant, e.g. the value of jet energy scale θ_{JES}, and its uncertainty σ_{JES}. Second is a log-normal probability density function that is used for normalization uncertainties. The third is a gamma probability density function. It is used to described statistical uncertainties associated with the number of selected MC events.

When nuisance parameters are estimated by the fitting, nuisance parameters are redefined as $\theta' = (\theta - \hat{\theta})/\sigma$ to be centered at zero with a width of one. Here θ is free parameter, $\hat{\theta}$ is the measured value and σ is the uncertainty. If θ' away from zero, observed data and modified MC are good agreement. On the other hand, If θ' close to zero and its error close to one, it indicates that the observed data and modified MC are disagreement.

The full profile likelihood ratio ($\lambda(\mu,\boldsymbol{\theta})$) and profile log likelihood ratio (t_μ) are defined as

$$\lambda(\mu) = \frac{L(\mu,\hat{\hat{\theta}})}{L(\hat{\mu},\hat{\theta})}, \tag{A.5}$$

$$t_\mu = -2\ln\lambda(\mu). \tag{A.6}$$

Here the numerator and denominator in the first equation are the maximized likelihood functions. $L(\mu,\hat{\hat{\theta}})$ is maximized by the free parameter $\hat{\hat{\boldsymbol{\theta}}}$ for the specified μ that is fixed value, and $\hat{\hat{\boldsymbol{\theta}}}$ is the conditional maximum-likelihood estimator of θ. The denominator is maximized by free parameters $\hat{\mu}$ and $\hat{\theta}$ and they are unconditional maximum-likelihood estimator of their. The $\hat{mu}$, $\hat{\theta}$, and $\hat{\hat{\theta}}$ are determined by the fitting for specified μ value.

In this analysis, the profile log likelihood ratio is used for the test statistics. In the condition $0 \leq \lambda(\mu) \leq 1$, if the quantity of $\lambda(\mu)$ closes to one, the observed data tend to close to good agreement with a hypothesis.

In the experiment, even if there is no any signal events of new physics, the signal strength μ does not be taken the negative value because the observed data should be same as the SM background in this case. The profile log likelihood ratio for $0 \leq \lambda(\mu) \leq 1$ and $\mu > 0$ can defined as

$$\lambda_\mu = \begin{cases} \frac{L(\mu,\hat{\hat{\theta}})}{L(\hat{\mu},\hat{\theta})} & \text{if } \hat{\mu} \leq 0, \\ \frac{L(\mu,\hat{\theta})}{L(\hat{\mu},\hat{\theta})} & \text{if } \hat{\mu} \neq 0. \end{cases}$$

On the other hand, in the case of test statistic, if the value (equivalent as the number of events) of t_μ is obtained large value in the hypothesis, the observed data and its hypothesis tend to close to incompatibility. The test statistics for $0 \leq \lambda(\mu) \leq 1$ and $\mu > 0$ can be defined as

$$t_\mu = \begin{cases} -2\ln(\mu) & \text{if } \hat{\mu} < \mu, \\ 0 & \text{if } \hat{\mu} > \mu. \end{cases}$$

The test statistic t_μ can be approximated by using the psudo-experiments and it is described in below subsection.

- **Confidence Level method:**

If some signal models are not included in the observed data, the exclusion limit that present the upper limit of the signal models can be decided for observed data. The data is sometimes observed lower than the SM backgrounds from MC predictions for the statistical fluctuation. In that case, even if a new physics exists in reality, this analysis excludes it in surplus. The CL method can protect to exclude the signal in surplus and it is used for setting the exclusion limit in this analysis. The p-value definitions of the signal-plus-background hypothesis ($\mu = 1$) and the background-only hypothesis ($\mu = 0$) are written as

$$p_1 = \int_{t_{\rm obs}}^{+\infty} f(t_1|1)dt \text{ (for } H_1), \tag{A.7}$$

$$p_0 = \int_{t_{\rm obs}}^{+\infty} f(t_0|0)dt \text{ (for } H_0). \tag{A.8}$$

$$\tag{A.9}$$

Therefore, CL_{s+b}, CL_b, and CL_s for the signal-plus-background, background-only, and signal hypothesis are simply defined as

$$CL_{s+b} = p_1 \tag{A.10}$$

$$CL_b = 1 - p_0 \tag{A.11}$$

$$CL_s = \frac{CL_{\rm s+b}}{CL_{\rm b}} = \frac{p_1}{1-p_0} \tag{A.12}$$

$$\tag{A.13}$$

When the observed CL_s is less than 0.05 for one signal model, it can claim that the one signal model is excluded with 95% CL. This analysis always excludes all hypotheses at the 95% CL.

A.3 Approximate Sampling Distributions for Test Statistics

To compute the p-value of the signal-plus-background hypothesis or background-only hypothesis, the distribution of the test statistic should be calculated. The observed value of the test statistic can be obtained from the observed data, but the distribution is only calculable from the psudo-experiments of toy MCs. The normal

psudo-experiments to compute the distribution need typically about 10^8 samples and this calculation is computationally expensive. Therefore, the distribution of test statistic is approximated by using the asymptotic formulae [125] with the asimov data set. For example, the approximation of the test statistic is defined as

$$t_\mu = -2\ln\lambda(\mu) = \frac{(\mu^2-\hat{\mu})^2}{\sigma^2} + \emptyset(\frac{1}{\sqrt{N}}) \quad (\hat{\mu} < \mu), \tag{A.14}$$

where $\hat{\mu}$ follows a Gaussian distribution of probability density function for t_μ with mean μ', and a general this distribution is defined as

$$f(t_\mu|\mu') = \frac{1}{2\sqrt{t_\mu}}\frac{1}{\sqrt{2\pi}} + [\exp(-\frac{1}{2}(\sqrt{t_\mu} + \frac{\mu-\mu'}{\sigma})^2) + \exp(-\frac{1}{2}(\sqrt{t_\mu} - \frac{\mu-\mu'}{\sigma})^2)]. \tag{A.15}$$

The σ is the standard deviation of the probability density function. The N is the number of the events in the SR. In general, the $\frac{1}{\sqrt{N}}$ term is ignored from the approximation. In this fact, this approximation method work only when the number of observed events is more than 5. Figure A.2 show the examples for the distributions of the test statistics and the distributions of these probability density functions. These distributions correspond to the signal-plus-background hypothesis and the background-only hypothesis. All distributions can be computed by the fitting with the function μ, and then finally p-values for these hypotheses can be obtained.

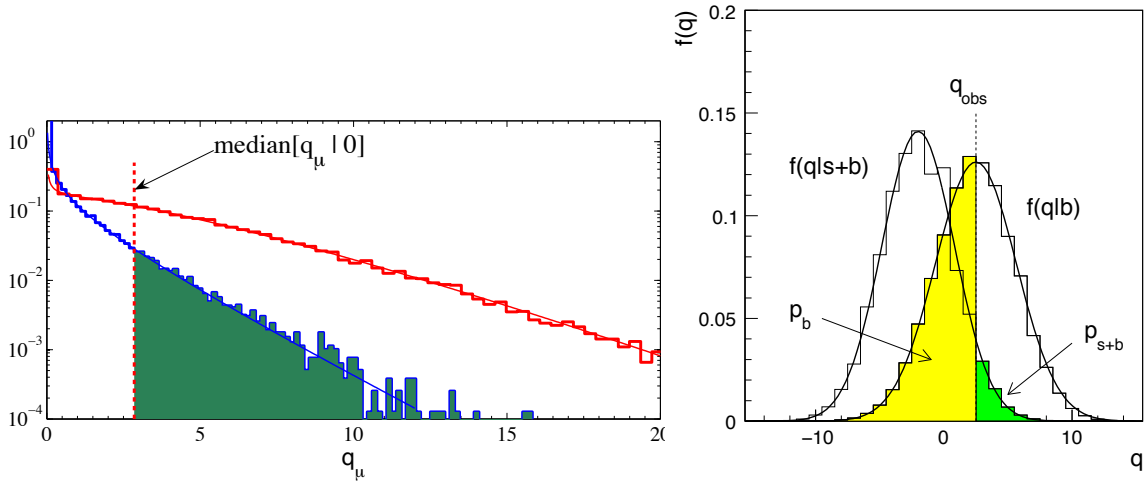

(a) (b)

Figure A.2: (a) The distributions of the test statistics q_μ and (b) the distributions of the probability density function of these. These distributions correspond to the signal-plus-background hypothesis and the background-only hypothesis.

Appendix B

Glossaries

Glossaries

pp	proton-proton. 1, 2, 13–15, 18, 19, 30–34, 51, 55, 101, 103, 109
SM	Standard Model. 1–4, 6–8, 33, 55, 58, 69, 70, 72, 75, 82, 97, 103, 104, 107, 109
ATLAS	A Toroidal LHC ApparatuS. 1, 2, 15, 16, 18–20, 22, 24, 27, 28, 37, 38, 41, 44, 50, 86, 109
BR	branching ratio. 13, 16, 17, 55, 101, 109
CERN	European Organization for Nuclear Research. 18, 109
CL	confidence level. 84, 85, 100–103, 105, 107, 109
CMB	cosmic microwave background. 4, 5, 109
CMS	Compact Muon Solenoid. 1, 109
CR	control region. 60, 61, 63, 69, 70, 75–79, 82, 84, 90–95, 97, 106, 109
CSC	Cathode Strip Chamber. 24, 26, 109
CTP	central trigger processor. 28, 109
DAQ	data acquisition. 28, 29, 109
DM	dark matter. 1, 4, 5, 8, 11, 13, 17, 103, 109
DQ	data quality. 29, 109
EM	electromagnetic. 38, 45, 46, 109
FSR	final state radiation. 31, 34, 109
GRL	Good Run List. 29, 109
HLT	high level trigger. 28, 109
IBL	Insertable B-Layer. 20, 21, 109
ID	inner detector. 20, 36, 41, 42, 47, 73, 109

ISR initial state radiation. 31, 34, 54, 55, 101, 103, 109

JER Jet Energy Resolution. 72, 73, 89, 109
JES Jet Energy Scale. 72, 73, 109

L1 level one. 28, 29, 51, 62, 109
LAr liquid argon. 23, 109
LHC Large Hadron Collider. 1, 2, 18–20, 22, 28, 30–32, 37, 72, 109
LSP Lightest Supersymmetric Particle. 1, 2, 6, 8, 10–13, 15–17, 35, 41, 54–57, 75, 84, 85, 101, 103, 104, 109

MC Monte Carlo. 2, 16, 30, 32, 33, 35, 39, 40, 42, 45, 46, 52, 58, 60–63, 72–79, 85, 92–95, 109
MDT Monitored Drift Tube. 24, 26, 109
ME matrix element. 30, 32, 34, 109
MS Muon Spectrometer. 24, 36, 41–43, 73, 109
MSSM Minimal Supersymmetric SM. 1, 6, 7, 9, 109

NLSP Next-to-Lightest Supersymmetric Particle. 12, 13, 15–17, 35, 41, 86, 88, 91, 100, 102–104, 109

PDF parton distribution functions. 30, 31, 34, 35, 109
PS parton shower. 32, 34, 109

QCD quantum chromodynamics. 26, 30–32, 60–62, 69, 70, 72, 103, 109
QED quantum electrodynamics. 30, 109

RoI Regions of Interest. 28, 51, 109
RPC Resistive Plate Chamber. 24, 25, 109

SCT SemiConductor Tracker. 20, 21, 109
sparticle SUSY particle. 6, 7, 9, 16, 17, 109
SR signal region. 55, 57, 58, 60, 61, 63, 66, 69, 70, 72, 75, 82, 84, 85, 90–92, 97, 99, 100, 103, 106, 109
SSB Spontaneous Symmetry Breaking. 3, 6, 7, 109
stop scalar top quark. 1, 7, 9–18, 59, 84–86, 100–103, 109
SUSY Supersymmetry. 1, 2, 6–8, 28, 75, 103, 109

TGC Thin Gap Chamber. 24–26, 109
TRT Transition Radiation Tracker. 20, 22, 109

UE underlying event. 31, 32, 34, 109

VEV vacuum expectation value. 6, 109
VR validation region. 61, 75, 90–92, 109

WIMP Weakly-Interacting Massive Particle. 5, 109

References

[1] *Quarks and Leptons*. John Wiley & Sons. Inc., United States of America, 1984.

[2] *Figure of Standard Model*, `https://en.wikipedia.org/wiki/Standard_Model#/media/File:Standard_Model_of_Elementary_Particles.svg`.

[3] C. Patrignani and P. D. Group, *Review of Particle Physics*, Chinese Physics C **40** (2016) 100001, `http://stacks.iop.org/1674-1137/40/i=10/a=100001`.

[4] K. G. Wilson, *Renormalization Group and Strong Interactions*, Phys. Rev. D **3** (1971) 1818–1846, `https://link.aps.org/doi/10.1103/PhysRevD.3.1818`.

[5] G. 't Hooft, C. Itzykson, A. Jaffe, H. Lehmann, P. K. Mitter, I. M. Singer, and R. Stora, *Recent Developments in Gauge Theories. Proceedings, Nato Advanced Study Institute, Cargese, France, August 26 - September 8, 1979*, NATO Sci. Ser. B **59** (1980) pp.1–438.

[6] A. M. Cooper-Sarkar, *Naturaless after LHC8*, PoS **EPS2013** (2013) 163.

[7] L. Susskind, *Dynamics of spontaneous symmetry breaking in the Weinberg-Salam theory*, Phys. Rev. D **20** (1979) 2619–2625, `https://link.aps.org/doi/10.1103/PhysRevD.20.2619`.

[8] G. Steigman, B. Dasgupta, and J. F. Beacom, *Precise Relic WIMP Abundance and its Impact on Searches for Dark Matter Annihilation*, Phys. Rev. **D86** (2012) 023506, `arXiv:1204.3622 [hep-ph]`.

[9] H. Kurki-Suonio, *Physics of the Cosmic Microwave Background and the Planck Mission*, ArXiv e-prints (2010), `arXiv:1012.5204 [astro-ph.CO]`.

[10] C. L. Bennett, D. Larson, J. L. Weiland, N. Jarosik, G. Hinshaw, N. Odegard, K. M. Smith, R. S. Hill, B. Gold, M. Halpern, E. Komatsu, M. R. Nolta, L. Page, D. N. Spergel, E. Wollack, J. Dunkley, A. Kogut, M. Limon, S. S. Meyer, G. S. Tucker, and E. L. Wright, *Nine-year Wilkinson Microwave Anisotropy Probe (WMAP) Observations: Final Maps and Results*, The Astrophysical Journal Supplement Series **208** (2013) 20, `http://stacks.iop.org/0067-0049/208/i=2/a=20`.

[11] Planck Collaboration, P. A. R. Ade et al., *Planck 2015 results. XIII. Cosmological parameters*, Astron. Astrophys. **594** (2016) A13, `arXiv:1502.01589 [astro-ph.CO]`.

[12] H. Miyazawa, *Baryon Number Changing Currents*, Prog. Theor. Phys. **36 (6)** (1966) 1266.

[13] R. Ramond, *Dual Theory for Free Fermions*, Phys. Rev. D **3** (1971) 2415.

[14] Yu. A. Golfand and E. P. Likhtman, *Extension of the Algebra of Poincare Group Generators and Violation of p Invariance*, JETP Lett. **13** (1971) 323, [Pisma Zh. Eksp. Teor. Fiz. 13 (1971) 452].

[15] A. Neveu and J. Schwarz, *Factorizable dual model of pions*, Nucl. Phys. B **31** (1971) 86.

[16] A. Neveu and J. Schwarz, *Quark Model of Dual Pions*, Phys. Rev. D **4** (1971) 1109.

[17] J. Gervais and B. Sakita, *Field theory interpretation of supergauges in dual models*, Nucl. Phys. B **34** (1971) 632.

[18] D. V. Volkov and V. P. Akulov, *Is the Neutrino a Goldstone Particle?*, Phys. Lett. B **46** (1973) 109.

[19] J. Wess and B. Zumino, *A Lagrangian Model Invariant Under Supergauge Transformations*, Phys. Lett. B **49** (1974) 52.

[20] J. Wess and B. Zumino, *Supergauge Transformations in Four-Dimensions*, Nucl. Phys. B **70** (1974) 39.

[21] S. P. Martin, *A Supersymmetry primer*, `arXiv:hep-ph/9709356 [hep-ph]`, [Adv. Ser. Direct. High Energy Phys.18,1(1998)].

[22] L. J. Hall, D. Pinner, and J. T. Ruderman, *A Natural SUSY Higgs Near 126 GeV*, JHEP **04** (2012) 131, `arXiv:1112.2703 [hep-ph]`.

[23] M. Papucci, J. T. Ruderman, and A. Weiler, *Natural SUSY Endures*, JHEP **09** (2012) 035, `arXiv:1110.6926 [hep-ph]`.

[24] N. Arkani-Hamed, A. Delgado, and G. F. Giudice, *The Well-tempered neutralino*, Nucl. Phys. **B741** (2006) 108–130, `arXiv:hep-ph/0601041 [hep-ph]`.

[25] J. Bramante, N. Desai, P. Fox, A. Martin, B. Ostdiek, and T. Plehn, *Towards the Final Word on Neutralino Dark Matter*, Phys. Rev. **D93** (2016) 063525, `arXiv:1510.03460 [hep-ph]`.

[26] ATLAS Collaboration, *Search for top squark pair production in final states with one isolated lepton, jets, and missing transverse momentum using* 36 fb^{-1} *of* $\sqrt{s} = 13$ *TeV pp collision data with the ATLAS detector*, ATLAS-CONF-2017-037, 2017, `https://cds.cern.ch/record/2266170`.

[27] ATLAS Collaboration, G. Aad et al., *Search for top squark pair production in final states with one isolated lepton, jets, and missing transverse momentum in* $\sqrt{s}$ *=8 TeV pp collisions with the ATLAS detector*, JHEP **11** (2014) 118, `arXiv:1407.0583 [hep-ex]`.

[28] CMS Collaboration, A. M. Sirunyan et al., *Search for top squark pair production in pp collisions at sqrt(s)=13 TeV using single lepton events*, `arXiv:1706.04402 [hep-ex]`.

[29] *TE-EPC-LPC in LHC*, `http://te-epc-lpc.web.cern.ch/te-epc-lpc/machines/lhc/general.stm`.

[30] *Luminosity Public Results in Run2*, `https://twiki.cern.ch/twiki/bin/view/AtlasPublic/LuminosityPublicResultsRun2#Pileup_Interactions_and_Data_AN1`.

[31] T. A. Collaboration, *The ATLAS Experiment at the CERN Large Hadron Collider*, Journal of Instrumentation **3** (2008) S08003, `http://stacks.iop.org/1748-0221/3/i=08/a=S08003`.

[32] U. Egede, *The search for a Standard Model Higgs at the LHC and electron identification using transition radiation in the ATLAS tracker*. PhD thesis, Lund U., 1998. `http://preprints.cern.ch/cgi-bin/setlink?base=preprint&categ=cern&id=THESIS-98-001`.

[33] ATLAS Collaboration,, *Design of the ATLAS detector*, `http://www.hep.lu.se/atlas/thesis/egede/thesis-node39.html`.

[34] ATLAS Collaboration,, *ATLAS detector and physics performance: Technical Design Report, 1*. Technical Design Report ATLAS. CERN, Geneva, 1999. `https://cds.cern.ch/record/391176`.

[35] ATLAS Collaboration,, *ATLAS detector and physics performance: Technical Design Report, 2*. Technical Design Report ATLAS. CERN, Geneva, 1999. https://cds.cern.ch/record/391177.

[36] M. Backhaus, *The upgraded Pixel Detector of the {ATLAS} Experiment for Run 2 at the Large Hadron Collider*, Nuclear Instruments and Methods in Physics Research Section A: Accelerators, Spectrometers, Detectors and Associated Equipment **831** (2016) 65 – 70, http://www.sciencedirect.com/science/article/pii/S0168900216303837, Proceedings of the 10th International "Hiroshima" Symposium on the Development and Application of Semiconductor Tracking Detectors.

[37] ATLAS Collaboration, M. Capeans, G. Darbo, K. Einsweiller, M. Elsing, T. Flick, M. Garcia-Sciveres, C. Gemme, H. Pernegger, O. Rohne, and R. Vuillermet, *ATLAS Insertable B-Layer Technical Design Report*, Tech. Rep. CERN-LHCC-2010-013. ATLAS-TDR-19, Sep, 2010. https://cds.cern.ch/record/1291633.

[38] ATLAS Muon Collaboration, E. Diehl, *ATLAS Muon Detector Commissioning*, in *Particles and fields. Proceedings, Meeting of the Division of the American Physical Society, DPF 2009, Detroit, USA, July 26-31, 2009*. 2009. arXiv:0910.2767 [physics.ins-det]. https://inspirehep.net/record/834063/files/arXiv:0910.2767.pdf.

[39] ATLAS Collaboration,, *ATLAS muon spectrometer: Technical Design Report*. Technical Design Report ATLAS. CERN, Geneva, 1997. https://cds.cern.ch/record/331068.

[40] ATLAS Collaboration,, *ATLAS muon spectrometer: Update of Technical Design Report*. Technical Design Report ATLAS. CERN, Geneva, 2000.

[41] ATLAS Collaboration, G. Aad et al., *Commissioning of the ATLAS Muon Spectrometer with Cosmic Rays*, Eur. Phys. J. **C70** (2010) 875–916, arXiv:1006.4384 [physics.ins-det].

[42] A. Polini, *Design and performance of the detector control system of the ATLAS resistive-plate-chamber muon spectrometer*, Nuclear Instruments and Methods in Physics Research Section A: Accelerators, Spectrometers, Detectors and Associated Equipment **661** (2012) S15 – S18, http://www.sciencedirect.com/science/article/pii/S0168900210017304, X. Workshop on Resistive Plate Chambers and Related Detectors (RPC 2010).

[43] A. Ruiz-Martinez and A. Collaboration, *The Run-2 ATLAS Trigger System*, Tech. Rep. ATL-DAQ-PROC-2016-003, CERN, Geneva, Feb, 2016. http://cds.cern.ch/record/2133909.

[44] ATLAS Collaboration,, *L1 Trigger Rate*, https://twiki.cern.ch/twiki/bin/view/AtlasPublic/TriggerOperationPublicResults#2016_pp_at_13_TeV.

[45] A. Buckley et al., *General-purpose event generators for LHC physics*, Phys. Rept. **504** (2011) 145–233, arXiv:1101.2599 [hep-ph].

[46] P. Z. Skands, *QCD for Collider Physics*, in *Proceedings, High-energy Physics. Proceedings, 18th European School (ESHEP 2010): Raseborg, Finland, June 20 - July 3, 2010*. 2011. arXiv:1104.2863 [hep-ph]. https://inspirehep.net/record/896215/files/arXiv:1104.2863.pdf.

[47] J. C. Collins, D. E. Soper, and G. F. Sterman, *Factorization of Hard Processes in QCD*, Adv. Ser. Direct. High Energy Phys. **5** (1989) 1–91, arXiv:hep-ph/0409313 [hep-ph].

[48] Y. L. Dokshitzer, *Calculation of the Structure Functions for Deep Inelastic Scattering and e+ e- Annihilation by Perturbation Theory in Quantum Chromodynamics.*, Sov. Phys. JETP **46** (1977) 641–653, [Zh. Eksp. Teor. Fiz.73,1216(1977)].

[49] V. N. Gribov and L. N. Lipatov, *Deep inelastic e p scattering in perturbation theory*, Sov. J. Nucl. Phys. **15** (1972) 438–450, [Yad. Fiz.15,781(1972)].

[50] G. Altarelli and G. Parisi, *Asymptotic Freedom in Parton Language*, Nucl. Phys. **B126** (1977) 298–318.

[51] J. Butterworth et al., *PDF4LHC recommendations for LHC Run II*, J. Phys. **G43** (2016) 023001, arXiv:1510.03865 [hep-ph].

[52] NNPDF Collaboration, R. D. Ball et al., *Parton distributions for the LHC Run II*, JHEP **04** (2015) 040, arXiv:1410.8849 [hep-ph].

[53] S. Dulat, T.-J. Hou, J. Gao, M. Guzzi, J. Huston, P. Nadolsky, J. Pumplin, C. Schmidt, D. Stump, and C. P. Yuan, *New parton distribution functions from a global analysis of quantum chromodynamics*, Phys. Rev. **D93** (2016) 033006, arXiv:1506.07443 [hep-ph].

[54] A. D. Martin, W. J. Stirling, R. S. Thorne, and G. Watt, *Heavy-quark mass dependence in global PDF analyses and 3- and 4-flavour parton distributions*, Eur. Phys. J. **C70** (2010) 51–72, arXiv:1007.2624 [hep-ph].

[55] B. Andersson, G. Gustafson, G. Ingelman, and T. Sjostrand, *Parton Fragmentation and String Dynamics*, Phys. Rept. **97** (1983) 31–145.

[56] S. Catani, F. Krauss, R. Kuhn, and B. R. Webber, *QCD matrix elements + parton showers*, JHEP **11** (2001) 063, arXiv:hep-ph/0109231 [hep-ph].

[57] F. Krauss, *Matrix elements and parton showers in hadronic interactions*, JHEP **08** (2002) 015, arXiv:hep-ph/0205283 [hep-ph].

[58] J. Alwall et al., *Comparative study of various algorithms for the merging of parton showers and matrix elements in hadronic collisions*, Eur. Phys. J. **C53** (2008) 473–500, arXiv:0706.2569 [hep-ph].

[59] S. Alioli, P. Nason, C. Oleari, and E. Re, *A general framework for implementing NLO calculations in shower Monte Carlo programs: the POWHEG BOX*, JHEP **06** (2010) 043, arXiv:1002.2581 [hep-ph].

[60] H.-L. Lai, M. Guzzi, J. Huston, Z. Li, P. M. Nadolsky, J. Pumplin, and C. P. Yuan, *New parton distributions for collider physics*, Phys. Rev. **D82** (2010) 074024, arXiv:1007.2241 [hep-ph].

[61] T. Sjostrand, S. Mrenna, and P. Z. Skands, *PYTHIA 6.4 Physics and Manual*, JHEP **05** (2006) 026, arXiv:hep-ph/0603175 [hep-ph].

[62] P. Z. Skands, *Tuning Monte Carlo Generators: The Perugia Tunes*, Phys. Rev. **D82** (2010) 074018, arXiv:1005.3457 [hep-ph].

[63] M. Czakon, P. Fiedler, and A. Mitov, *Total Top-Quark Pair-Production Cross Section at Hadron Colliders Through $O(\alpha_S^4)$*, Phys. Rev. Lett. **110** (2013) 252004, arXiv:1303.6254 [hep-ph].

[64] M. Czakon and A. Mitov, *NNLO corrections to top pair production at hadron colliders: the quark-gluon reaction*, JHEP **01** (2013) 080, arXiv:1210.6832 [hep-ph].

[65] M. Czakon and A. Mitov, *NNLO corrections to top-pair production at hadron colliders: the all-fermionic scattering channels*, JHEP **12** (2012) 054, arXiv:1207.0236 [hep-ph].

[66] P. Brnreuther, M. Czakon, and A. Mitov, *Percent Level Precision Physics at the Tevatron: First Genuine NNLO QCD Corrections to $q\bar{q} \to t\bar{t} + X$*, Phys. Rev. Lett. **109** (2012) 132001, arXiv:1204.5201 [hep-ph].

[67] M. Cacciari, M. Czakon, M. Mangano, A. Mitov, and P. Nason, *Top-pair production at hadron colliders with next-to-next-to-leading logarithmic soft-gluon resummation*, Phys. Lett. **B710** (2012) 612–622, arXiv:1111.5869 [hep-ph].

[68] M. Czakon and A. Mitov, *Top++: A Program for the Calculation of the Top-Pair Cross-Section at Hadron Colliders*, Comput. Phys. Commun. **185** (2014) 2930, arXiv:1112.5675 [hep-ph].

[69] N. Kidonakis, *Next-to-next-to-leading-order collinear and soft gluon corrections for t-channel single top quark production*, Phys. Rev. **D83** (2011) 091503, arXiv:1103.2792 [hep-ph].

[70] N. Kidonakis, *Two-loop soft anomalous dimensions for single top quark associated production with a W- or H-*, Phys. Rev. **D82** (2010) 054018, arXiv:1005.4451 [hep-ph].

[71] N. Kidonakis, *NNLL resummation for s-channel single top quark production*, Phys. Rev. **D81** (2010) 054028, arXiv:1001.5034 [hep-ph].

[72] T. Gleisberg, S. Hoeche, F. Krauss, M. Schonherr, S. Schumann, F. Siegert, and J. Winter, *Event generation with SHERPA 1.1*, JHEP **02** (2009) 007, arXiv:0811.4622 [hep-ph].

[73] S. Catani, L. Cieri, G. Ferrera, D. de Florian, and M. Grazzini, *Vector boson production at hadron colliders: a fully exclusive QCD calculation at NNLO*, Phys. Rev. Lett. **103** (2009) 082001, arXiv:0903.2120 [hep-ph].

[74] J. Alwall, R. Frederix, S. Frixione, V. Hirschi, F. Maltoni, O. Mattelaer, H. S. Shao, T. Stelzer, P. Torrielli, and M. Zaro, *The automated computation of tree-level and next-to-leading order differential cross sections, and their matching to parton shower simulations*, JHEP **07** (2014) 079, arXiv:1405.0301 [hep-ph].

[75] T. Sjostrand, S. Mrenna, and P. Z. Skands, *A Brief Introduction to PYTHIA 8.1*, Comput. Phys. Commun. **178** (2008) 852–867, arXiv:0710.3820 [hep-ph].

[76] ATLAS Collaboration, *ATLAS Pythia 8 tunes to 7 TeV data*, ATL-PHYS-PUB-2014-021, 2014, https://cds.cern.ch/record/1966419.

[77] R. D. Ball et al., *Parton distributions with LHC data*, Nucl. Phys. **B867** (2013) 244–289, arXiv:1207.1303 [hep-ph].

[78] C. Borschensky, M. Krmer, A. Kulesza, M. Mangano, S. Padhi, T. Plehn, and X. Portell, *Squark and gluino production cross sections in pp collisions at $\sqrt{s}$ = 13, 14, 33 and 100 TeV*, Eur. Phys. J. **C74** (2014) 3174, arXiv:1407.5066 [hep-ph].

[79] E. Re, *Single-top Wt-channel production matched with parton showers using the POWHEG method*, Eur. Phys. J. **C71** (2011) 1547, arXiv:1009.2450 [hep-ph].

[80] S. Frixione, P. Nason, and G. Ridolfi, *A Positive-weight next-to-leading-order Monte Carlo for heavy flavour hadroproduction*, JHEP **09** (2007) 126, arXiv:0707.3088 [hep-ph].

[81] R. Frederix, E. Re, and P. Torrielli, *Single-top t-channel hadroproduction in the four-flavour scheme with POWHEG and aMC@NLO*, JHEP **09** (2012) 130, arXiv:1207.5391 [hep-ph].

[82] S. Alioli, P. Nason, C. Oleari, and E. Re, *NLO single-top production matched with shower in POWHEG: s- and t-channel contributions*, JHEP **09** (2009) 111, arXiv:0907.4076 [hep-ph], [Erratum: JHEP02,011(2010)].

[83] D. J. Lange, *The EvtGen particle decay simulation package*, Nucl. Instrum. Meth. **A462** (2001) 152–155.

[84] J. Pumplin, D. R. Stump, J. Huston, H. L. Lai, P. M. Nadolsky, and W. K. Tung, *New generation of parton distributions with uncertainties from global QCD analysis*, JHEP **07** (2002) 012, arXiv:hep-ph/0201195 [hep-ph].

[85] S. Carrazza, S. Forte, and J. Rojo, *Parton Distributions and Event Generators*, pp. , 89–96. 2013. arXiv:1311.5887 [hep-ph]. https://inspirehep.net/record/1266070/files/arXiv:1311.5887.pdf.

[86] A. M. Cooper-Sarkar, *HERAPDF1.5LO PDF Set with Experimental Uncertainties*, PoS **DIS2014** (2014) 032.

[87] GEANT4 Collaboration, S. Agostinelli et al., *GEANT4: A Simulation toolkit*, Nucl. Instrum. Meth. **A506** (2003) 250–303.

[88] ATLAS Collaboration, G. Aad et al., *The ATLAS Simulation Infrastructure*, Eur. Phys. J. **C70** (2010) 823–874, arXiv:1005.4568 [physics.ins-det].

[89] T. Gleisberg and S. Hoeche, *Comix, a new matrix element generator*, JHEP **12** (2008) 039, arXiv:0808.3674 [hep-ph].

[90] F. Cascioli, P. Maierhofer, and S. Pozzorini, *Scattering Amplitudes with Open Loops*, Phys. Rev. Lett. **108** (2012) 111601, arXiv:1111.5206 [hep-ph].

[91] S. Schumann and F. Krauss, *A Parton shower algorithm based on Catani-Seymour dipole factorisation*, JHEP **03** (2008) 038, arXiv:0709.1027 [hep-ph].

[92] S. Hoeche, F. Krauss, M. Schonherr, and F. Siegert, *QCD matrix elements + parton showers: The NLO case*, JHEP **04** (2013) 027, arXiv:1207.5030 [hep-ph].

[93] ATLAS Collaboration, *The Optimization of ATLAS Track Reconstruction in Dense Environments*, ATL-PHYS-PUB-2015-006, 2015, https://cds.cern.ch/record/2002609.

[94] A. Rosenfeld and J. L. Pfaltz, *Sequential Operations in Digital Picture Processing*, J. ACM **13** (1966) 471–494, http://doi.acm.org/10.1145/321356.321357.

[95] ATLAS Collaboration, G. Aad et al., *A neural network clustering algorithm for the ATLAS silicon pixel detector*, JINST **9** (2014) P09009, arXiv:1406.7690 [hep-ex].

[96] R. Fruhwirth, *Application of Kalman filtering to track and vertex fitting*, Nucl. Instrum. Meth. **A262** (1987) 444–450.

[97] ATLAS Collaboration, *Performance of the ATLAS Silicon Pattern Recognition Algorithm in Data and Simulation at $\sqrt{s} = 7$ TeV*, ATLAS-CONF-2010-072, 2010, https://cds.cern.ch/record/1281363.

[98] T. G. Cornelissen, M. Elsing, I. Gavrilenko, J. F. Laporte, W. Liebig, M. Limper, K. Nikolopoulos, A. Poppleton, and A. Salzburger, *The global chi**2 track fitter in ATLAS*, J. Phys. Conf. Ser. **119** (2008) 032013.

[99] G. Borissov, D. Casper, K. Grimm, S. P. Griso, L. E. Pedersen, K. Prokofiev, M. Rudolph, and A. Wharton, *ATLAS strategy for primary vertex reconstruction during Run-2 of the LHC*, Journal of Physics: Conference Series **664** (2015) 072041, http://stacks.iop.org/1742-6596/664/i=7/a=072041.

[100] ATLAS Collaboration, *Performance of primary vertex reconstruction in proton–proton collisions at $\sqrt{s} = 7$ TeV in the ATLAS experiment*, ATLAS-CONF-2010-069, 2010, https://cds.cern.ch/record/1281344.

[101] ATLAS Collaboration, *Electron efficiency measurements with the ATLAS detector using the 2015 LHC proton–proton collision data*, ATLAS-CONF-2016-024, 2016, https://cds.cern.ch/record/2157687.

[102] ATLAS Collaboration, *Improved electron reconstruction in ATLAS using the Gaussian Sum Filter-based model for bremsstrahlung*, ATLAS-CONF-2012-047, 2012, https://cds.cern.ch/record/1449796.

[103] ATLAS Collaboration, G. Aad et al., *Electron and photon energy calibration with the ATLAS detector using LHC Run 1 data*, Eur. Phys. J. **C74** (2014) 3071, arXiv:1407.5063 [hep-ex].

[104] ATLAS Collaboration,, *Electron reconstruction and identification efficiency measurements in 2016 Data*, https://atlas.web.cern.ch/Atlas/GROUPS/PHYSICS/PLOTS/EGAM-2017-003/index.html.

[105] ATLAS Collaboration,, *Electron and photon energy calibration with the ATLAS detector using data collected in 2015 at $\sqrt{s} = 13$* TeV, Tech. Rep. ATL-PHYS-PUB-2016-015, CERN, Geneva, Aug, 2016. http://cds.cern.ch/record/2203514.

[106] ATLAS Collaboration, G. Aad et al., *Muon reconstruction performance of the ATLAS detector in protonproton collision data at $\sqrt{s}$ =13 TeV*, Eur. Phys. J. **C76** (2016) 292, arXiv:1603.05598 [hep-ex].

[107] J. Illingworth and J. Kittler, *A survey of the hough transform*, Computer Vision, Graphics, and Image Processing **44** (1988) 87 – 116, http://www.sciencedirect.com/science/article/pii/S0734189X88800331.

[108] ATLAS Collaboration,, *ATLAS Muon Combined Performance with the full 2016 dataset*, https://atlas.web.cern.ch/Atlas/GROUPS/PHYSICS/PLOTS/MUON-2017-001/index.html.

[109] M. Cacciari, G. P. Salam, and G. Soyez, *The Anti-k(t) jet clustering algorithm*, JHEP **04** (2008) 063, arXiv:0802.1189 [hep-ph].

[110] S. D. Ellis and D. E. Soper, *Successive combination jet algorithm for hadron collisions*, Phys. Rev. **D48** (1993) 3160–3166, arXiv:hep-ph/9305266 [hep-ph].

[111] M. Wobisch and T. Wengler, *Hadronization corrections to jet cross-sections in deep inelastic scattering*, pp. , 270–279. 1998. arXiv:hep-ph/9907280 [hep-ph]. https://inspirehep.net/record/484872/files/arXiv:hep-ph_9907280.pdf.

[112] Y. L. Dokshitzer, G. D. Leder, S. Moretti, and B. R. Webber, *Better jet clustering algorithms*, JHEP **08** (1997) 001, arXiv:hep-ph/9707323 [hep-ph].

[113] ATLAS Collaboration, M. Aaboud et al., *Jet energy scale measurements and their systematic uncertainties in proton-proton collisions at $\sqrt{s} = 13$ TeV with the ATLAS detector*, Phys. Rev. **D96** (2017) 072002, arXiv:1703.09665 [hep-ex].

[114] *Expected performance of the ATLAS b-tagging algorithms in Run-2*, Tech. Rep. ATL-PHYS-PUB-2015-022, CERN, Geneva, Jul, 2015. https://cds.cern.ch/record/2037697.

[115] ATLAS Collaboration Collaboration, I. Connelly, *Performance and calibration of b-tagging with the ATLAS experiment at LHC Run-2*, Tech. Rep. ATL-PHYS-PROC-2016-193, CERN, Geneva, Nov, 2016. https://cds.cern.ch/record/2229557.

[116] ATLAS Collaboration Collaboration,, *Optimisation of the ATLAS b-tagging performance for the 2016 LHC Run*, Tech. Rep. ATL-PHYS-PUB-2016-012, CERN, Geneva, Jun, 2016. http://cds.cern.ch/record/2160731.

[117] *Tagging and suppression of pileup jets with the ATLAS detector*, Tech. Rep. ATLAS-CONF-2014-018, CERN, Geneva, May, 2014. http://cds.cern.ch/record/1700870.

[118] *Performance of missing transverse momentum reconstruction for the ATLAS detector in the first proton-proton collisions at at* $\sqrt{s}$*= 13 TeV*, Tech. Rep. ATL-PHYS-PUB-2015-027, CERN, Geneva, Jul, 2015. https://cds.cern.ch/record/2037904.

[119] ATLAS Collaboration,, *Summary plots from the ATLAS Supersymmetry physics group*, https://atlas.web.cern.ch/Atlas/GROUPS/PHYSICS/CombinedSummaryPlots/SUSY/index.html#ATLAS_SUSY_Stop_tLSP.

[120] R. D. Cousins, J. T. Linnemann, and J. Tucker, *Evaluation of three methods for calculating statistical significance when incorporating a systematic uncertainty into a test of the background-only hypothesis for a Poisson process*, Nuclear Instruments and Methods in Physics Research Section A: Accelerators, Spectrometers, Detectors and Associated Equipment **595** (2008) 480 – 501, http://www.sciencedirect.com/science/article/pii/S0168900208010255.

[121] W. H. Press, S. A. Teukolsky, W. T. Vetterling, and B. P. Flannery, *Numerical Recipes in C (2Nd Ed.): The Art of Scientific Computing*. Cambridge University Press, New York, NY, USA, 1992.

[122] ATLAS Collaboration, *Jet Calibration and Systematic Uncertainties for Jets Reconstructed in the ATLAS Detector at* $\sqrt{s} = 13$ *TeV*, ATL-PHYS-PUB-2015-015, 2015, https://cds.cern.ch/record/2037613.

[123] G. Cabras, *Luminosity measurements of the ATLAS experiment in LHC Run2 with LUCID*, Nuovo Cimento C **40** (2017) 17. 2 p, http://cds.cern.ch/record/2288622.

[124] B. Nachman and C. G. Lester, *Significance Variables*, Phys. Rev. **D88** (2013) 075013, arXiv:1303.7009 [hep-ph].

[125] G. Cowan, K. Cranmer, E. Gross, and O. Vitells, *Asymptotic formulae for likelihood-based tests of new physics*, Eur. Phys. J. **C71** (2011) 1554, arXiv:1007.1727 [physics.data-an], [Erratum: Eur. Phys. J.C73,2501(2013)].

Acknowledgements

First of all, I would like to express my deepest thanks to my supervisor Makoto Tomoto. He gave me the opportunities for several studies in high energy physics and kindly supported my research for five years. I had no experiences in high energy physics when I joined N laboratory of Nagoya University. Thanks to his great supervision and high pressure, I enjoyed the searches for SUSY particles and completed the PhD thesis.

I would also like to express my gratitude to Keisuke Yoshihara, Tomohiro Yamazaki, Till Eifert, Javier Montejo Berlingen, Sophie Pataraia, Takashi Yamanaka, Yu Nakahama and other people of stop1L group. They kindly supported my analysis with many discussions. Thanks to thier supports, I could contribute to the ATLAS publication made by stop1L group.

I would also like to thank Yasuyuki Horii, Kentaro Kawade, Junpei Maeda, Masahiro Morinaga, Shion Chen, Takuya Nobe, and other ATLAS Japan members. They helped me for both the study and the life in France. I spent a very good time.

I am grateful to the N laboratory members, especially Toru Iijima and Kenji Inami to organize a wonderful laboratory. I thank all my friends for emotional supports. Lastly, I thank my family for continuous encouragement and financial support.